國立中山大學機械與機電工程學系

博士論文

金屬薄膜於奈米壓痕之數值模擬與實驗研究

Numerical Simulation and Experimental Test of Nanoindentation Analysis on Metal Thin Film

研究生：王中鼎 撰

指導教授：錢志回 博士

中華民國 九十六 年 十 月

謝 誌

本論文承蒙指導教授 錢志回博士與 朱訓鵬博士悉心指導方得順利完成。兩位老師的諄諄教誨與啟蒙，每遇困惑瓶頸，更且再三詳為析疑釋惑，初稿完成，復字斟句酌，細心審閱修正，師恩浩瀚，謹申誠摯敬意。

承蒙口試委員 中正大學蕭庭郎教授、成功大學陳元方教授、中興大學黃敏睿教授以及本系謝曉星教授、光灼華教授、任明華教授與楊旭光教授等於論文口試中，皆以豐富之實務與學術經驗，費心審核愷切指正，使本文更臻完備，特誌由衷謝意。

修業期間，感謝本校材料系黃志青教授在材料領域的觀念指導；義守大學材料系簡賸瑞教授在奈米壓痕方面的觀念交流與討論；日月光半導體製造公司賴逸少博士與楊秉豐主任工程師在合作計劃上有形與無形的支持；金屬中心吳以德博士在研究及課業上的協助；實驗應力實驗室及分子工程實驗室學弟妹們的幫忙；另外要特別感謝我的碩士指導教授邵清安博士在研究觀念及做人處事上不斷地耐心指點與教誨；也要特別感謝分子工程實驗室學弟李玟頡在分子動力學上的傾囊相助。

最後，謹以此論文獻予最敬愛的父母與妻子，尤其是我的妻子張淑女，在我正處於軍旅生涯校級軍官的軍階與收入下，毅然而然地選擇退伍唸博班，在完全沒有經濟收入及忙於課業與研究而疏於陪伴她的情況下，她不但要一肩擔負起家庭的經濟重擔，同時還要肩負我的寶貝女兒的教養重責，由於她這樣無悔無怨的支持與鼓勵，方能使我在無後顧之憂的情況下順利完成學業，點點滴滴感銘於心，在此深表由衷的感激。

王中鼎　謹誌

中華民國九十六年十月

于 西子灣

Contents

List of Tables

List of Figures

摘要

奈米壓痕檢測技術為目前量測奈米尺度材料之機械性質的最主要方法之一。隨著近年來奈米科技的蓬勃發展，製程技術所能製造出的奈米元件尺寸愈來愈小，以往巨觀的檢測技術已不敷使用，尤其當材料的尺寸到達原子級的尺度時，其所需之檢測精確度更是巨觀檢測技術所難以達到的，因此奈米壓痕檢測技術乃成為非常重要的微觀檢測技術。本文即利用奈米壓痕之數值及實驗方法對金屬薄膜在探針的壓痕作用下，對其材料特性進行定性及定量之分析。

本文研究方法第一部份先以分子動力學之平行運算對(100)、(110)及(111)三個定向結晶面之鎳薄膜進行奈米壓痕之模擬分析，模擬結果顯示由探針作用所造成材料塑性變形之應變能量乃是利用同質性孕核(Homogeneous Nucleation)的成形來儲存，而利用{111}滑移面的錯位滑移(Dislocation Sliding)來釋放。三個定向結晶面之壓痕曲線從曲線局部最高點到局部最低點的陡峭變化、壓痕表面的堆積隆起(Pile-up)形貌之擴散程度，以及硬度(Hardness)與彈性模數(Elastic Modulus)之材料性質等，均受材料{111}滑移面之滑移角的數目所影響；第二部份則利用分子動力學結合有限元素法與平行運算之多尺度模擬對(100)定向結晶面之鎳薄膜進行奈米壓痕之模擬分析，在與相同模擬條件之全分子動力學的模擬結果比較下，由壓痕曲線及壓痕變形形貌之模擬結果驗証了本文對於分子動力學結合有限元素法所建立之多尺度模型的正確性；第三部份則是利用奈米壓痕儀(Nanoindenter)結合聚焦離子束顯微鏡(FIB)與穿透式電子顯微鏡(TEM)來對氮化鎵(GaN)薄膜因壓痕所引起的局部相變化機制進行實驗分析。對三五族的氮化鎵材料而言，在壓痕負載的過程中，壓痕曲線會有突然跳躍(pop-in)的現象產生，此現象乃為材料的錯位成核(Dislocation Nucleation)之

變形機制，但在奈米壓痕過程中所導致的相變化機制則不存在於氮化鎵薄膜中。

關鍵詞: 分子動力學，有限元素法，奈米壓痕，金屬薄膜，材料特性

Abstract

Molecular dynamics (MD) simulations are applied to elucidate the anisotropic characteristics in the material responses for crystallographic nickel substrates with (100), (110) and (111) surface orientations during nanoindentation. The strain energy of the substrate exerted by the tip is stored by the formation of the homogeneous nucleation, and is dissipated by the dislocation sliding of the {111} plane. The steep variations of the indentation curve from the local peak to the local minimums are affected by the numbers of slip angle of {111} sliding plane. The pile-up patterns of the three nickel substrates prove that the crystalline nickel materials demonstrate the pile-up phenomenon from nanoindentation on the nanoscale. The three crystallographic nickel substrates exhibit differing amounts of pile-up dislocation spreading at different crystallographic orientations. The effects of surface orientation in material properties of F.C.C. nickel material on the nanoscale are observable through the slip angle numbers of {111} sliding planes which influence hardness values, as well as the cohesive energy of different crystallographic surfaces that indicate Young's modulus. Furthermore, the multiscale simulations are performed on the (100) monocrystal nickel substrate by using nanoindentation, compensating for MD limitation of a large specimen simulation without significant increase in the size of the problem. This study examines the accuracy of the coupling method for the multiscale model by means of the indentation curve and the deformation profile.

Nanoindentation-induced mechanical deformation in GaN thin films prepared by metal-organic chemical-vapor deposition (MOCVD) was investigated using the Berkovich diamond tip in combining with the cross-sectional transmission electron

microscopy (XTEM). By using the focused ion beam (FIB) milling to accurately position the cross-section of the indented region, the XTEM results demonstrate that the major plastic deformation was taking place through the propagation of dislocations. The present observations are in support of attributing the pop-ins appeared in the load-displacement curves to the massive dislocation activities occurring underneath the indenter during loading cycle. The absence of indentation-induced new phases might have been due to the stress relaxation via substrate and is also consistent with the fact that no discontinuity was found upon unloading.

Key words: Molecular dynamics, Finite element method, Nanoindentation, Metal thin films, Material characteristics

Nomenclature

A_p The contact area

$[C]$ Element damping matrix

E_r The reduced elastic modulus

E Young's modulus

F_i The interaction force of atom i

H The Hamiltonian function

H_d The Hardness

h_c The contact depth

$[J]$ Jacobian matrix

k_B Boltzmann constant

$[K]$ Element stiffness matrix

L The Lagrangian function

m_i The mass of atom i

$[M]$ Element mass matrix

N Total atom numbers

$[N]$ The matrix of shape function

P_i The momentum of atom i

$P_{\max}$ The maximum load of the tip at the maximum depth

$\vec{Q}$ The vector of nodal displacement

$\dot{\vec{Q}}$ The vector of nodal velocity

$\ddot{\vec{Q}}$ The vector of nodal acceleration

r_i The position of atom

$\dot{r}_i$ The velocity of atom *i*

$\ddot{r}_i$ The acceleration of atom *i*

T The kinetic energy

U Potential function

w_{ij} Weight function of atom

w_l Weight function of element

σ_{nn} The normal stress

σ_{nm} The shear stress

ε_{nn} The normal strain

ε_{mn} The shear strain

π_p The potential energy

ν Poisson's ratio

Chapter 1 Introduction

1.1 Motivation

In general, mechanical properties such as the elastic modulus and hardness of the nano-thin film can be measured by nanoindentation techniques. In recent years, the measurement of the operation specimen by nanoindentation techniques was fallen below the level of 100 nm [1-2]. Accordingly, these techniques provide researchers an excellent opportunity to obtain the characteristics of the material properties of nano-thin films. However, the experimental method of nanoindentation measurement on nano-thin films is not easy to accomplish, both because the experimental techniques are on the atomic-scale level, and because it is difficult to investigate the transient atomic information inside the specimen during the nanoindentation process. Therefore, theoretical methods can accompany experimental techniques to provide much useful information without the limitations of the experimental method. Though the theoretical method is useful for analysis of nanoindentation on the nanoscale, it must be passed through the numerical method in order to completely observe the variations in the process of nanoindentation. Correspondingly, molecular dynamics (MD) simulation, which is suitable for nanoindentation analysis under nanoscale, is a powerful numerical method to describe the detailed variations at the atomic scale.

MD simulation studies were initiated in the late 1950s at the Lawrence Radiation Laboratory (LRL) by Alder and Wainwright [3-4] in the field of equilibrium and non-equilibrium statistical mechanics. The application of MD simulation to the cutting and indentation process was first introduced at Lawrence Livermore National Laboratory (LLNL) in the late 1980s and early 1990s [5-6]. Pioneering research in the field of MD

simulations of indentation was conducted by Landman et al [7-10] at the Georgia Institute of Technology, followed by Belak and his colleagues at the Lawrence Livermore National Laboratory (LLNL). Since then, MD simulation has been applied to a wide range of fields, including crystal growth, low-pressure diamond synthesis, laser interactions, nanometric cutting [11-17], indentation [18-22], and tribology [23-27]. Nowadays, MD methods using empirical interatomic potentials can be implemented in simulating large-scale systems of up to ten million atoms [28-29].

1.2 Nanoindentation of Crystal Metal Orientation Surfaces

Recently, considerable attention has been devoted to atomic scale processes and the measurable techniques of materials. Specifically, the material properties of substrates of nanoscale thickness have received attention because of the specific characteristics of their mechanical and physical properties [30-31]. Nickel is one of the favored materials for either reactively or catalytically forming a smooth electroless deposition of additional thin layers in order to provide enhanced magnetic read-write capability on magnetic memory disks [32-33]. In micro electro-mechanical system (MEMS) application, nickel has been found to have excellent mechanical and magnetic properties that can be exploited to realize movable structures [34-37]. At this small scale, the macroscale deformation of the bulk material will be less significant than the influences of different local atomic arrangement or the surface orientation upon which a nanoscale deformation mechanism imposes an external force [38]. This study examines the relationships between material properties and deformation mechanisms of surfaces of different crystallographic orientations under nanoscale, because they can provide significant information for the manufacture and design of nano-components, one of

nanotechnology's promising applications.

However, because of the limitation of the experimental indentation equipment, research is rarely published that focuses on the influence of different surface orientations on the mechanical properties of the indentation substrate during nanoindentation. Even for molecular dynamics simulations, there are no complete and systematic discussions on this topic. In related studies, Mante et al [39] performed an investigation of the elastic modulus and hardness of selected crystallographic planes of single crystal titanium using a mechanical properties microprobe (MPM). Gouldstone et al [1] utilized nanoindentation experiments on thin film of polycrystalline aluminum of known texture and different thicknesses, and of single crystal aluminum of different crystallographic orientations. Wang et al [40] presented a study about the dependence of nanoindentation pile-up patterns and of micro-textures on the crystallographic orientation using high purity copper single crystals. Komanduri et al [27] utilized MD simulations of nanoindentation followed by nanoscratching conducted on single crystal aluminum (with the crystal set up in the (001) [100] orientation and with scratching performed in the [100] direction) at extremely fine scratch depths (from 0.8 nm to near zero) to investigate atomic-scale friction. Subsequently, Komanduri et al [41] used MD simulations to investigate the effect of crystallographic factors (crystal orientation and direction of scratching) in indentation and scratching conducted on single crystal aluminum at specific combinations of orientations {(111), (110), (001), ($\bar{1}$20)} and scratch directions <[$\bar{1}$10], [$\bar{2}$11], [100], [210], [221]>. Kum [42] performed MD simulations to study anisotropic features in nano-mechanical properties at the surface of nickel single crystals as a function of indenter size and velocity for three crystallographic orientations: (100),

(110), and (111).

For the previously mentioned research, although Komanduri [27, 41] performed MD simulations of nanoindentation to study the influences of crystallographic factors on FCC metals in indentation and scratching, the only material used in the simulated models is single crystal aluminum. Moreover, the atomic phases depicting deformation in the simulated models are only presented in 2D morphologies, and neither the homogeneous nucleation nor the dislocation sliding of plastic deformation are clearly visible during indentation and scratching. In addition, although Kum [42] performed MD simulations to investigate the orientation effects of elastic-plastic deformation on (100), (110), and (111) crystallographic orientations of nickel substrates—which is similar to our current investigation—the main aim of Kum's research was to calculate the parameters of power law on the initial stage of the indentation curve in order to obtain the nano-mechanical properties of elastic deformation. The plastic deformation characteristics of dislocation and nucleation in the course of indentation were not presented in the study, and the influences of three crystallographic orientations on the mechanical properties of both the hardness and the elastic modulus were not discussed [42]. Therefore, the main purpose of this paper is to use MD simulations of nanoindentation to analyze the influences of both plastic deformation characteristics and of atomic stress variations on the material properties of different crystallographic nickel substrates during nanoindentation, compensating for the experimental limitation of nanoindentation-particularly for pure nickel substrates of three crystallographic orientations. The notable results of our research include the presentation of 3D atomic phases of plastic deformation induced by indentation corresponding to atomic stress distributions, diagrams of the pile-up patterns

at the maximum indentation depth, and the extracted material properties from the indentation curves for (100), (110), and (111) crystallographic orientations of nickel substrates in the course of nanoindentation.

1.3 Nanoindentation of Multiscale Crystal Metals

Over the years a number of approaches have been developed to simulate dynamics in condensed phases. In the atomistic regime, the molecular dynamics (MD) simulation technique has been successfully carried out to investigate the mechanical behaviors of structures on nanoscale [43-46]. Because of the availability of accurate interatomic potentials for a range of materials, classical MD simulations have become prominent as a tool for elucidating complex physical phenomena. However, the length and time scales that can be probed using MD are still fairly limited. In principle, length scales of MD simulations could be made larger, but simulations with 10^{10} particles must be performed by the most advanced computers currently available, in despite of the real physical systems usually containing 10^{23} particles [47]. Therefore, for the study of nanoscale mechanics and materials, the analytic model up to a scale of several microns, consisting of billions of atoms, which is too large for MD simulations.

Current parallel supercomputers can deal with up to billions of atoms, where the spatial size is still in sub-micro meters. Similarly, in regard to the temporal scale calculations, the parallel algorithm in MD simulations is still very difficult to achieve a realistic condition as compared with the experiments to date. Consequently, it is currently impossible to model an entire macroscopic domain with atoms by using MD simulations, despite the recent advances in computational power. By contrast, the finite element method (FEM) can be successfully modeled to describe the physical phenomenon passing

through material on macroscopic scale [48,49]. By means of FEM analysis, the analytic model for the scientific problems can be simply solved by the highly efficient calculation, tying in parallel algorithm with FEM simulations, which significantly enlarge to a practical time and length scales. Besides, it has also a strong point for the quantitative and qualitative precision in the continuum analysis on the macroscopic scale. However, it is not always powerful in some circumstances, especially for the descriptions of the atomic behavior at the microscopic scale. For the FEM approach, the major shortcoming in the numerical analysis lies in the constitutive relations, governed by the continuum theory, which is incapable to obtain the precise solutions under the effect of nanoscale [50]. Additionally, FEM simulations tend to fail for the phenomenal descriptions at the atomic scale due to the inability of continuum models to describe defects. Despite these efforts, it is unclear whether a convergent solution for the correct phenomenology can in fact be reached.

A remarkable approach can be solved for the above-mentioned problems, which had been recently proposed in many researches, namely multiscale methodology. It is to combine a MD simulation for the central regions within the system with a FEM for a continuum description of the remainder of the system. By the use of multiscale analysis, it can be applied to many problems that a critical region or regions, much smaller than the overall computational domain, is defined using atomic level descriptions capable of producing appropriate behavior at the nanoscale; meanwhile, outside of the atomistic region, where strain fields are smoothly varying, continuum mechanics is used to describe the material deformation behavior over larger length scales. Accordingly, multiscale methods are a class of simulation methods that have become useful and

important within the past decade [50]. Much of this is due to the fact that the governing physics and mechanics of deforming media have been elucidated over the course of time. Another crucial factor at play is the recent explosion in computational power. As combining the two scale approaches, the multiscale method leads straight towards a new revolution in computational mechanics.

With regard to the literature review for the proposed research of multiscale method in the past decades, a classic example is the pioneering work of Clementi and coworkers [51] in 1980s where they used quantum mechanics, atomistic dynamics, and fluid dynamics to predict the tidal circulation in Buzzard's Bay Massachusetts. They first used high quality quantum mechanical methods to evaluate the interaction of several water molecules. Since then, multiscale simulation has been applied to the various fields, including nanocomponent analysis [52-55], crack fracture analysis [51,53,55,56-61], wave propagation [57,62], nanoindentation [53,63-67], nanometric cutting [47], and stress distribution analysis [68-69]. Nowadays, there were many methodologies to couple MD and FEM which had been successfully developed. Systematically, these methodologies can be classified into several categories: the bridging scale method (BSM) [50,52,56-57,70-74], meshfree particle method (MPM) [53-54], the quasicontinuum method (QCM) [47,58,63-67,75-76], the coarse-grained molecular dynamics (CGMD) [77], the coupled atomistic dislocation dynamics (CADD) [78-80], the macroscopic atomistic ab initio dynamics (MAAD) [51,60], the coupling of length scales method (CLS) [55,59], and the finite element and atomistic method (FEAt) [61,81-82]. As the present article is not intended as an exhaustive review, the interested reader can refer to the multiple scale review papers of Curtin et al. [80], and Liu et al. [83].

Among these previously mentioned literatures of multiscale research, a widely used approach is to implement the coupling through a so-called “handshake” region, which is essentially the interface between the MD and FEM regions. In this method, the finite element mesh is graded down to the atomic lattice size in an overlap, or ‘‘handshake’’, region; the dynamics is governed by a total Hamiltonian function that combines the separate Hamiltonians of the different regions in an appropriate way [51,55,59-62,68-69,78-79,80-82,84]. In the handshake region, a certain weighted factor is performed between the MD description and the coarse grid description. These researches briefly include: Dewald et al. [78] employed the CADD method to quantify the error in dislocation driving forces for dislocations near the atomistic/continuum interface. Abraham [51] utilized the MAAD method to simulate the crack growth of solid silicon slab corresponding to the stress wave propagation. Rudd et al. [55] performed the multiscale simulations of dynamical systems at finite temperature using the CLS method with applications in fracture and Micro-Electro-Mechanical Systems (MEMS). Izumi et al. [82] used the FEAt method to analyze the shear-strain dominant field of silicon flat. Lidorikis et al. [69] adopted the CLS method to study the stress distributions in the interface of silicon/silicon-nitride nanopixels. Liu [68] et al. established a full 3D model with a combination of MD and FE by the overlapping transition zone to study the stress distributions in an epitaxial island.

In this paper, a newly coupled method of the weighted function using the handshake region to combine MD and FE, proposed by Lidorikis et al. [69,84], was adopted in our hybrid FE/MD simulations, because this method exhibits a simple characteristic and fits in with our demand for coupling the MD and FE regions. We take nanoindentation as an

investigation problem for assessing the performance of the coupled method involving multiple length scales, and confirm the accuracy of our hybrid model as compared with the results of full MD simulations. The present results of nanoindentation simulations are performed in the prototype FCC transition metal nickel (Ni). By means of the multiscale approach, it can be allow for the consideration of large volumes of material and hence for the minimization of unwanted effects induced by the limited size of the specimen and by the boundary conditions.

1.4 Nanoindentation of Crystal Metal Semiconductors

The development of microsystems and nanotechnology has relied, in many ways, on the major progress accomplished in surface science and materials science and, in particular, thin film technology. In the past, much effort has been devoted to characterizing the optical, electrical and magnetic properties of the resultant structures and devices. Recently, it has become clear that, in order to fully harvest the unprecedented potential of the emerging nanotechnologies in general, the processes-induced structural and mechanical modifications on the materials might be equally important. For instance, over the last two decades, gallium nitride (GaN) epitaxial films and devices have attracted considerable attention because of their broad applications in blue/green light emitting diodes [85], laser diodes and photodetectors [86], as well as high-power or high-temperature electronics [87]. However, the successful fabrication of devices based on epitaxial GaN thin films requires a better understanding of the mechanical characteristics in addition to their optical and electrical performance, since the contact loading during processing or packaging can significantly degrade the performance of these devices. Consequently, there is a growing demand for investigating

the mechanical characteristics of materials, in particular in the nanoscale regime, for device applications.

In trying to mimic the contact loading frequently encountered in wire-bonding packaging, there are several issues to be addressed. Firstly, the mechanical responses of a thin film to an applied load might be vastly different from that of the same bulk material. For this purpose, unfortunately, the traditional methods such as tensile measurements do not scale well into the micrometre and nanometre scale. Secondly, the role of structural changes under contact loading are largely underestimated owing to the difficulties in probing the structural characterizations of thin films affected by the contact interaction directly. In this respect, the advent of nanoindentation instruments and the subsequent development of the underlying science may potentially address the scaling issue and the scientific evaluation of all contact loading related phenomena. Since the deformation that occurred during the test is controlled locally on the nanometre scale, nanoindentation has, recently, been widely used to investigate the deformation mechanisms of various semiconductors [88–90], in combination with the molecular dynamics simulations for analysing the atomic interactions [91–93]. In addition, the mechanical properties of surfaces of solids and thin films, such as the hardness and Young's modulus, have been extracted using this technique [94-96].

Despite the successes obtained from the nanoindentation studies in GaN thin films, this technique itself does not provide direct information on subsurface deformation mechanisms, crack initiation and dislocation propagation. Therefore, complementary methods capable of providing such information are needed. In most nanoindentation studies, both Raman microspectroscopy [89] and plan-view TEM [90] techniques have

been successfully used to analyse the phase transformation and defect/dislocations propagation along the horizontal direction of materials. However, they are inadequate to distinguish the phase changes inside the deformed zone along the direction of the concentrated applied stress. The focused ion beam (FIB) miller, which is now widely used for a range of material characterization applications [88], is an excellent tool for preparing transmission electron microscopy samples to reveal the cross-sectional microstructure of the locally deformed regions. In this report, we employed this method to investigate the subsurface deformation structures as well as the possible substrate deformations involved in the Berkovich nanoindentation performed on GaN films, compensating for the numerical limitation of nanoindentation-particularly for MD simulation. The detailed microstructure evolution resulting from the perpendicularly contact-induced deformed region was examined to correlate with the features exhibited in the obtained load–displacement measurements.

Chapter 2 Theory

2.1 Governing Equation of Molecular Dynamics

Molecular dynamics (MD) has been widely used to simulate properties of liquids, solids, and molecules in several research disciplines. It is an important approach to understand microscopic character of nature. MD is derived form a new concept called, phase trajectory. We computed the trajectories of molecules using classical Newtonian mechanics and we described features of the molecule trajectory in classical nonlinear dynamics. And obtain properties by analyze the trajectory with kinetic theory, statistical mechanics, and sampling theory. In addition, periodic boundary conditions and conservation principles are used to hold accuracy of MD simulation. Combined these tools form the foundation of molecular dynamics. Newtonian second law can be expressed as follows:

$$F_i = m\ddot{r}_i = m\frac{d^2 r_i}{dt^2} \tag{2.1}$$

where r_i is the position vector of molecule *i* as shown in Fig. 2.1. Since Newton's second law is time independent or equivalently. Equation (2.1) is invariant under time translations. Consequently, we expect there to be some functions of the positions and velocities whose value is constant in time; this function is called the Hamiltonian, as follows:

$$H(r^N, P^N) = const \tag{2.2}$$

where $p_i = m\dot{r}_i$ is the momentum of molecule *i*. For an isolated system, total energy *E* is conserved, where *E* is equal to the sum of kinetic energy and potential energy. Thus,

for an isolated system, we identify total energy as the Hamiltonian; then for N spherical molecules, H can be written as

$$H(r^N, p^N) = \frac{1}{2m}\sum_i p_i^2 + U(r^N) = E \tag{2.3}$$

where $U(r^N)$ results from the intermolecular interactions. First consider the total time derivative of the general Hamiltonian (2.2)

$$\frac{dH}{dt} = \sum_i \frac{\partial H}{\partial p_i}\cdot \dot{p}_i + \sum_i \frac{\partial H}{\partial r_i}\cdot \dot{r}_i + \frac{\partial H}{\partial t} \tag{2.4}$$

if, as is (2.3), H has no explicit time dependence, then the last term on the RHS of (2.4) vanishes and we are left with, due to H=const

$$\frac{dH}{dt} = \sum_i \frac{\partial H}{\partial p_i}\cdot \dot{p}_i + \sum_i \frac{\partial H}{\partial r_i}\cdot \dot{r}_i = 0 \tag{2.5}$$

If Hamiltonian is expressed as (2.6), then

$$\frac{dH}{dt} = \frac{1}{m}\sum_i p_i \cdot \dot{p}_i + \sum_i \frac{\partial U}{\partial r_i}\cdot \dot{r}_i = 0 \tag{2.6}$$

On comparing (2.5) and (2.6), we find for each molecule i

$$\frac{dH}{dp_i} = \frac{p_i}{m} = \dot{r}_i \tag{2.7}$$

$$\frac{\partial H}{\partial r_i} = \frac{\partial U}{\partial r_i} \tag{2.8}$$

Substituting (2.7) into (2.5) gives

$$\sum_i \dot{r}_i \cdot \dot{p}_i + \sum_i \frac{\partial U}{\partial r_i}\cdot \dot{r}_i = 0 \tag{2.9}$$

$$\sum_i (\dot{p}_i + \frac{\partial H}{\partial r_i})\cdot \dot{r}_i = 0 \tag{2.10}$$

Since the velocities are all independent of one another, equation (2.10) can be satisfied only, for each molecule *i*, we have

$$\frac{\partial H}{\partial r_i} = -\dot{p}_i \tag{2.11}$$

Equation (2.7) and (2.11) are Hamilton's motion equation. For a system of *N* particles, Equation (2.7) and (2.11) represent 6*N* first-order differential equations that are equivalent to Newton's 3*N* second-order differential equation (2.1).

In the Newtonian view, motion is a response to an applied force. However, in the Hamiltonian view, motion occurs in such a way as to preserve the Hamiltonian function, where the force does not appear explicitly. For an isolated system, the particles move in accordance with Newton's second law, tracing our trajectories that can be represented by time-dependent position vectors $r_i(t)$. Similarly, we also have time-dependent momentum $p_i(t)$. At one instant, there are positions and momenta of the *N* particles in a 6*N* dimensional hyperspace. Such a space, called phase space, is composed of two parts: a 3*N*-dimensional configuration space, in which the coordinates are the components of position vectors $r_i(t)$, and a 3*N*-dimensional momentum space (or velocity space), in which the coordinates are the components of the momentum vectors $p_i(t)$. As time evolves, the points defined by positions and momentum in the 6*N* phase space moves, describing a trajectory in phase space.

2.2 Tight-Binding Potential

It is widely recognized that empirical many-body potentials can reproduce with good accuracy the thermodynamic and structural properties of most transition metals [98].

In the last years, these potentials have been extensively used to analyze a variety of problems in materials science by MD computer simulations. The main advantage of a many-body treatment over the conceptually and practically simpler pair-potential description is the ability to better reproduce some basic features of metallic systems. A relatively simple scheme for relating the atomic and electronic structure, without resorting to the complex treatment of first-principles calculations, is the Tight-Binding (TB) potential. The pair-wise intermolecular potential form as follow:

$$U_{total} = \sum_{i=1}^{N} \left\{ -\left[\sum_{j} \xi^2 \exp\left(-2q \left(\frac{r_{ij}}{r_o} - 1 \right) \right) \right]^{1/2} + A \exp\left[-p \left(\frac{r_{ij}}{r_o} - 1 \right) \right] \right\} \tag{2.12}$$

where the subscripts i and j represent atom i and atom j, respectively, ξ is an effective hopping integral, r_{ij} is the distance between atoms i and j, and r_0 is the first-neighbors' distance. The total band energy is characterized by the second moment of the d-band density of state and is shown in the first part of the potential function. Meanwhile, the second part reveals a modified form of the original tight-binding potential. The free parameters of A, ξ, p and q are fitted to the experimental values of cohesive energy, lattice parameters (by the constraint on the atomic volume), and independent elastic constants for each pure system and for alloys. The interaction force F_i on atom i is derived from the equation (1), can be expressed as

$$F_i = -\sum_{j \neq i}^{N} \left(\frac{\partial \Phi_{ij}}{\partial r_{ij}} + \frac{\partial \Phi_{ij}}{\partial r_{ij}} \right) = m_i \frac{d^2 r_i(t)}{d t^2} \tag{2.13}$$

where m_i is the mass of atom i, r is the position of atom i, and N is the total number of atoms. By using equation (2.13), the resultant forces of each individual atom can be calculated at each time step.

2.3 Initial Conditions

1. A minimum requirement for the MD simulation to be valid is that the results of a simulation of adequate duration are insensitive to the initial state, so any convenient initial state is allowed.
2. A particular simple but practical choice is to start with the particles at the sites of some regular lattice, e.g., the square or simple cubic lattice, and spaced to give the desired density.
3. The velocities are assigned random directions and a fixed magnitude based on temperature.
4. The speed of equilibration to a state in which there is no memory of this arbitrarily selected initial configuration is normally quite rapid, so that more careful attempts at the constructing a "typical" state are of little benefit.
5. For FCC lattice, there are four atoms per unit cell, and the system is centered at the origin.
6. The velocity magnitude is fixed, each velocity vector is assigned a random direction, and the velocities are then adjusted to ensure that the center of mass is at rest.
7. For leapfrog method, if the users do not care the minor difference between $t = 0$ and $t = \Delta t / 2$ in setting the initial velocities, then there is no further work required. If the difference is not to be overlooked, a single interaction computation is all that is required.

2.4 Periodic Boundary Condition

Unless the purpose of the MD simulation is to capture the physics near real walls, a problem that is actually of considerable importance, walls are better eliminated by using

periodic boundary conditions (PBC). Physical meaning of periodic boundary conditions is shown in Fig. 2.3. The introduction of PBC is equivalent to considering an infinite space-filling array of identical copies of simulation region. There are some consequences of this PBC:

1. A particle that leaves the simulation region through a particular bounding face immediately reenters the region through the opposite face.
2. A wraparound effect needs to be considered. Particles lying within a distance r_c of a boundary interact with particles in an adjacent copy of the system, or, equivalently, with particles near the opposite boundary.
3. This wraparound effect of the PBC must be taken into account in both the integration of the equations of motion and the interaction computations. (Checking the coordinates of particles if they move outside the region.)
4. Periodic boundary conditions are most easily handled if the region is rectangular in two dimensions, or a rectangular prism in three dimensions. This is not an essential requirement, and any space-filling convex region can be used, although the boundary computation is not as easy as those in rectangular one. The motivation to choose alternative region shapes is to enlarge the volume to surface ratio, thus increase the maximum distance between particles before periodic ambiguity appears.
5. Using PBC will restrict the interaction range to no more than half the smallest region dimension.
6. Even with PBC, finite-size effects are still present. So how big the simulation region should be? It depends on what kind of system and the properties of the interest. As a minimum requirement, the size should exceed the range of any significant

correlations. Only detailed numerical experiments can hope to resolve this question.

2.5 Rescaling Method

Rescaling method keep wall isothermal by modify total kinetic energy. In microcosmic size, temperature is related to kinetic energy, when we set the temperature of correction layer, it means to set the average kinetic energy of atoms on the correction layer, so we must keep he kinetic energy fixed. (Equation (2.14)), so we have a reference value. Then, use equation (2.15) we compute the total kinetic energy of atoms. Finally, we start rescaling by using equation (2.16) to make the total kinetic energy in the correction layer is the same as reference value which we computed in equation (2.15)

$$E_{kd} = \frac{3}{2} N k_B T_d \tag{2.14}$$

$$E_{ka} = \frac{1}{2} m \sum_{i=1}^{N} V_i^{old\,2} = \frac{3}{2} N k_B T_a \tag{2.15}$$

$$V_i^{new} = V_i^{old} \cdot \sqrt{\frac{E_{kd}}{E_{ka}}} = V_i^{*} \cdot \sqrt{\frac{T_d}{T_a}} \tag{2.16}$$

where N is total atoms in the correction layer; k_B is Boltzmann constant; E_{kd} is the total kinetic energy defined by T_d; E_{ka} is the total kinetic energy of atoms in the correction layer; T_d is the boundary temperature which we need; T_a is the average temperature of atoms in the correction layer before modification; V_i^{old} is the velocity of atom in the correction layer before modification; V_i^{new} is the velocity of atom in the correction layer after modification.

2.6 Cell Link List Combined Verlet List

Basic idea of this method is to divide the simulation region into a lattice of small cells, and that the cell width exceeds r_c . If particles are assigned to cells based on their instantaneous positions, then it is obvious that interactions are only possible between particles that are either in the same cell or in immediately adjacent cells. Because of symmetry only half the neighboring cells need to be considered. For example, a total of 14 neighboring cells must be examined in three dimensions (include the cell itself). In addition, the wraparound effects can be readily incorporated into the scheme. In general, the region size must be at least 4 r_c for this method to be useful.

There are several ways of implementing this cell link list method to connect the relation between particles and cells. In the current demonstration code, it utilizes concept of the pointers for particles and cells. Each cell stores a particle number, which may be zero or nonzero. Nonzero value represents a true particle number, while the zero value represents either the last atom in the cell or an empty cell. In addition, only one array cell list is used to represent the particles and cells. The obvious advantage of doing this is we know exactly the size of this array in advance if periodic boundary conditions are used. Of course, there are several other methods to implement this idea of cell link list technique. Ideas depicting in the above can be clearly illustrated as Fig. 2.4.

A list of all particle pairs with separation $r_{\max} > r_c$ is maintained and updated every say 10 or 20 time steps. $r_{\max}$ is chosen large enough that it is unlikely that a particle pair not in the list will come closer than r_c before the list is updated. It is also possible to decide automatically when the neighbor list needs to be updated. When the list is created, a vector for each particle is set to zero. At each time step, the vector is incremented by the

particle displacement. For example, see the Fig. 2.5. We could combine cell link method and Verlet list method, see Fig. 2.6; by this way, it could promote the performance of the simulation.

2.7 Leap-Frog Method

Leapfrog method is completely equivalent algebraically and yield coordinates that are accurate to third order in Δt. However, it tends to be considerably better than the higher-order methods from the viewpoint of energy conservation. In addition, their storage requirements are also minimal. The derivation of the Verlet formula follows immediately from the Taylor expansion of the coordinate variable typically $x(t)$

$$x(t+h) = x(t) + h\dot{x}(t) + (h^2/2)\ddot{x}(t) + O(h^3) \tag{2.17}$$

where t is the current time, and $h \equiv \Delta t$. Here, $\dot{x}(t)$ is the velocity component, and $\ddot{x}(t)$ the acceleration or force $f(t)$ in reduced MD units. Note that although $\ddot{x}(t)$ has been expressed as a function of *t*, it is actually a known function via the force law of the coordinates at time *t*. After rearrange equation (2.17), we obtain

$$x(t+h) = 2x(t) - x(t-h) + h^2\ddot{x}(t) + O(h^4) \tag{2.18}$$

The truncation error is of order $O(h^4)$ because the h^3 term cancels. A possible disadvantage of equation (2.18) is that at low machine precision the h^2 term multiplying the acceleration may prove a source of inaccuracy. The velocity is not directly involved in the solution, but if required it can be obtained from

$$\dot{x}(t) = [x(t+h) - x(t-h)]/2h + O(h^2) \tag{2.19}$$

with higher-order expression based on values from earlier time steps available if needed, though rarely used. The leapfrog method is equally simple to derive. Rewrite the Taylor

expansion as

$$x(t+h) = x(t) + h[\dot{x}(t) + (h/2)\ddot{x}(t)] + O(h^3) \tag{2.20}$$

The term multiplying h is just $\dot{x}(t+h/2)$, so equation (2.20) becomes (2.22) below. The leapfrog integration formulate are then

$$\dot{x}(t+h/2) = \dot{x}(t-h/2) + h\,\ddot{x}(t) \tag{2.21}$$

$$x(t+h) = x(t) + h\,\dot{x}(t+h/2) \tag{2.22}$$

The fact that coordinates and velocities are evaluated at different times dose not present a problem; if an estimate for $\dot{x}(t)$ is required there is a simple connection that can be expressed in either of two ways:

$$\dot{x}(t) = \dot{x}(t \mp h/2) \pm (h/2)\,\ddot{x}(t) \tag{2.23}$$

The initial conditions can be handled in a similar manner, although a minor inaccuracy in describing the starting state, namely, the distinction between $\dot{x}(0)$ and $\dot{x}(h/2)$, is often ignored.

2.8 Atomic Decomposition Algorithm

In the atom decomposition method, as shown in Fig. 2.7, each processor, which owns nearly the same number of atoms as other processors and in which atoms are not necessarily geometrically nearby, integrates the Newton's equation for all atoms and moves the atoms of their owns. However, this method requires global communication at each time step, which becomes unacceptably expensive as compared with the “useful” MD computation when the number of atoms increase to a certain amount, since each processor has to know all information (position and velocities) of all atoms at each time step. On equivalently, the communication is $O(N)$, where N is the number of atoms in the

system that is independent of the number of the processors, P. Thus, the atom decomposition method is generally suitable for small-scale problem.

2.9 Governing Equation of Finite Element Method

In dynamic problems the displacements, velocities, strains, stresses and load are all time-dependent. The procedure involved in deriving the finite element equations of a dynamic problem can be stated by the following step:

Step1: Idealize the body into *E* finite elements.

Step 2: Assume the displacement model of element *e* as

$$\vec{U}(x,y,z,t)=\begin{Bmatrix}u(x,y,z,t)\\v(x,y,z,t)\\w(x,y,z,t)\end{Bmatrix}=[\,N(x,y,z,t)\,]\,\vec{Q}^{(e)}(t) \tag{2.24}$$

where $\vec{U}$ is the vector of displacements, $[N]$ is the matrix of shape functions and $\vec{Q}^{(e)}$ is the vector of nodal displacements which is assumed to be a function of time *t*.

Step 3: Derive the element characteristic (stiffness and mass) matrices and characteristic (load) vector. From equation (2.24), the strain can be expressed as

$$\vec{\varepsilon}=[B]\,\vec{Q}^{(e)} \tag{2.25}$$

and the stress as

$$\vec{\sigma}=[D]\,\vec{\varepsilon}=[D][B]\,\vec{Q}^{(e)} \tag{2.26}$$

By differentiating equation (2.26) with respect to time, the velocity field can be obtained as

$$\dot{\vec{U}}(x,y,z,t)=[\,N(x,y,z)\,]\,\dot{\vec{Q}}^{(e)}(t) \tag{2.27}$$

where $\dot{\vec{Q}}^{(e)}$ is the vector of nodal velocities. To derive the dynamic equations of motion

of a structure, we can use either Lagrange equations [105]. The Lagrange equations are given by

$$\frac{d}{dt}\left\{\frac{\partial L}{\partial \dot{Q}}\right\}-\left\{\frac{\partial L}{\partial Q}\right\}+\left\{\frac{\partial R}{\partial \dot{Q}}\right\}=\{0\} \tag{2.28}$$

where

$$L = T - \pi_p \tag{2.29}$$

is call the Lagrangian function, T is the kinetic energy, π_p is the potential energy, R is the dissipation function, Q is the nodal displacement and $\dot{Q}$ is the nodal velocity. The kinetic and potential energies of an element "e" can be expressed as

$$T^{(e)} = \frac{1}{2}\iiint_{V^{(e)}} \rho \dot{\vec{U}}^T \dot{\vec{U}}\, dV \tag{2.30}$$

and

$$\pi_P^{(e)} = \frac{1}{2}\iiint_{V^{(e)}} \varepsilon^T \vec{\sigma}\, dV - \iint_{S_1^{(e)}} \vec{U}^T \vec{\Phi}\, dS_1 - \iiint_{V^{(e)}} \vec{U}^T \vec{\phi}\, dV \tag{2.31}$$

where $V^{(e)}$ is the volume, ρ is the density and $\dot{\vec{U}}$ is the vector of velocities of element e. By assuming the existence of dissipative forces proportional to the relative velocities, the dissipation function of the element e can be expressed as

$$R^{(e)} = \frac{1}{2}\iiint_{V^{(e)}} \mu \dot{\vec{U}}^T \dot{\vec{U}}\, dV \tag{2.32}$$

where μ can be called the damping coefficient. In equation (2.30) to (2.32), the volume integral has to be taken over the volume of the element and in equation (2.32), the surface integral has to be taken over that portion of the surface of the element on which distributed surface forces are prescribed. By using equation (2.24) to (2.26), the

expressions for T, π_p and R can be written as:

$$T = \sum_{e=1}^{E} T^{(e)} = \frac{1}{2}\dot{\vec{Q}}^T \left[\sum_{e=1}^{E} \iiint_{V^{(e)}} \rho [N]^T [N] dV \right] \dot{\vec{Q}} \tag{2.33}$$

$$\begin{aligned} \pi_P = \sum_{e=1}^{E} \pi_P^{(e)} &= \frac{1}{2}\vec{Q}^T \left[\sum_{e=1}^{E} \iiint_{V^{(e)}} [B]^T [D][B] dV \right] \vec{Q} \\ &- \vec{Q}^T \left(\sum_{e=1}^{E} \iint_{S_1^{(e)}} [N]^T \vec{\bar{\Phi}}(t)\, dS_1 + \iiint_{V^{(e)}} [N]^T \vec{\bar{\phi}}(t)\, dV \right) - \vec{Q}^T \vec{P}_c(t) \end{aligned} \tag{2.34}$$

$$R = \sum_{e=1}^{E} R^{(e)} = \frac{1}{2}\dot{\vec{Q}}^T \left[\sum_{e=1}^{E} \iiint_{V^{(e)}} \mu [N]^T [N] dV \right] \dot{\vec{Q}} \tag{2.35}$$

where $\vec{Q}$ is the global nodal displacement vector, $\dot{\vec{Q}}$ is the global nodal velocity vector, and $\vec{P}_c$ is the vector of concentrated nodal forces of the structure or body. By defining the matrices involving the integrals as

$$\left[M^{(e)} \right] = \text{element mass matrix} = \iiint_{V^{(e)}} \rho [N]^T [N] dV \tag{2.36}$$

$$\left[K^{(e)} \right] = \text{element stiffness matrix} = \iiint_{V^{(e)}} [B]^T [D] [B] dV \tag{2.37}$$

$$\left[C^{(e)} \right] = \text{element damping matrix} = \iiint_{V^{(e)}} \mu [N]^T [N] dV \tag{2.38}$$

$\vec{P}_s^{(e)}$ = vector of element nodal forces produced by surface forces

$$= \iint_{S_1^{(e)}} [N]^T \vec{\bar{\Phi}} \cdot dS_1 \tag{2.39}$$

$\vec{P}_b^{(e)}$ = vector of element nodal forces produced by body forces

$$= \iiint_{V^{(e)}} [N]^T \vec{\bar{\phi}} \cdot dV \tag{2.40}$$

Step 4: Assemble the element matrices and vectors and derive the overall system equations of motion. Equation (2.33) to (2.35) can be written as

$$T = \frac{1}{2}\dot{\vec{Q}}^T [M] \dot{\vec{Q}} \tag{2.41}$$

$$\pi_p = \frac{1}{2}\vec{Q}^T [K] \vec{Q} - \vec{Q}^T \vec{P} \tag{2.42}$$

$$R = \frac{1}{2}\dot{\vec{Q}}^T [C] \dot{\vec{Q}} \tag{2.43}$$

where

$$[M] = \text{master mass matrix of the structure} = \sum_{e=1}^{E} \left[M^{(e)} \right] \tag{2.44}$$

$$[K] = \text{master stiffness matrix of the structure} = \sum_{e=1}^{E} \left[K^{(e)} \right] \tag{2.45}$$

$$[C] = \text{master damping matrix of the structure} = \sum_{e=1}^{E} \left[C^{(e)} \right] \tag{2.46}$$

$$\vec{P}(t) = \text{total load vector} = \sum_{e=1}^{E} \left[P_s^{(e)}(t) + P_b^{(e)}(t) \right] + \vec{P}_c(t) \tag{2.47}$$

By substituting equation (2.42) to (2.44) into equation (2.29), we obtain the desired dynamic equations of motion of the structure or body as

$$[M] \ddot{\vec{Q}}(t) + [C] \dot{\vec{Q}}(t) + [K] \vec{Q}(t) = \vec{P}(t) \tag{2.48}$$

where $\ddot{\vec{Q}}$ is the vector of nodal accelerations in the global system. If damping is neglected, the equations of motion can be written as

$$[M] \ddot{\vec{Q}}(t) + [K] \vec{Q}(t) = \vec{P}(t) \tag{2.49}$$

Steps 5 and 6: Solve the equations of motion by applying the boundary and initial conditions. Equation (2.48) or (2.49) can be solved by using the techniques of a set of

simultaneous linear differential equations for propagation problems. Once the time history of nodal displacements, $\vec{Q}(t)$, is known, the time histories of stresses and strains in the elements can be found as in the case of static problems. Special space-time finite elements have also been developed for the solution of dynamic solid and structural mechanics problems [106-107].

2.10 Element Stiffness Matrix

The element stiffness matrix is given by

$$\left[K^{(e)}\right] = \iiint_{V^{(e)}} [B]^T [D] [B] dV \tag{2.50}$$

Since the matrix $[B]$ is expressed in natural coordinates, it is necessary to carry out the integration in equation (2.50) in natural coordinates too, using the relationship

$$dV = dx\,dy\,dz = \det [J] \cdot dr\,ds\,dt \tag{2.51}$$

Thus equation (2.50) can be rewritten as

$$\left[K^{(e)}\right] = \int_{-1}^{1}\int_{-1}^{1}\int_{-1}^{1} [B]^T [D][B] \det [J] dr\,ds\,dt \tag{2.52}$$

2.11 Numerical Computation

Since the matrix $[B]$ is an implicit (not explicit) function of *r*, *s* and *t*, a numerical method has to be used to evaluate the multiple integral of equation (2.52). The Gaussian quadrature has been proved to be the most efficient method of numerical integration for this class of problems. By using the two-point Gaussian quadrature, which yields sufficiently accurate results, equation (2.52) can be evaluated as [108]:

$$\left[K^{(e)}\right] = \sum_{r=R_i=R_1}^{R_2} \sum_{s=S_j=S_1}^{S_2} \sum_{t=T_k=T_1}^{T_2} \left[\left([B]^T [D] [B] \cdot \det [J] \right) \Big|_{(R_i, S_j, T_k)} \right] \tag{2.53}$$

where

$$\left[\left(\left[B\right]^T\left[D\right]\left[B\right]\cdot\det\left[J\right]\right)\Big|_{(R_i,S_j,T_k)}\right] \tag{2.54}$$

indicates the value of $\left(\left[B\right]^T\left[D\right]\left[B\right]\det\left[J\right]\right)$ evaluated at $r=R_i$, $s=S_j$ and $t=T_k$, and $R_1=S_1=T_1=-0.57735$ and $R_2=S_2=T_2=+0.57735$.

2.12 Direct Integration of Equations of Motion

The direct integration of the equations of motion provides the response of the system at discrete intervals of time which are usually equally spaced. Determination of the response involves the computation of three basic parameters: displacement, velocity, and acceleration. The integration algorithms are based on appropriately selected expressions that relate the response parameters at a given interval of time to their values at one or more previous time points. In general, two independent expressions of this nature must be specified. The equation of motion written for the time interval under consideration provides the third expression necessary to determine the three unknown parameters.

Direct integration thus involves a marching along the time dimension. It is assumed that at the beginning of the integration, response parameter values have been specified or have been computed at one or more points preceding the time range of interest. These specified or computed values permit the marching scheme to be begun so that response can be computed at as many subsequent points as desired. The accuracy and stability of a scheme depend on the expressions selected for relating the response parameters at a time to their historic value, as well as on the magnitude of the time interval used in the computation.

In the following sections we present several methods used in numerical integration

of the equation of motion and discuss their relative accuracy as well as the conditions that must be met to guarantee stability of the solution. The following notations are used in the presentation: $h =$ time interval, $t_n = nh$, $u_n =$ =displacement at time nh, $\dot{u}_n =$ velocity at time nh, $\ddot{u}_n =$ acceleration at time nh, and $p_n =$ the applied forces at time nh.

2.12.1 Derivation of General Formulas

As mentioned in section 2.12, time integration methods are based on appropriately selected expressions relating the response parameters at a given interval of time to their values at one or more previous points. A general expression of this type can be written as

$$u_{n+1} = \sum_{l=n-k}^{n} A_l u_l + \sum_{l=n-k}^{n+1} B_l \dot{u}_l + \sum_{l=n-k}^{n+1} C_l \ddot{u}_l + R \tag{2.55}$$

where R is a remainder term representing the error in the expression, and A_l, B_l, and C_l are constants, some of which may equal zero.

Equation (2.55) relates the displacement, velocity, and acceleration at time point $n+1$, to their values at the previous points $n-k$, $n-k+1$, …, n. The equation has $m = 5+3k$ undetermined constants A, B, and C. By a suitable choice for the values of these constants, the equation can be made exact in the special case where u is a polynomial of order $m-1$. When the formula is exact, the remainder term R will equal zero. Now, if equation (2.55) is exact for a polynomial of order $(m-1)$, it will also be exact when u takes any one of the following values 1, t, t^2, …, t^{m-1}. Therefore, to evaluate the m constants, we can successively set u equal to each of these values in turn, and in each case make a substitution in equation (2.55). This procedure yields m simultaneous equations involving the set of m coefficients A_l, B_l, and C_l. A solution of these equations provides the

required values for the coefficients.

Now if $u = t^m$ is substituted into equation (2.55), R cannot be expected to equal zero automatically. We will designate the resulting value of R by E_m. It will be evident that the larger the number of terms in equation (2.55), the smaller will be the magnitude of truncation error R. Equation having many terms may, however, encounter spurious roots and instability, characteristics that we shall examine in some detail later. It may not, therefore, be desirable to use all m free constants to reduce the truncation error. An approach having practical usefulness is to employ equation (2.55) to represent exactly a polynomial of order $p-1$, p being an integer smaller than m. Then $(m-p)$ constants become available which can be assigned arbitrary values chosen so as to improve the stability or convergence characteristics of the resulting formula.

A formula that is exact for polynomials up to an order $m-1$ has a truncation error E_m when $u = t^m$. It is of interest to estimate the truncation error term when u is a polynomial of order higher than m, or in the more general case, when u is a function other than a polynomial. Standard textbooks on numerical analysis show that in most cases the truncation error term R is given by

$$R = \frac{E_m}{m!} u^{(m)}(\xi) \quad (n-k)h \le \xi \le (n+1)h \tag{2.56}$$

where $u^{(m)}$ is the value of the mth differential of u at $t = \xi$. Parameter ξ is, in general, not known, and it may not therefore be possible to obtain a precise value for R. Nevertheless, equation (2.56) can often be used to provide an upper bound on R. An estimate of the truncation error term may be helpful in choosing one formula over the other, although such error is not the only criterion in the choice of a formula.

The procedure described in the foregoing paragraph is a very general method of finding formulas. In fact, all formulas of type equation (2.55) that are used in structural dynamics for time integration can be derived using the procedure described. However, very often such formulas are obtained from physical considerations, such as, for example, an assumed variation in the acceleration $\ddot{u}$, or from the well-known finite difference approximations of the differentials. In the following sections, we develop, both from the underlying physical considerations, and by using the technique of this section, a number of more commonly used methods of numerical integration of the equation of motion. In each case we also derive the truncation error term.

2.12.2 Newmark's β Method

In 1959, Newmark devised a series of numerical integration formulas which are collectively known as Newmark's β methods. We derive Newmark's formulas by the general method of section 2.12.1. The velocity expression is of the form

$$\dot{u}_{n+1} = a_1\dot{u}_n + a_2\ddot{u}_n + a_3\ddot{u}_{n+1} \tag{2.57}$$

Equation (2.57) is automatically satisfied with $u = 1$, so that we still have three free constants, a_1, a_2, and a_3. We use two of them to make the formula exact for $u = t$ and t^2, leaving one of the constants slack. Substitution into equation (2.57) gives

$$\begin{aligned} u &= t \qquad 1 = a_1 \\ u &= t^2 \qquad 2h = 2a_2 + 2a_3 \end{aligned} \tag{2.58}$$

We now have two equations and three unknowns. We assign an arbitrary value to one of the unknowns and determine the other two from equation (2.58). Let us select $a_3 = \gamma h$, where γ is an arbitrary constant. We then get

$$\begin{aligned} a &= 1 \\ a_2 &= h(1-\gamma) \end{aligned} \tag{2.59}$$

Equation (2.57) now takes the form

$$\dot{u}_{n+1} = \dot{u}_n + h(1-\gamma)\ddot{u}_n + h\gamma\ddot{u}_{n+1} + R \tag{2.60}$$

There error term is obtained by substituting $u = t^3$ in equation (2.60), so that

$$\begin{aligned} 3h^3 &= 6h^2\gamma + E_3 \\ E_3 &= h^2(3-6\gamma) \end{aligned} \tag{2.61}$$

Using equation (2.56) and (2.57), we get

$$R = \frac{E_3}{3!}u^{(3)}(\xi) = h^2\left(\frac{1}{2} - \gamma\right)u^{(3)}(\xi) \tag{2.62}$$

Constant γ is usually selected to be 1/2. With this value for γ, equation (2.60) becomes

$$\dot{u}_{n+1} = \dot{u}_n + \frac{h}{2}\ddot{u}_n + \frac{h}{2}\ddot{u}_{n+1} + R \tag{2.63}$$

Further, the error term given by equation (2.62) becomes zero. This implies that the formula is exact for polynomials of order up to 3. The new error term is obtained by substituting $u = t^4$ and can be shown to be

$$R = -\frac{h^3}{12!}u^{(4)}(\xi) \tag{2.64}$$

The displacement expression in Newmark's β method is

$$u_{n+1} = b_1 u_n + b_2 \dot{u}_n + b_3 \ddot{u}_n + b_n \ddot{u}_{n+1} \tag{2.65}$$

Equation (2.65) has four free constants. We use three of them to make the formula exact for $u = 1$, t, and t^2. Substituting these values of u, in turn, in equation (2.65), we obtain

$$
\begin{aligned}
u &= 1 \qquad 1 = b_1 \\
u &= t \qquad h = b_2 \\
u &= t^2 \qquad h^2 = 2b_3 + 2b_4
\end{aligned}
\tag{2.66}
$$

Equation (2.66) provides three relationships among four unknowns. We assign an arbitrary value βh^2 to b_4 so that $b_3 = h^2(1/2 - \beta)$. Equation (2.65) now reduces to

$$
u_{n+1} = u_n + h\dot{u}_n + h^2(\frac{1}{2} - \beta)\ddot{u}_n + h^2\beta\ddot{u}_{n+1} + R \tag{2.67}
$$

The error term *R* is obtained by substituting $u = t^3$ in equation (2.67), which gives

$$
\begin{aligned}
h^3 &= 6\beta h^3 + E_3 \\
E_3 &= h^3(1 - 6\beta)
\end{aligned}
\tag{2.68}
$$

and

$$
R = \frac{E_3}{3!}u^{(3)}(\xi) = h^3\left(\frac{1}{6} - \beta\right)u^{(3)}(\xi) \tag{2.69}
$$

By assigning different values to γ and β, a series of integration formulas can be obtained. As an example, when $\gamma = 0$ and $\beta = 0$, Newmark's β method reduces to the constant-acceleration method, which we have already discussed. Other more commonly used versions of the Newmark's β method are: The average acceleration method, $\gamma = 1/2$, $\beta = 1/4$.

2.12.3 Average Acceleration Method

When γ is set equal to 1/2 and $\beta = 1/4$, equation (2.60) and (2.67) reduce to

$$
\dot{u}_{n+1} = \dot{u}_n + \frac{h}{2}(\ddot{u}_n + \ddot{u}_{n+1}) - \frac{h^3}{12}u^{(4)}(\xi) \tag{2.70}
$$

$$
u_{n+1} = u_n + h\dot{u}_n + \frac{h^2}{4}(\ddot{u}_n + \ddot{u}_{n+1}) + 0.152\,h^3u^{(3)}(\xi_m) \tag{2.71}
$$

The error term in equation (2.70) has been obtained from equation (2.64). For $\beta = 1/4$, the error expression of equation (2.69) is not applicable. The error term in equation (2.71), obtained by a somewhat more complicated procedure [109], represents an upper bound. The coordinate value ξ_m lies between 0 and h and is selected to give the maximum value of differential $u^{(3)}$. Equation (2.70) and (2.71) can also be derived by assuming that, as indicated in Fig. 2.11, the acceleration of the system remains constant over the small interval h and its value is equal to the average of the values of accelerations at the beginning and end of the interval:

$$\ddot{u} = \frac{1}{2}(\ddot{u}_n + \ddot{u}_{n+1}) \tag{2.72}$$

For simplicity, we shift the origin on the time axis to point t_n. Then by integrating equation (2.72) and applying the boundary conditions $\dot{u} = \dot{u}_n$ at $t = 0$ and $\dot{u} = \dot{u}_{n+1}$ at $t = h$, we get

$$\dot{u} = \dot{u}_n + \frac{t}{2}(\ddot{u}_n + \ddot{u}_{n+1}) \tag{2.73}$$

and

$$\dot{u}_{n+1} = \dot{u}_n + \frac{h}{2}(\ddot{u}_n + \ddot{u}_{n+1}) \tag{2.74}$$

Integration of equation (2.73) with the boundary conditions $u = u_n$ at $t = 0$ and $u = u_{n+1}$ at $t = h$ yields

$$u_{n+1} = u_n + \dot{u}_n h + \frac{h^2}{4}(\ddot{u}_n + \ddot{u}_{n+1}) \tag{2.75}$$

Equations (2.74) and (2.75) are, of course, the same as equation (2.70) and (2.71), respectively. The third relationship is obtained by writing the equation of motion at time

point $n+1$:

$$m\ddot{u}_{n+1} + c\dot{u}_{n+1} + k u_{n+1} = p_{n+1} \tag{2.76}$$

Equation (2.74) and (2.75) combined with equation (2.76) enable us to solve for u_{n+1}, $\dot{u}_{n+1}$, and $\ddot{u}_{n+1}$ in terms of u_n, $\dot{u}_n$, and $\ddot{u}_n$. From equation (2.75) we obtain

$$\ddot{u}_{n+1} = \frac{4}{h^2}(u_{n+1} - u_n - h\dot{u}_n) - \ddot{u}_n \tag{2.77}$$

Substitution of equation (2.77) into equation (2.74) gives

$$\dot{u}_{n+1} = -\dot{u}_n + \frac{2}{h}(u_{n+1} - u_n) \tag{2.78}$$

Finally, on substituting for $\ddot{u}_{n+1}$ and $\dot{u}_{n+1}$ from equation (2.77) and (2.78) in equation (2.76) and collecting terms, we get

$$\left(\frac{4m}{h^2} + \frac{2c}{h} + k\right)u_{n+1} = p_{n+1} + m\left(\frac{4}{h^2}u_n + \frac{4}{h}\dot{u}_n + \ddot{u}_n\right) + c\left(\frac{2}{h}u_n + \dot{u}_n\right) \tag{2.79}$$

Equation (2.79) can be solved for u_{n+1}. Substitution into equation (2.77) and (2.78) then gives $\ddot{u}_{n+1}$ and $\dot{u}_{n+1}$, respectively. To begin the integration, u_0, $\dot{u}_0$, and $\ddot{u}_0$ must be known. Two of these, usually the initial displacement and the initial velocity, will be given; the third can be determined by using the equation of motion written at $t = 0$. For an *N*-degree-of-freedom system, equation (2.77) to (2.78) can be rewrite as follows:

$$[\ddot{u}_{n+1}] = -[\ddot{u}_n] + \frac{4}{h^2}\{[u_{n+1}] - [u_n] - h[\dot{u}_n]\} \tag{2.80}$$

$$[\dot{u}_{n+1}] = -[\dot{u}_n] + \frac{2}{h}\{[u_{n+1}] - [u_n]\} \tag{2.81}$$

A third relationship is obtained from the equation of motion written at time point $n+1$:

$$[M][\ddot{u}_{n+1}] + [C][\dot{u}_{n+1}] + [K][u_{n+1}] = [p_{n+1}] \tag{2.82}$$

Substitution for $[\dot{u}_{n+1}]$ and $[\ddot{u}_{n+1}]$ from equation (2.80) and (2.81) in equation (2.82) gives

$$\left\{ \frac{4}{h^2}[M]+\frac{2}{h}[C]+[K] \right\}[u_{n+1}]= \\ [P_{n+1}]+[M]\left\{ \frac{4}{h^2}[u_n]+\frac{4}{h}[\dot{u}_n]+[\ddot{u}_n] \right\}+[C]\left\{ \frac{2}{h}[u_n]+[\dot{u}_n] \right\} \tag{2.83}$$

Equation (2.83) is solved for $[u_{n+1}]$ and the resulting value is substituted in equation (2.80) and (2.81), respectively, to obtain $[\ddot{u}_{n+1}]$ and $[\dot{u}_{n+1}]$. It will be noted that the solution for $[u_{n+1}]$ requires factorization of $[K]$. The average acceleration method is unconditionally stable and is therefore suitable for direct integration of the equations of motion of systems with a large number of degrees of freedom.

2.13 Parallel Substructure Method

Parallel substructure method has been one of the most popular approaches for parallel finite element computations. Based upon the direct method, parallel substructure method is suitable for not only linear but also nonlinear structural analysis for its robustness on ill-conditioned problems. In addition, substructure method is usually used for finite element analysis with adaptive method refinement or local nonlinearities, out-of-core finite element analysis, or cooperative design analyses among different teams. The method first partitions the structure into a number of non-overlapping substructures and assigns each substructure to a separate processor. Each processor then forms its substructure equilibrium equations:

$$[K]_k\{u\}_k=\begin{bmatrix} K_{II} & K_{IE} \\ K_{EI} & K_{EE} \end{bmatrix}_k \begin{Bmatrix} u_I \\ u_E \end{Bmatrix}_k = \begin{Bmatrix} f_I \\ f_E \end{Bmatrix}_k \tag{2.84}$$

in which $[K]$ is the stiffness matrix; $\{u\}$ is the displacement vector; $\{f\}$ is the external force vector; the subscript *k* denotes the k^{th} substructure; the subscripts *I* and *E* denote the internal and interface degrees-of-freedom, respectively. Then, static condensation of substructure interior degrees-of-freedom is performed independently and concurrently within each substructure without any inter-process communication as expressed by the following two equations:

$$[\overline{K}]_k = [K_{EE}]_k - [K_{EI}]_k [K_{II}]_k^{-1} [K_{IE}]_k \tag{2.85}$$

$$[\bar{f}_E]_k = [f_E]_k - [K_{EI}]_k [K_{II}]_k^{-1} [f_I]_k \tag{2.86}$$

The condensed system of each substructure is then assembled to form a set of global equations for the unknowns along the substructure interfaces and the solution of the global system of equations is performed as follows:

$$[\overline{K}_{EE}]_g = \sum_{k=1}^{N_P} \left([B]_k [\overline{K}_{EE}]_k [B]_k^T \right) \tag{2.87}$$

$$[\bar{f}_e]_g = \sum_{k=1}^{N_P} \left([B]_k [\bar{f}_E]_k \right) \tag{2.88}$$

$$[u_E]_g = [\overline{K}_{EE}]_g^{-1} [\bar{f}_E]_g \tag{2.89}$$

in which the subscript *g* denotes the global system; the matrix $[B]_k$ is the Boolean matrix for mapping the degrees-of-freedom from the substructure *k* to the global system. Finally, the internal degrees-of-freedom of each substructure are solved concurrently within each processor as follows:

$$[u_E]_k = [B]_k^T [u_E]_g \tag{2.90}$$

$$[u_I]_k = [K_{II}]_k^{-1} \left(\{f_I\}_k - [K_{IE}]_k \{u_E\}_k \right) \tag{2.91}$$

The scheme for the parallel substructure method implemented in our parallel source code for the finite element analyses is shown in Fig. 2.12. In addition, the modified decomposition algorithm developed by [118] is used for the static condensation of the substructure interior degrees-of-freedom.

Because the concepts of the substructure method for solving the equilibrium equations are very similar to the multi-frontal method for solving a linear system [117,119], the parallel finite element analysis using the substructure method can be seen as a type of multi-frontal method special for finite element analyses. One of the major differences between the substructure method and the multi-frontal method is that the former one uses element as the basic unit for mesh partitioning, while the latter one usually uses degree-of-freedom as the basic unit. The major advantage of using 'element' as the basic unit is that, theoretically, it requires less operation on mesh partitioning and load balancing because the number of elements is usually much fewer than the number of degree-of-freedom.

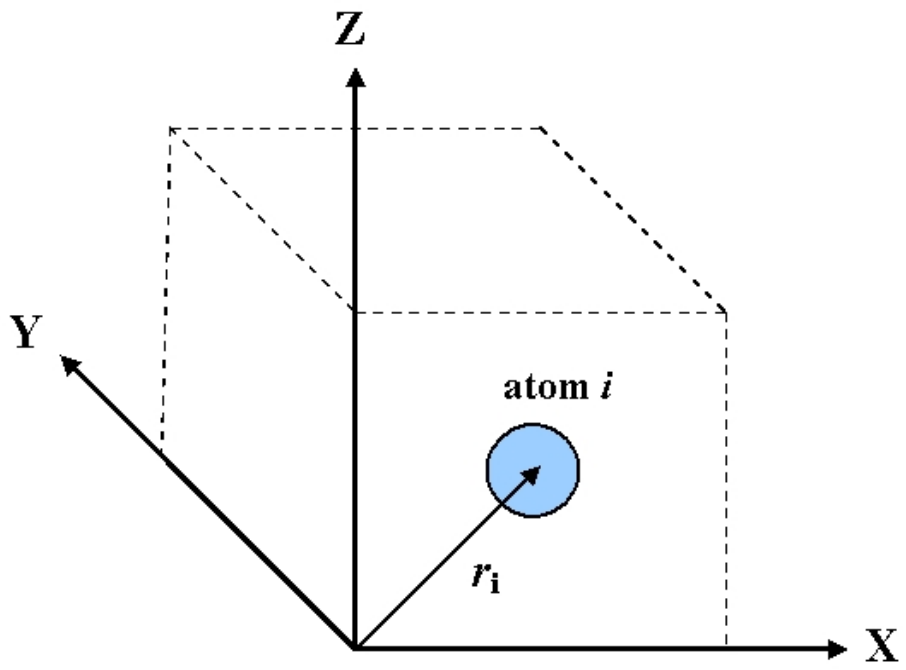

Fig. 2.1 Cartesian frame

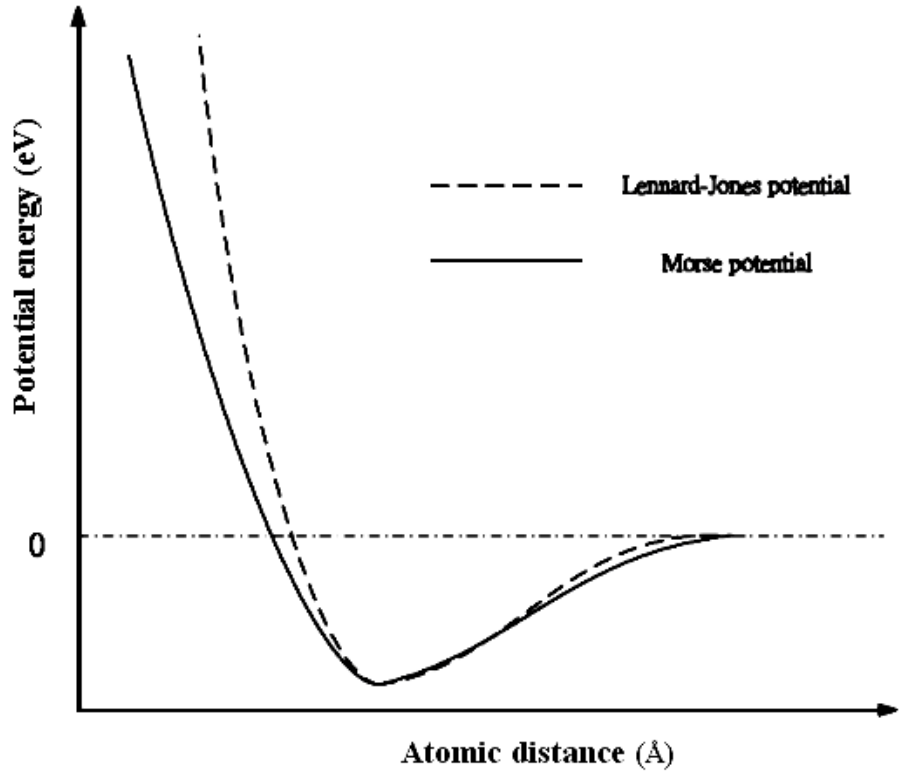

Fig. 2.2 Lennard-Jones pairwise intermolecular potential

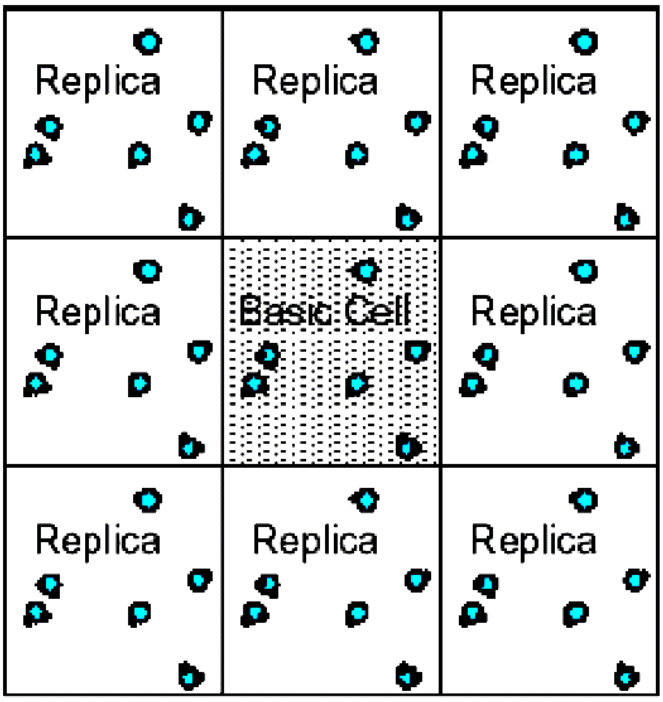

Fig. 2.3 Periodic boundary conditions

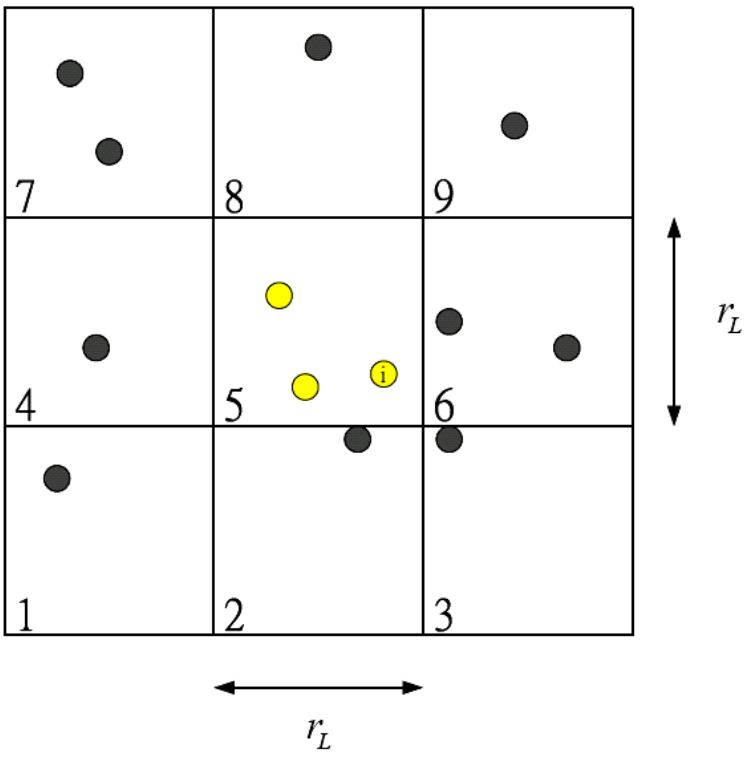

Fig. 2.4 Cell link list method

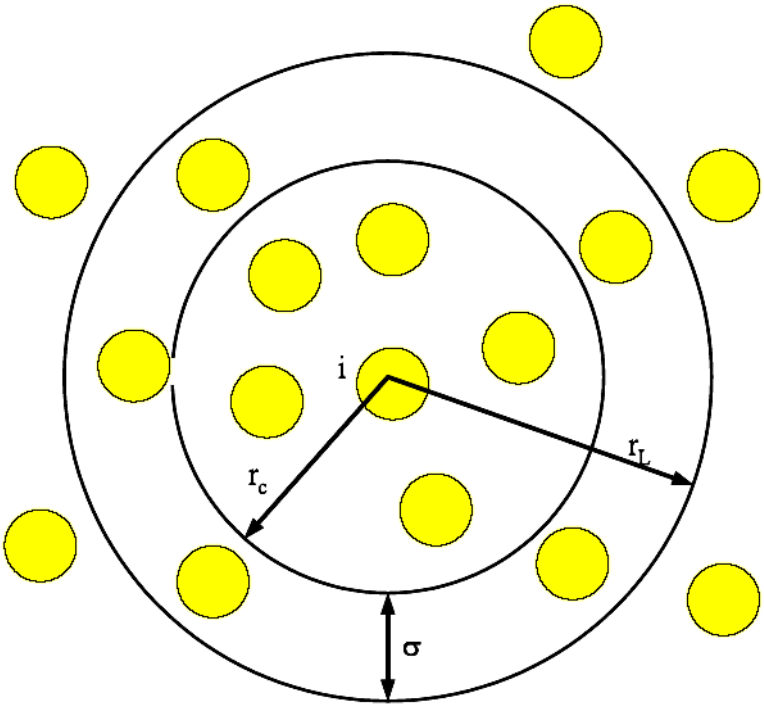

Fig. 2.5 Verlet list method

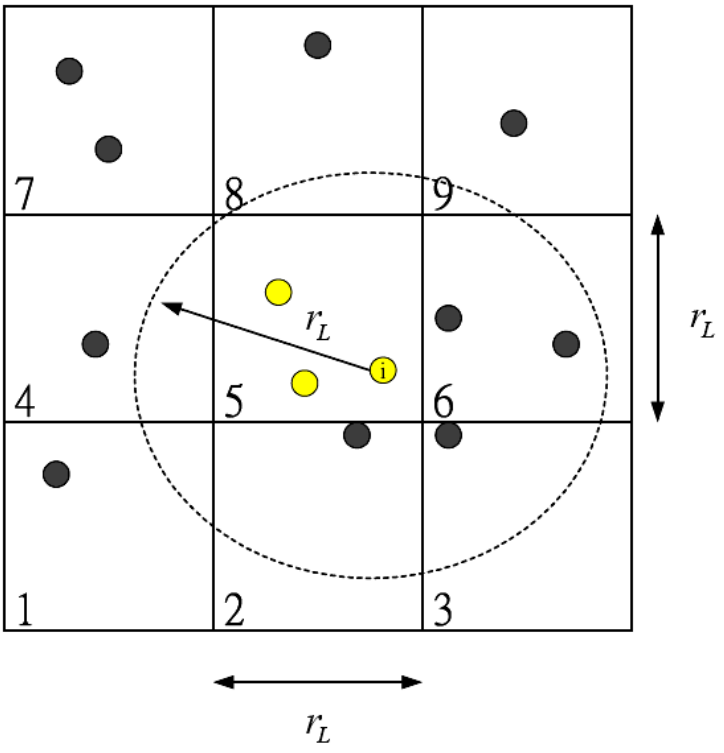

Fig. 2.6 Cell link list combined verlet list method

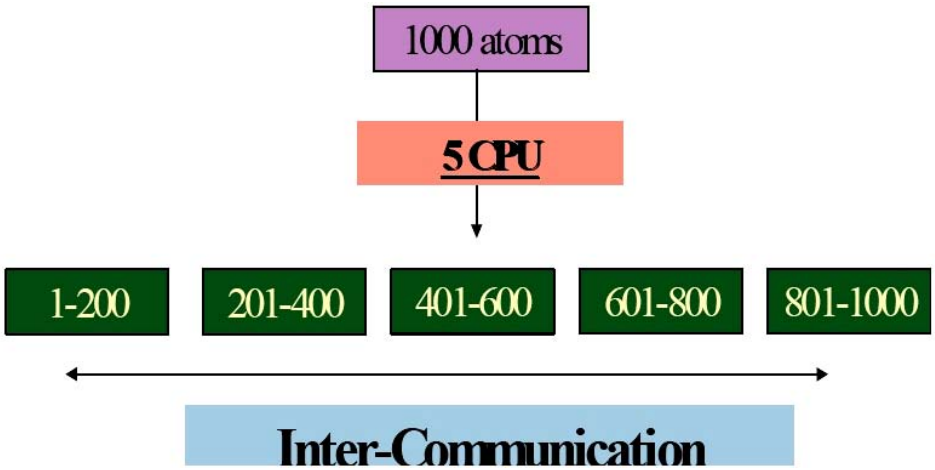

Fig. 2.7 A sketch of atomic decomposition algorithm

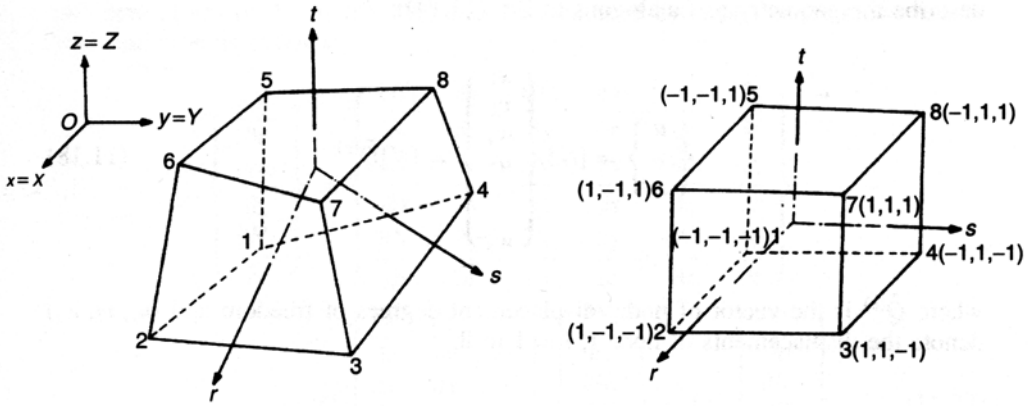

(a) In global *xyz* system **(b) In local *rst* system**

Fig. 2.8 A hexahedron element with 8 nodes

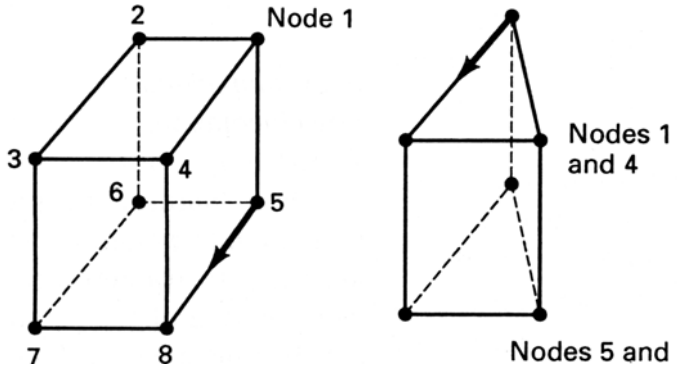

Fig. 2.9 A tetrahedral element by using collapsing hexahedron element

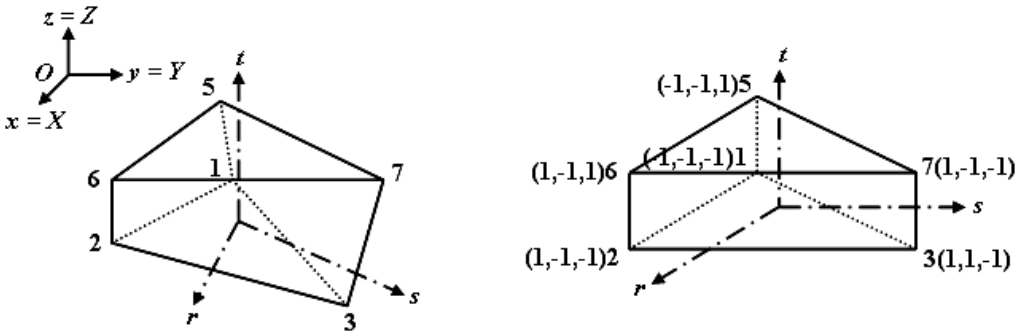

(a) In global *xyz* system **(b) In local *rst* system**

Fig. 2.10 A tetrahedral element with 6 nodes

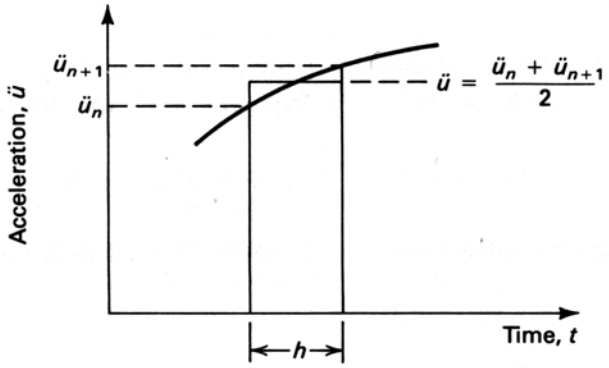

Fig. 2.11 Average acceleration method

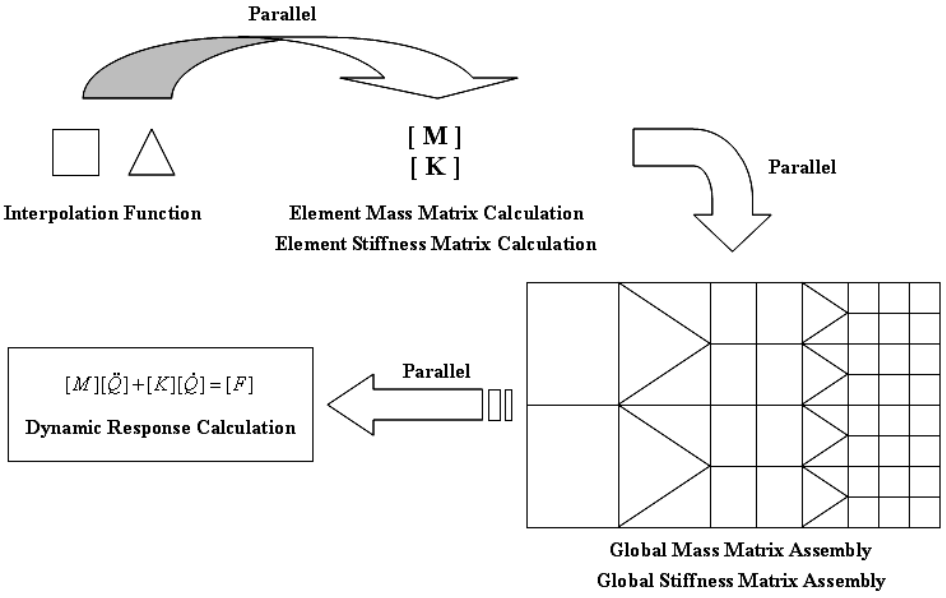

Fig. 2.12 A scheme for the parallel substructure method in FEM

Chapter 3 Nanoindentation for Simulation and Experiment

3.1 Simulation Set Up of Crystal Ni Metal Orientation Surfaces

The simulated models consist of (100), (110), and (111) crystallographic orientation surfaces and three mono-crystalline nickel substrates. The dimensional scales of the simulated models are approximately 125 Å×125 Å×155 Å. The simulated functions consist of the rigidity, thermostat, and Newtonian functions from the method utilized by Jeng et al [122]. The rigidity atoms at the fixed bottom layers of substrate are assumed to be unaffected by the tip during the indentation process. Therefore, they are fixed in their initial atomic positions so as to maintain the complete frame for the simulated model. Periodic boundary conditions are used in the transverse x and y directions, which represent the infinite boundary of the substrate. The sharp tip of the indenter has a conical shape with a diameter of 6 nm and height of 3 nm. To acquire the most efficient calculations, the tip atoms also are assumed to be the same as the rigidity atoms; however, the tip atoms' indentation velocity is given by the displacement-rate at each time step of the simulation for the force interaction between the tip and the substrates.

The motions of thermostat atoms are modified based on Nosé-Hoover thermostat [123], which sets up a heat bath that controls the temperature of Newtonian atoms to ensure the average temperature is at the desired value. The motions of all Newtonian atoms are determined by the interatomic forces derived by the interaction potential. The rigidity atoms of the nickel substrate are arranged as the fixed bottom layers, and the thermostat atoms are arranged on top of the fixed bottom layers. Meanwhile, the Newtonian atoms of the nickel substrate at the top region are bound by the thermostat atoms and are free to move by the influence of the tip atoms. The indenter tip is

positioned on the top of the substrate surface at the center, held at a constant distance from the substrate before the commencement of the indentation process. Because the three substrates are composed of more than 140,000 nickel atoms in each simulated model, we implement parallel computations by using the atom decomposition method [99]. The configurations of the simulated model are shown in Fig. 3.1.

In the present MD simulations, the interatomic force derived from the potential function is described by the tight-binding potential as follows:

$$\Phi_{total} = \sum_{i=1}^{N} \Phi_{ij} = \sum_{i=1}^{N} \left\{ -\left[\sum_{j} \xi^2 \exp\left(-2q \left(\frac{r_{ij}}{r_o} - 1 \right) \right) \right]^{1/2} + A \exp\left[-p \left(\frac{r_{ij}}{r_o} - 1 \right) \right] \right\} \tag{3.1}$$

where the subscripts i and j represent atom i and atom j, respectively, ξ is an effective hopping integral, r_{ij} is the distance between atoms i and j, and r_0 is the first-neighbors' distance. The total band energy is characterized by the second moment of the d-band density of state and is shown in the first part of the potential function. Meanwhile, the second part reveals a modified form of the original tight-binding potential. The free parameters of A, ξ, p and q are fitted to the experimental values of cohesive energy, lattice parameters (by the constraint on the atomic volume), and independent elastic constants for each pure system and for alloys. The interaction force F_i on atom i is derived from the equation (3.1), can be expressed as

$$F_i = -\sum_{j \neq i}^{N} \left(\frac{\partial \Phi_{ij}}{\partial r_{ij}} + \frac{\partial \Phi_{ij}}{\partial r_{ij}} \right) = m_i \frac{d^2 r_i(t)}{dt^2} \tag{3.2}$$

where m_i is the mass of atom i, r is the position of atom i, and N is the total number of atoms. By using equation (3.2), the resultant forces of each individual atom can be calculated at each time step. The parametric values of the tight-binding potential for the

present simulation models are adopted from Cleri et al [124].

MD simulations of nanoindentation comprise the equilibrium and indentation stages. In the equilibrium stage, the tip and the substrate surface are first positioned 10 Å apart in order to avoid the effect of attractive force which occurs as they gradually approach each other. The initial positions of tip and substrate atoms are prescribed in accordance with their crystalline structures, respectively. The initial velocities are assigned from a randomized producer, and are adjusted according to the rescaling method [123] in order to achieve a constant system temperature. After being held at the initial position for a period of time, both the tip and substrate are relaxed to their equilibrium configuration as a result of the interatomic forces acting on each individual atom. In the second indentation stage of MD simulations, the indentation is modeled by moving the tip 25 Å downward at a constant speed of 5 m/s, and then retracting the tip back to its original position at the same speed. In both stages, the time integration of motion is performed by applying the velocity-Verlet algorithm [123] to the corresponding data obtained in the previous step in order to derive the new position and velocity vectors of the substrate atoms. The system temperature of simulated models is kept at 300 K during the entire process. The size of the incremental time steps employed in the computations must be smaller than the thermal motion periods in the simulated system, but not so small as to be affected by the accumulations of inevitable round-off errors during the computational process. In the present computations, a compromised choice of time step $\Delta t = 1$ fs is thus employed.

It should be noted that nanoindentation experiments are performed at much slower rates than MD simulations (10^{-6} to 10^{-9} m/s); however, if conducted at these rates, MD

simulations would take extremely long processing times even with the fastest microprocessors [41]. Due to computing power limitations, the speeds of the indenter tip reported in the references are on an order of 1-100 m/s for most MD simulations of nanoindentation [125]. Although the indentation speed in our simulations is several orders of magnitude higher than typical experimental values, it is sufficiently slow to allow equilibrium of the indentation system, and allow any excess energy arising from the motion of the indenter to dissipate by means of Nosé-Hoover thermostat, which permits the indentation system to become a quasi-static state at each time step during nanoindentation [126]. Nevertheless, the sensitivity of the simulated results to the indentation velocity must be considered before the simulated and experimental results can be directly compared. A number of studies have attempted to do so. Liang et al [127] performed MD simulations to study dislocation nucleation in the initial stage during nanoindentation. With respect to the influence of indenter velocity on the dynamic effect of the material indentation behavior, they found that a higher indentation velocity in MD simulation leads to a higher strength, while the relationship between applied load and indentation depth shows little change. At the same time, the ensuing dislocation structures do not differ substantially. More importantly, the indentation curves for different velocities will quickly converge as the velocity decreases and approaches approximately 3 m/s. In fact, no obvious difference is apparent when the velocity is below 3 m/s. This discovery can be understood from the research of Yamakov et al [128], which uses MD simulations to investigate the dislocation processes in the deformation of nanocrystalline aluminum. They found that the typical dislocation-glide velocities of FCC nanocrystalline aluminum are about 500 m/s under strain rates of 10^7 s^{-1} in the [100]

direction, which are well below both the velocity of sound at about 3,664 m/s, and the experimental value of 3,050 m/s. Moreover, Fang et al [129] utilized MD simulation to analyze the indenter velocity effects on a single crystal copper substrate. One of the results for the effect of indenter velocity on material properties reveals that the critical velocity of the indenter necessary to cause an increase in Young's modulus and in hardness is about 80 m/s. The above-mentioned references suggest that the indenter velocity of 5 m/s adopted in our simulations is suitable to observe and describe the plastic deformation behavior and the material properties under nanoindentation.

3.2 Simulation Set Up of Multiscale Crystal Ni Metal

3.2.1 The Multiscale Model of Nanoindentation

In describing the present hybrid scheme, it is helpful to use the initial configuration of the hybrid simulation of nanoindentation. The simulated model of the indentation problem along with the arrangement in the present simulation is shown in Fig. 3.2. The simulated models consist of both a sharp rigidity tip of indenter and the nickel substrate. The sharp tip of the indenter has a conical shape with a diameter of 6 nm and height of 3 nm, and the dimensional scales of the nickel substrate are approximately 150 Å×150 Å × 200 Å. As shown in Fig. 3.2, the simulation system of nickel substrate is geometrically decomposed into three dynamic regions: the atomistic molecular dynamics region (MD); the finite element region (FE); and the MD/FE handshake region (HS). In Fig. 3.2(b), the blue is the rigidity atoms, the red are the composite atoms/nodes constituting the HS region between MD and FE, the yellow above the HS region are the MD atoms, and the yellow below the HS region are the FE nodes. The region close to the

indentation site is simulated with the atomistic MD resolution, representing the mono-crystalline nickel of (100) crystallographic orientation surface, while the remaining regions are simulated with the continuum FE resolution, representing the mesh grids of nickel material. The connection between the MD and FE regions is depend on the HS region, in which the FE mesh is refined down to the atomic scale in such a way that each FE node coincides with an MD atom. Continuum FE is used to efficiently describe large parts of the system that are elastically deformed but do not include highly strained or broken bonds. Closer to the indentation zone, as the strains become larger and the continuum description becomes less accurate, atomistic MD which requires a selected empirical many-body potential is adopted to provide a computationally fast atomic description. Note that not the entire regions of the multiscale model are shown in Fig. 3.2 since the extent of the present model is too large.

In the course of calculations at each time step, the MD calculations apply to the MD and the HS regions, whereas the FE calculations apply to the FE and the HS regions. A Hamiltonian is defined for the entire system. Its degrees of freedom are atomic positions r and their velocities $\dot{r}$ for the MD region, and displacements u and their time rates of change $\dot{u}$ for the FE region. Equations of motion for all the relevant variables in the system are obtained by taking the appropriate derivatives of this Hamiltonian. All variables can then be updated in lockstep as a function of time step using the same integrator. Thus, the entire time history of the system can be obtained numerically given an appropriate set of initial conditions. Following the uniform trajectory dictated by this Hamiltonian will result in a conserved total energy. In order to achieve a controlled comparison, two systems are prepared, subsequent to the above schedule. In one system,

the original multiscale system is kept, whereas in the other system we replace the portion of the substrate below the HS by a MD system, i.e., the entire nanoindentation model is described by a full MD simulations. Both systems are performed according to the same schedule described above. There are several details of the implementation specific to the nanoindentation simulations of nickel substrate that we describe below, as appropriate.

3.2.2 MD/FE-HS Region

To effectively combine the regions described by the MD and FE methods into a single model, one not only has to ensure consistency between the properties of the discrete and continuum media, but also to provide a smooth handshake between the two media. In the present work, the coupling of the two descriptions of the media is brought about by a HS region, in which the FE nodes coincide with the positions of the particles in the MD region, as shown in Fig. 3.3. Two-dimensional views of the HS region and its surroundings from MD and FE regions are represented as the multiscale model. Note that not all of the MD and FE regions are shown in Fig. 3.3 since their extent is too large. In Fig. 3.3, on the above side of the HS region is the atomistic region in which every atom is explicitly represented by the nickel crystalline lattices. On the below side of the HS region, there is a FE mesh with its associated nodes. Within the HS region, the MD crystalline lattices and the FE mesh grids are overlapped, yielding a one-to-one correspondence between MD atoms and FE nodes although not all atom sites are nodal positions. Moving away from the HS region on the continuum side, the FE nodes become increasingly sparse and the corresponding elements become larger so as to always completely fill the physical space. The particles belong to the MD part that are governed by the interaction via the interatomic potential, yet are governed by the continuum linear

elasticity theory if the particles belong to the FE part.

For these hybrid atom/node particles, the weighted function of an average Hamiltonian proposed by Lidorikis et al. [69,84] is utilized in the present simulations. Formally, a total hybrid Hamiltonian can be written as follows:

$$H_{total} = \frac{1}{2}\sum_{i}^{N} m_i v_i^2 + \frac{1}{2}\sum_{i,j}^{N_{atoms}} w_{ij}\Phi_{ij}(r_{ij}) + \frac{1}{2}\sum_{i}^{N_e}\sum_{i,j}^{N_{ne}} w_l u_i^l k_{ij}^l u_i^l \tag{3.3}$$

where N , N_e , and N_{ne} are the number of total particles, elements, and nodes per element, respectively. m_i corresponds to both atomic and nodal masses, Φ_{ij} is the many-body potential terms used in MD, and $\boldsymbol{u}^l$, $\boldsymbol{k}^k$ are the FE displacement vector and stiffness matrix, respectively, for element l. The tight-binding potential for nickel involves only short range interactions; therefore, two bi-layers of Ni (100) depicted as $L1$ and $L2$ in Fig. 3.3 are sufficient to make up the HS region. In the present multiscale model, the following weights in the hybrid scheme to be the most accuracy as compared with the full MD simulations are as follows:

$$w_{ij} = \begin{cases} 1 & ,if\ \ i\ \ or\ \ j\ \ is\ \ above\ \ L_1 \\ 4/7 & ,if\ \ i\ \ and\ \ j\ \ are\ \ within\ \ L_1 \\ 1/2 & ,if\ \ i\ \ or\ \ j\ \ crosses\ \ HS\ , \\ 3/7 & ,if\ \ i\ \ and\ \ j\ \ are\ \ within\ \ L_2 \\ 0 & ,if\ \ i\ \ or\ \ j\ \ is\ \ below\ \ L_2 \end{cases} \tag{3.4}$$

$$w_l = \begin{cases} 0 & ,if\ \ l\ \ is\ \ above\ \ HS \\ 1/2 & ,if\ \ l\ \ is\ \ crosses\ \ HS \\ 1 & ,if\ \ l\ \ is\ \ below\ \ HS \end{cases}$$

By the use of equation (3.3) and (3.4), it can be successful to merge seamlessly between MD and FE in the multiscale model since it exhibits the numerical stability during the computational process.

3.2.3 Molecular Dynamics

In the MD part of our multiscale model, the motions of all Newtonian atoms are determined by the interatomic forces derived by the interaction potential. For the dynamic responses of MD, the time integration of atomic motion is performed by applying the velocity-Verlet algorithm [123] to the corresponding data obtained in the previous step in order to derive the new position and velocity vectors of the substrate atoms. The atomic thermostat are modified based on Nosé-Hoover thermostat [122], which sets up a heat bath that controls the temperature of Newtonian atoms to ensure an average temperature maintained at the desired value. The atoms of the nickel substrate are arranged by the nickel crystalline lattices in the MD and HS regions in order to move by the influence of the tip atoms. The initial velocities are assigned from a randomized producer, and are adjusted according to the rescaling method [123] in order to achieve a constant system temperature. Periodic boundary conditions are used in the transverse x and y directions, which represent the infinite boundary of the substrate. The indenter tip is positioned on the top of the substrate surface at the center, held at a constant distance from the substrate before the commencement of the indentation process. Because the substrate of MD part is composed of more than 140,000 nickel atoms in the simulated model, we implement parallel computations by using the atom decomposition method [99]. In the present multiscale simulations of MD part, the potential function and the interatomic force is described by the same as equation (3.1) and (3.2).

3.2.4 Finite Element Method

In the FE part of our multiscale model, the continuum elastic energy is integrated over the entire volume of the sample by placing a mesh over the system. Therefore, the

distortions from equilibrium are relatively small and linear elasticity is sufficient to describe them. In this region, the equations of linear continuum elasticity are solved on a computational grid. The interpolation function can be used within each element of the mesh nodes to determine the displacement field everywhere. The kinetic energy integral is handled similarly. For the dynamic responses of FE, the time integration of nodal motion is performed by applying the average acceleration method [130] to the corresponding data obtained in the previous step in order to derive the new position and velocity vectors of the substrate nodes.

For the consideration of the computational cost, it is necessary to estimate whether the multiscale model will influence the simulated results of nanoindentation for the adoption of two-dimensional (2D) or three-dimensional (3D) models of FE. From the literature survey for the multiscale research, we found that there are several researches to adopt the 2D plane strain model of FE to couple MD in their mutiscale model of nanoindentation simulations, which include that Picu [64] utilized the quasicontinuum method to perform the nanoindentation simulations in the prototype BCC transition metal molybdenum (Mo) for the minimization of unwanted effects induced by the limited size of the specimen, Shenoy et al. [65] performed the plane strain nanoindentation using atomistic simulations as well as analytic models to determine a nucleation criterion for dislocation nucleation as compared with the results of the atomistic lattice statics by using the quasicontinuum method, and Smith et al. [67] applied the local quasicontinuum method, extended to handle the complex crystal structures, to silicon nanoindentation.

In the above-mentioned references, the results obtained from the multiscale model of nanoindentation all have a good agreement with the variation tendency of

nanoindentation. Furtherly, in the reference [67], Smith et al. also used both the 2D and 3D FE meshes to couple MD in their multiscale models. The compared results obtained from the nanoindentation simulations between these two models indicate that there are no obvious differences under the avoidance of the substrate effect, i.e., the specific value of the indentation depth divided by the substrate thickness can not be exceeded 10% (0.1) [131]. Accordingly, we can know that it is suitable to adopt the 2D FE model to couple MD in our multiscale simulations under the avoidance of the substrate effect in order to obtain the maximum computation cost for the length scale expansion. Therefore, in our multiscale model of FE part, the nodes not constrained by boundary conditions or stuck to the indenter are free to move in the *xz* plane, but are not permitted to move in the *y* direction, i.e., plane strain conditions of FE.

For this study, we use the quadrilateral elements of four nodes and the triangular elements of three nodes for grid coarsening with linear interpolation for the displacement field. Fixed boundary conditions are imposed on the bottom of the mesh, and periodic boundary conditions are imposed on the sides, perpendicularly to the indentation surface. For the constitutive relations, we use the elastic constants of nickel as determined from the tight-binding potential. We also use the lumped mass approximation, i.e., the mass is collapsed on the nodes instead of being uniformly distributed. This approximation has been shown to be more appropriate for small atomic-size elements [55,77]. In order to cooperate with the application of parallel algorithm in MD part, there are more than 15,000 mesh nodes in FE part also implemented by using the parallel computation of the parallel substructure method [118].

In the present simulations, the total elastic energy of a solid, for the undamped

system and in the absence of both tractions and body forces, is then given

$$L_{total} = \sum_{e=1}^{E} \left(T^{(e)} - \pi_p^{(e)} \right)$$
$$= \frac{1}{2} \sum_{e=1}^{E} \left[\dot{\vec{Q}}^T \left(\iint_{S^{(e)}} \rho [N]^T [N] dS \right) \dot{\vec{Q}} - \vec{Q}^T \left(\iint_{S^{(e)}} [B]^T [D][B] dS \right) \vec{Q} + \vec{Q}^T \vec{P}_c(t) \right] \tag{3.5}$$

where $T^{(e)}$, $\pi_p^{(e)}$, and $S^{(e)}$ are the kinetic energy, the potential energy, and the surface of an element *e*, respectively; $[N]$, $[D]$ and $[B]$ are the matrix of interpolation function, material properties, and partial differentiation, respectively; $\dot{\vec{Q}}$ and $\vec{Q}$ are the nodal velocity and displacement, ρ is the density value, and $\vec{P}_c(t)$ is the vector of concentrated nodal forces of the structure. By using the Lagrange equations [105], we can derive the dynamic equations of motion of a structure for the undamped system, as follows:

$$\sum_{e=1}^{E} \left[\left(\iint_{S^{(e)}} \rho [N]^T [N] dS \right) \ddot{\vec{Q}}(t) + \left(\iint_{S^{(e)}} [B]^T [D][B] dS \right) \vec{Q}(t) \right] =$$
$$\sum_{e=1}^{E} \left(\left[M^{(e)} \right] \ddot{\vec{Q}}(t) + \left[K^{(e)} \right] \vec{Q}(t) \right) = \sum_{e=1}^{E} \left[\vec{P}_c(t) \right] \tag{3.6}$$

where $\left[M^{(e)} \right]$ and $\left[K^{(e)} \right]$ are the mass and stiffness matrices of an element *e*, and $\ddot{\vec{Q}}$ is the nodal acceleration. Solve the equation of motion by applying the boundary and initial conditions. Equation (3.6) can be solved by using the techniques of a set of simultaneous linear differential equations for propagation problems.

3.2.5 Nanoindentation Simulation

The multiscale simulations of nanoindentation comprise the equilibrium and indentation stages. In the equilibrium stage, the tip and the substrate surface are first

positioned 10 Å apart in order to avoid the effect of attractive force which occurs as they gradually approach each other. After being held at the initial position for a period of time, both the tip and substrate are relaxed to their equilibrium configuration as a result of the interatomic forces acting on each individual atom. In the indentation stage, the indentation is modeled by moving the tip 25 Å downward at a constant speed of 5 m/s, and then retracting the tip back to its original position at the same speed. To acquire the most efficient calculations, the tip atoms also are assumed to be the same as the rigidity atoms; however, the tip atoms' indentation velocity is given by the displacement-rate at each time step of the simulation for the force interaction between the tip and the substrates. The system temperature of simulated models is kept at 300 K during the entire process. The size of the incremental time steps employed in the computations must be smaller than the thermal motion periods in the simulated system, but not so small as to be affected by the accumulations of inevitable round-off errors during the computational process. In the present computations, a compromised choice of time step $\Delta t = 1$ fs is thus employed. For the explanations of the high indentation speed used in our multiscale simulations of MD part as compared with the experimental conditions, we had elucidated the suitable factors as the above-mentioned descriptions in the section 3.1.

3.3 Experiment Set Up of Crystal GaN Metal Semiconductor

The GaN thin films (As shown in Fig. 3.5) used in this study were grown on (0001)-sapphire substrates by the metal-organic chemical-vapour deposition (MOCVD) method with an average thickness of about 2 μm. The detailed growth procedures of the GaN thin films can be found elsewhere [132]. The nanoindentation measurements were performed on a Nanoindenter MTS NanoXP® system (MTS Cooperation, Nano

Instruments Innovation Center, TN, USA, as shown in Fig. 3.6) with a diamond pyramid-shaped Berkovich-type indenter tip, whose radius of curvature is 50 nm. The mechanical properties (the hardness and Young's modulus) of GaN thin films were measured by nanoindentation with a continuous stiffness measurements (CSM) technique [133]. In this technique, a small sinusoidal load with known frequency and amplitude was superimposed onto the quasi-static load. It results in a modulation of the indenter displacement that is phase shifted in response to the excitation force. The stiffness, *S*, of the material, and the damping, ωC, along indentation loading can be respectively calculated using equations (3.7) and (3.8) expressed below. The hardness and elastic modulus are, then, calculated by putting the obtained stiffness data into equations (3.9) and (3.10), respectively. In this way, the hardness and modulus as a function of penetration depth are determined for a single loading-unloading cycle [134].

$$S = \left[\frac{1}{\left(P_{\max} / h(\omega)\right)\cos\Phi - \left(K_S - m w^2\right)} - K_f^{-1} \right] \tag{3.7}$$

$$S = \omega C = \frac{P_0}{h(\omega)} \sin\Phi \tag{3.8}$$

$$H = \frac{P_{\max}}{A_c} \tag{3.9}$$

$$\frac{E}{1-\upsilon^2} = \frac{\sqrt{\pi}}{2} \frac{P_0}{\sqrt{A_c}} \tag{3.10}$$

where $P_{\max}$ and $h(\omega)$ are denoted as the driving force and the displacement response of the indenter, respectively; Φ is the phase angle between $P_{\max}$ and $h(\omega)$; m is the mass of the indenter column; K_S is the is spring constant in the vertical direction; K_f

is frame stiffness; m, K_S and K_f are all constant values for the specified indentation system; ω is angular speed which equals $2\pi f$; f is the driven frequency of the ac signal of 45 Hz for this work, which is used to avoid the sensitivity to thermal drift; the load resolution of the system was 50 nN; v is Poission's ratio and set to be 0.25 [132] for current analysis; and A_c is the contact area when the material in contact with indenter being loaded at $P_{\max}$.

The area function, which is used to calculate contact area, *A*c, from contact depth, h_c, was carefully calibrated by using fused silica as the standard sample prior to the nanoindentation experiments. The nanoindentation tests were carried out in the following sequence: first of all, the Berkovich indenter was brought into contact with the surface at a constant strain rate of $0.05\ s^{-1}$ until 100 nm of penetration was achieved. The load was then held at the maximum value for 30 s in order to determine the creep behaviour. The Berkovich indenter was then withdrawn from the surface at the same rate until 10% of the maximum load was reached. This constant strain rate was chosen such that the strain-hardening effect could be avoided during the measurements. At least 10 indents were performed on each GaN film. The nanoindentations were sufficiently spaced to prevent mutual interactions. The hardness and Young's modulus of GaN films obtained from the present nanoindentation tests with CSM technique are 19.31 ± 1.05 GPa and 286.12 ± 25.34 GPa, respectively. As displayed in Table 4-1, which summarizes the hardness and Young's modulus for various GaN samples obtained from different indentation methods [135-138], the values obtained by using Berkovich indenter are somewhat larger than those obtained by other methods. Nonetheless, the current data are consistent with our previous studies [132], indicating the reproducibility of the technique.

Furthermore, in order to reveal the role played by the nucleation and propagation of dislocations in indentation-induced deformation, cyclic nanoindentation tests were also performed in this study. These tests were carried out by the following sequences. First, the indenter was loaded to some chosen load and then unloaded by 90% of the previous load, which completed the first cycle. It then was reloaded to a larger chosen load and unloaded by 90% for the second cycle. Fig. 3.9 illustrated a typical cyclic indentation test repeated for 5 cycles. It is noted that in each cycle, the indenter was held for 30 s at 10% of its previous maximum load for thermal drift correction and for assuring that complete unloading was achieved. The thermal drift was kept below ± 0.05 nm s^{-1} for all indentations considered in this study. The same loading– unloading rate of 10 mN s^{-1} was used.

After indentation to a maximum load of 200 mN, the cross-sectional transmission electron microscopy (TEM, as shown in Fig. 3.7) samples of the GaN films were prepared by the lift-out technique using a dual-beam FIB station (FEI Nova 220, as shown in Fig. 3.8). The technique for sample preparation using the FIB consisted of first milling two crosses alongside the indented area, serving as makers, and then depositing a layer of Pt (about 1 μm thick) to protect the area of interest from damages and implantation by the injected Ga^{+} ion beam. Material was removed from both sides of the selected area using an ion current of 5 nA, followed by successive thinning steps by reducing the ion current progressively from 3 nA to 300 pA until the foil was about 1 μm thick. Subsequently, the bottom and one side of the foil were cut free while tilting the sample at an angle of 45° to the ion beam. A central area containing the indentation apex of a few micrometres in length was then chosen and thinned further to a thickness of 100

nm, leaving the side thicker areas relatively intact to prevent the foil from collapsing. Finally a small area of interest was selected and thinned until electron transparency was achieved. The FIB milling procedures are displayed in Fig. 3.10. The transfer of the sample from the sample holder to the TEM grid with a carbon membrane was made *ex situ* using the electrostatic force of a glass needle. The TEM samples were examined in JEOL-2010F TEM operating at an accelerating voltage of 200 kV.

Table 3-1 Mechanical properties of GaN thin films derived from various measurement methods

	GaN thin films	*H* (GPa)	*E* (GPa)	Indenter tip
Drovy *et al* [135]	As-grown	12± 2	287	Vickers
Nowak *et al* [136]	As-grown	20	295	Spherical
Kucheyev *et al* [137]	As-grown	13.4	233	Spherical
	Ion-damaged	15.1	164	
	Ion-damaged	15.1	164	
	Amorphized	2.4	65	
Jian *et al* [132]	As-grown	19.34± 2.13	314.93± 40.58	Berkovich
	Si-doped	20.12± 2.51	247.16± 14.89	
Kavouras *et al* [138]	As-grown	13.67± 0.15	—	Knoop
	O-doped	14.74± 0.22	—	
	Mg-doped	16.87± 0.13	—	
	Au-doped	12.16± 0.09	—	
	Xe-doped	11.35± 0.12	—	
	Ar-doped	9.98± 0.14	—	
Chien *et al* [a]	As-grown	19.31± 1.05	286.12± 25.34	Berkovich

[a] This study

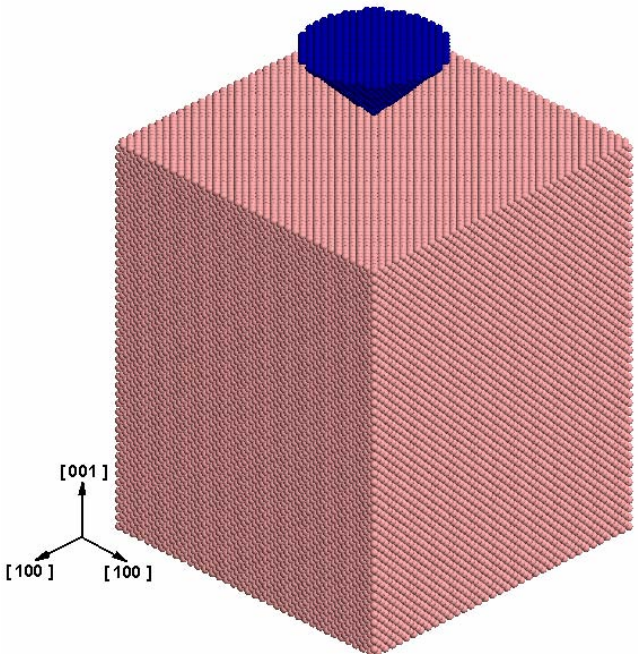

(a)

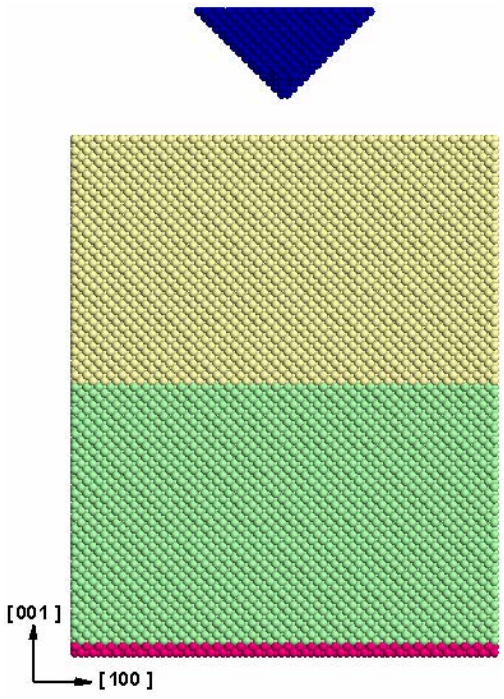

(b)

Fig. 3.1 Simulated nickel models of both the material and functional configurations.

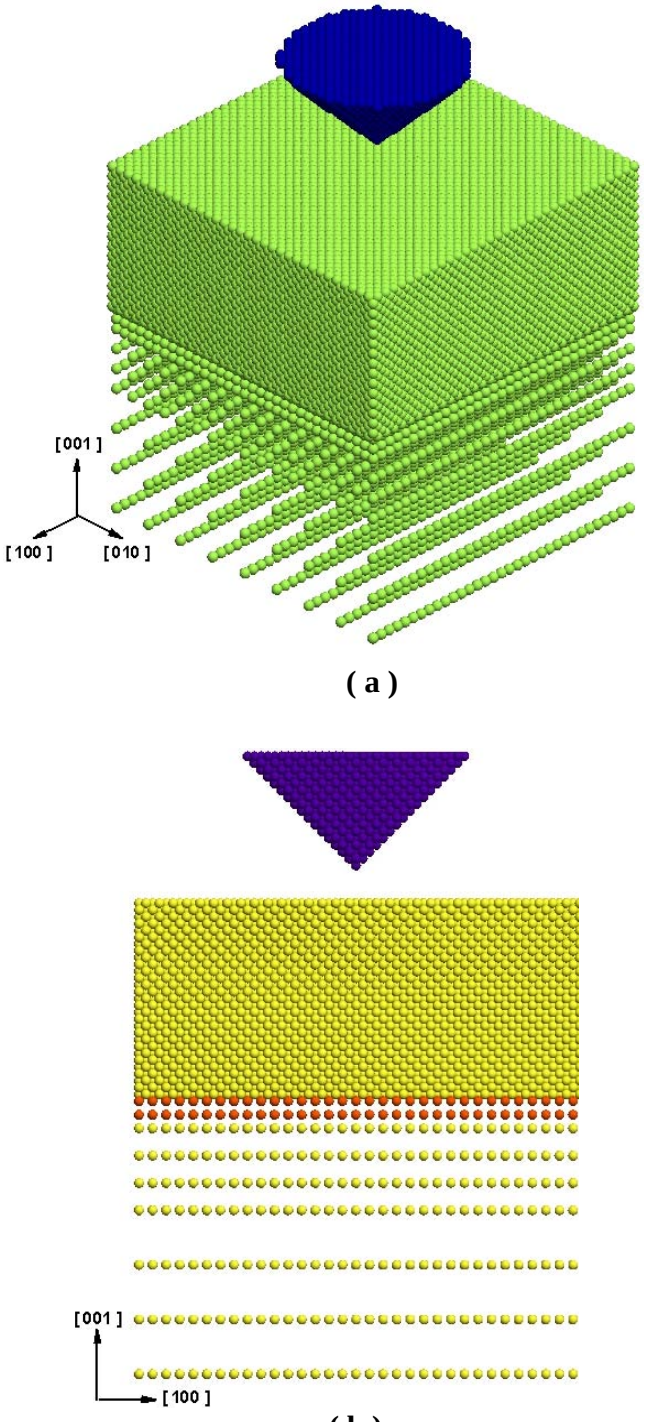

Fig. 3.2 Multiscale Simulation models of nickel substrate of both the material and functional configurations.

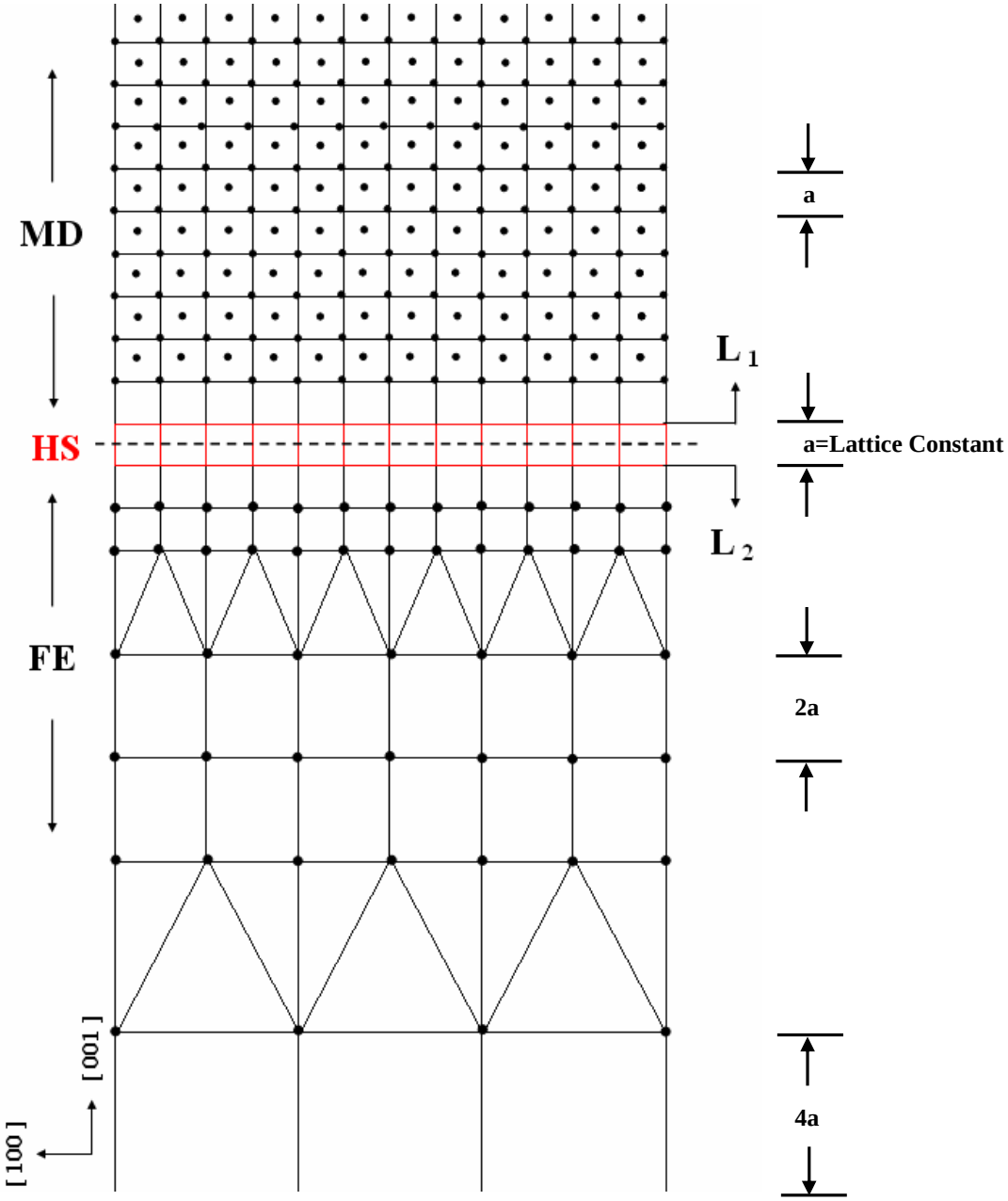

Fig. 3.3 Close-up of the HS region and its surroundings in the nickel substrate showing 2D views from two different directions.

(a)

(b)

Fig. 3.4 The high performance computer (HPC).

Fig. 3.5 The experimental samples of GaN thin films.

(a)

(b)

Fig. 3.6 Nanoindenter (MTS NanoXP® Nanoindenter).

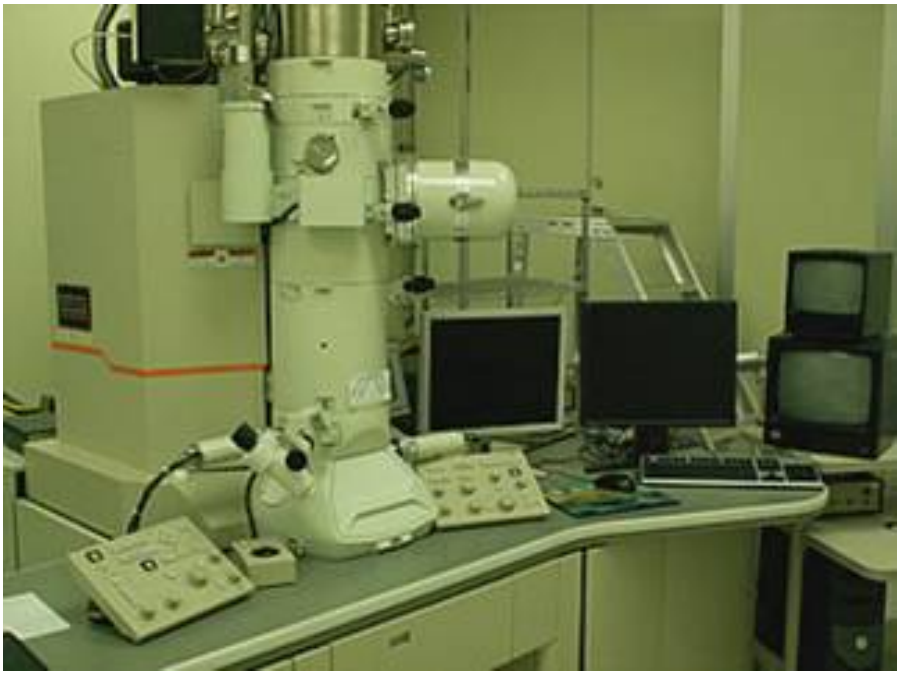

Fig. 3.7 The transmission electron microscopy (Jeol JEM-2100F TEM).

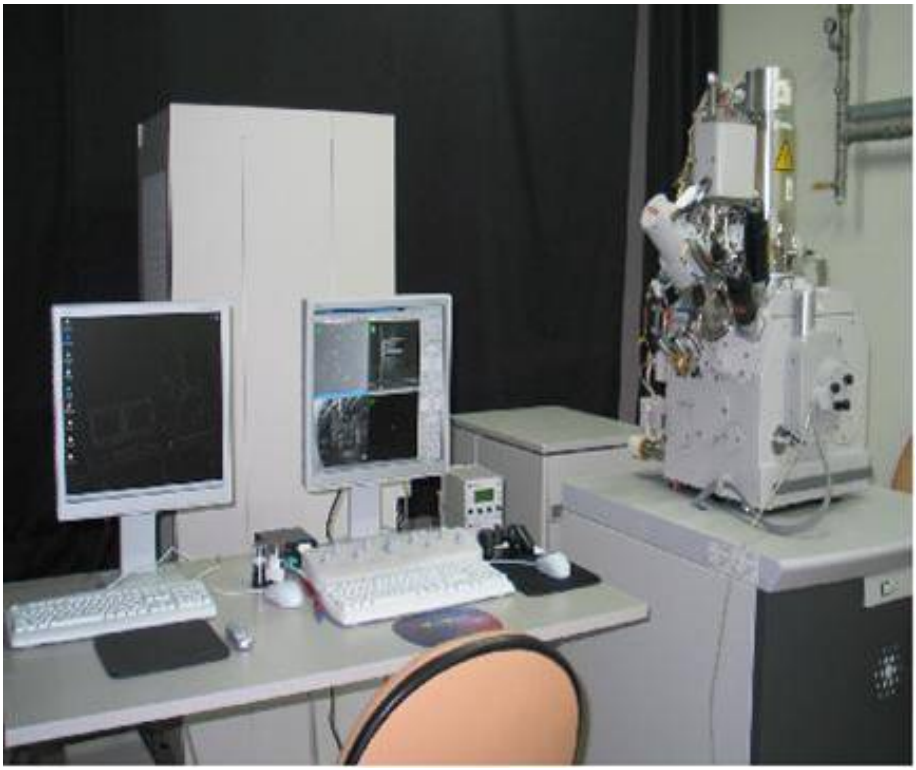

Fig. 3.8 Focused ion beam (FEI Nova 220 FIB).

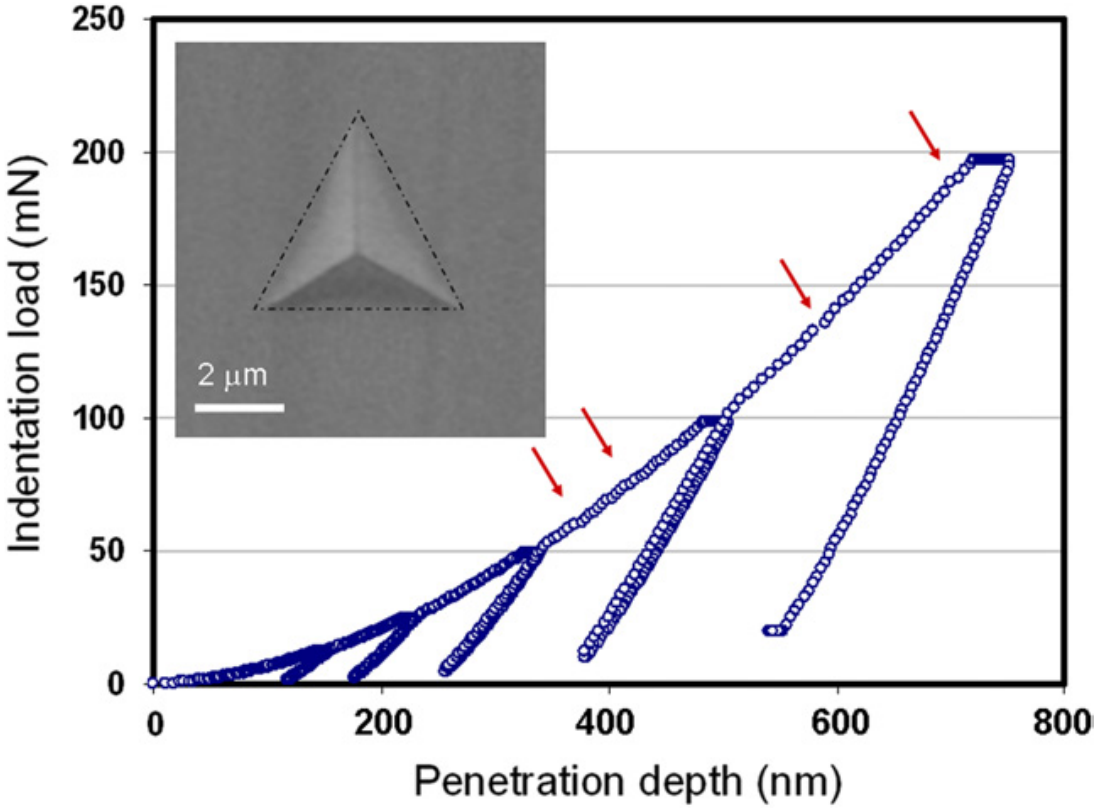

Fig. 3.9 Typical cyclic nanoindentation load–displacement curves for GaN thin films obtained with a Berkovich indenter.

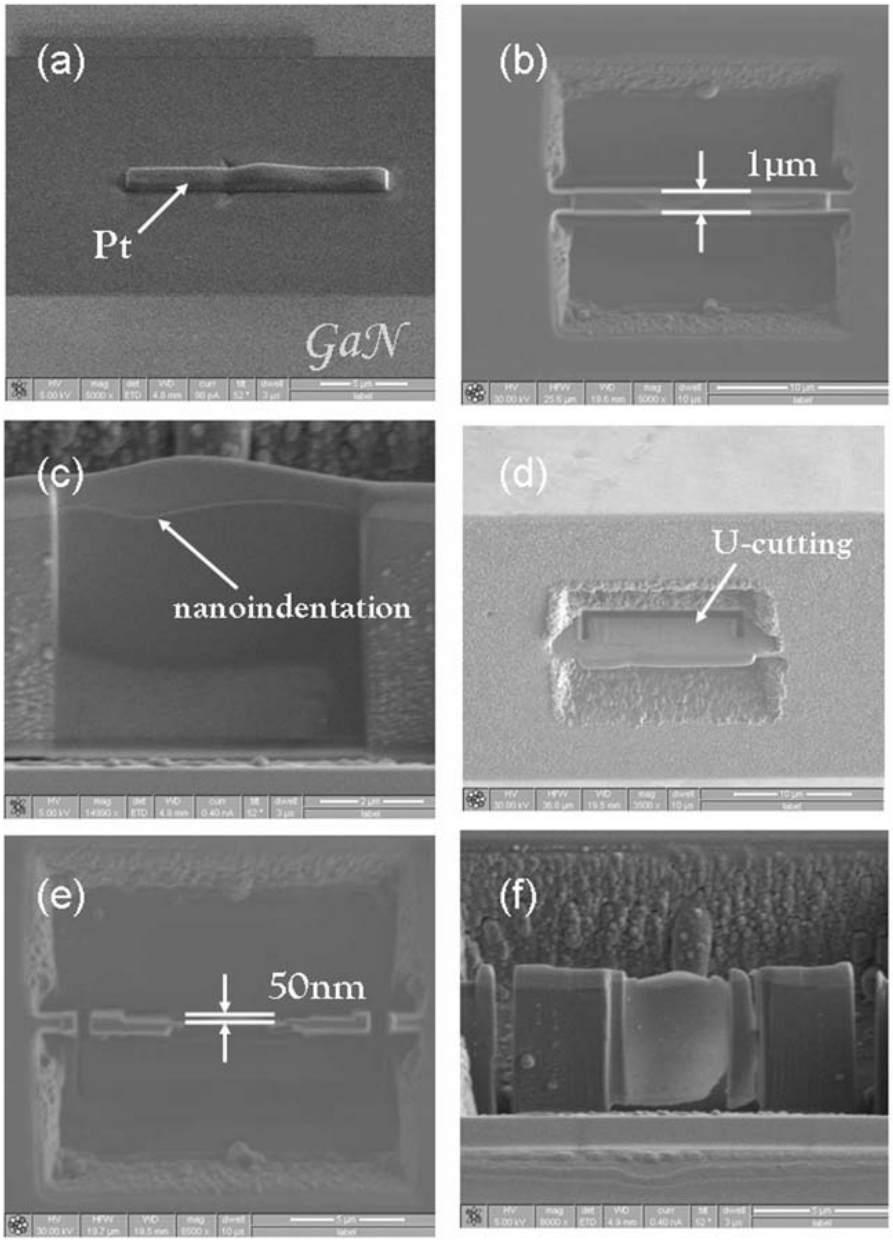

Fig. 3.10 Illustration of the typical procedures for FIB milling sample preparation. Sample preparation starts with a line of nanoindentations.

Chapter 4 Results and Discussions

4.1 The Nanoindentation Characteristics of Crystal Ni Metal Orientation Surfaces

4.1.1 Plastic Deformation Characteristic during Nanoindentation

The indentation curves of the tip force and the indentation depth for three nickel substrates with different crystallographic surfaces of (100), (110), and (111) orientations are shown in Fig. 4.1(a)-(c). The vertical axis represents the value of the tip force, defined as the resultant force at the indenting direction exerted upon the tip by nickel atoms, and the horizontal axis represents the indentation depth. The height of the tip is set to zero indentation depth when the atoms of the tip start interacting with the nickel atoms of the substrate. The positive and negative values of the tip force represent the repulsive and attractive force between the tip and the nickel substrate, respectively. For each crystallographic surface, because the interaction between two atoms is attractive as they gradually approach each other, the tip force is negative in the beginning of the indenting. As the tip increases its indentation depth into the surface, attractive force will convert into repulsive force.

In Fig. 4.1, it is clearly evident that in the course of the indenting process, the value of the tip force imposed on the nickel (100) substrate varies more significantly, while the values of tip forces exerted on nickel (110) and (111) substrates appear to monotonically increase with the indentation depth. For convenience in describing the variations of tip force with the indentation depth in Fig. 4.1, labels (1) to (18) are used to explain the characteristic variations of the indentation curves. Each label marks the characteristic indentation depth at which the tip force displays relatively obvious variation. The

corresponding morphologies, as well as the distributions of atomic normal stress on indentation direction at these labels are shown in Fig. 4.2 to Fig. 4.4. Because the coordination number of a nickel atom in a perfect FCC crystalline material is 12, nickel atoms with a coordination number lower than 12 under indentation are shown during the evolution of the deformation and relaxation of the substrates [139]. In addition, atomic-level stress is also used to monitor the evolution of the structure relaxation in Fig. 4.2 to Fig. 4.4. The atomic stress is obtained from the following formula [140]:

$$\sigma_{mn} = \frac{1}{N_R}\sum_i \left[\frac{m_i v_i^m v_i^n}{V_i} - \frac{1}{2V_i}\sum_j \frac{\partial \phi(r_{ij})}{\partial r_{ij}} \frac{r_{ij}^m r_{ij}^n}{r_{ij}} \right] \tag{4.1}$$

where m_i is the mass of atom *i*; V_i is the volume surrounding to atom *i*; N_R is the number of particles contained in region *R*, where *R* is defined as the region of atomic interaction; r_{ij} is the distance between atoms *i* and *j*; and r_{ij}^m and r_{ij}^n are two components of the vector from atom *i* to *j*. The first term of the bracketed section of equation (4.1) represents the kinetic effect associated with atomic motion, and will be affected by temperature. The second term is related to the interactive forces and the distance between the atoms. V_i is also named Voronoi volume, constructed by the perpendicular planes which bisect the lines between atom *i* and all its neighbor atoms. However, it is time-consuming to obtain the Voronoi volume of each atom, so Srolovitz [141] has used the following formulation to obtain a sphere whose volume is equal to the original Voronoi volume, namely,

$$V_i = \frac{4\pi}{3} a_i \tag{4.2}$$

where a_i is the average radius of atom *i*, and r_{ij} is the distance between atoms *i* and its

neighbor atom *j*.

Fig. 4.2(a)-(f) depict the morphologies of nickel atoms with a coordination number lower than 12, and which correspond to the morphologies at different indentation depths on the (100) surface, marked as labels (1)-(6). The morphologies at labels (1), (3), and (5) are located at the local peaks of the (100) indentation curve, while those at labels (2), (4), and (6) are at local minimums of the tip forces. The tip force will decrease when the indentation depths increase from label (1) to (2), label (3) to (4), and label (5) to (6), because the strain energy of the substrate due to the force exerted by the tip will be released by the dislocation-sliding along the {111} plane. After the release of strain energy, the indentation curve continues to rise after crossing the local minimums until the deformation energy of the next stage is released again.

As shown in Fig. 4.2(a), (c) and (e), the atomic arrangements display the homogeneous nucleation phases. Because Fig. 4.2(a) occurs at the shallow indentation stage, the formation size of nucleation is not significant in size. With the increase of indentation depth, as shown in Fig. 4.2(c) and (e), more nickel atoms nucleate around the tip, which leads to the formation of a larger nucleation. According to the stress legend in Fig. 4.2(a), (c) and (e), the nucleated atoms around the tip reveal repulsive stresses. The atomic normal stresses increase with the indentation depth, in that the maximum atomic stresses in Fig. 4.2(a), (c) and (e) for indentation depths of 5.1 Å, 9.2 Å, and 13.3 Å are about -0.06 GPa, -0.09 GPa and -0.11 GPa, respectively. In contrast, the atomic arrangements in Fig. 4.2(b), (d) and (f) display the phases where dislocation from the nucleation phase takes place. In Fig. 4.2(b), because the indentation depth into the nickel substrate by the tip is not sufficient, the areas of the sliding planes are relatively small.

With increase of the indentation depth, as shown in Fig. 4.2(d) and (f), the dislocation defects gradually enlarge, which results in larger areas of sliding planes. From the displays of the stress legend in Fig. 4.2(b), (d) and (f), it can be seen that the distributions of the atomic normal stress values on the {111} sliding planes are close to the zero value after the relaxation period, where strain energy is released.

Fig. 4.3(a)-(f) and Fig. 4.4(a)-(f) also depict the morphologies of nickel atoms with the coordination number lower than 12, and which correspond to the morphologies at different indentation depths on both (110) and (111) surfaces at labels (7)-(12) and labels (13)-(18), respectively. The morphologies at labels (7), (9), and (11) are located at the local peaks of the (110) indentation curve, while those at labels (8), (10), and (12) are at local minimums of the tip forces. Similarly, the morphologies at labels (13), (15), and (17) are located at the local peaks of the (111) indentation curve, while those at labels (14), (16), and (18) are at local minimums of the tip forces. Fig. 4.1 shows the decrease in tip force from the local peaks to the local minimums between labels (7) and (8), labels (9) and (10), and labels (11) and (12); as well as labels (13) and (14), labels (15) and (16), and labels (17) and (18). This because the strain energy of the substrate due to the exertion of the tip is released by the dislocation along the {111} sliding plane.

The strain energy can be examined in further detail in Fig. 4.3 and 5.4. As previously noted, in Fig. 4.3(a), (c), and (e), the atomic arrangements display the homogeneous nucleation phases, and the formation size of nucleation increases with the increase of indentation depth. The nucleated atoms around the tip reveal the repulsive stresses, and the atomic normal stresses increase with the increase of indentation depth. The maximum atomic stresses in Fig. 4.3(a), (c), and (e) are about -0.08 GPa, -0.11 GPa and -0.12 GPa.

In Fig. 4.3(b), (d), and (f), the atomic structures display the dislocation defect phases, and the areas and quantities of the sliding planes increase with the increase of indentation depth, while the distributions of the atomic normal stress values on the {111} sliding planes in Fig. 4.3(b), (d), and (f) are close to the zero value. In Fig. 4.4(a)-(f), the deformation evolution and atomic stress state of the (111) substrate during indentation are similar to Fig. 4.2(a)-(f) and Fig. 4.3(a)-(f). The maximum values of atomic stress in Fig. 4.4(a), (c), and (e) are about -0.09 GPa, -0.11 GPa and -0.12 GPa, while the distributions of the atomic normal stress values on the {111} sliding planes in Fig. 4.4(b), (d), and (f) are close to the zero value. From the previously mentioned results shown in Fig. 4.2 to Fig. 4.4, the plastic deformation characteristics corresponding to the distributions of atomic normal stress illustrate that the strain energy of the substrate exerted by the tip is stored by the formation of the homogeneous nucleation in one phase, and is dissipated by the dislocation sliding of the {111} plane in the following phase.

Furthermore, the series of drop phenomena during nanoindentation found in the three indentation curves in Fig. 4.1 correspond to the dislocation nucleation patterns presented in Fig. 4.2 to Fig. 4.4, and which conform to the related research of MD simulations for the FCC single crystal metals of nanoindentation [126,142-145]. These patterns are identified in the (100) surface orientation substrate as prismatic dislocation loop [142], and in the (111) surface orientation substrate as the dislocation defects of the tetrahedral sessile lock [126], the three-fold symmetry dislocation [143-144] or the three unique {111} sliding planes [145]. Finally, because of different orientation surfaces in the three nickel substrates, the numbers of slip angles of {111} sliding planes in the three nickel substrates are different. The numbers of slip angles for the three nickel substrates

can be calculated from Wulff net projection [146]. The slip angle of {111} sliding planes in the (100) substrate is 54.7°, and the slip angles of {111} sliding planes in the (110) substrate are 35.3° and 90°, while the slip angles of {111} sliding planes in the (111) substrate are 0°, 70.5° and 109.5°. From these results of slip angle numbers of {111} sliding planes in the three nickel substrates corresponding to the trend variations of the indentation curves, it can be found that the steep variations of the indentation curve from the local peaks to the local minimums are affected by the numbers of slip angles of the {111} sliding plane. Because the steep variations of the indentation curve are related to the plastic deformation ability of the material substrates during nanoindentation, the steep variations of the three indentation curves in Fig. 4.1 decrease when the numbers of slip angles of the {111} sliding plane increase in the three nickel substrates. This indicates that the (111) nickel substrate exhibits more dislocation activity owing to the maximum number of three slip angles, and the (100) nickel substrate exhibits less dislocation activity due to the minimum number of only one slip angle, with the dislocation activity of the (110) nickel substrate between the (111) and (100) nickel substrates as a result of two slip angles.

4.1.2 Pile-up Patterns after Nanoindentation

The actual contact area between the tip and the specimen is determined by the shape of the out-of-plane displacement zone, which will affect the quantitative analysis of the material property measurements. Therefore, the pile-up patterns produced after nanoindentation are also observed in the present MD simulations. As shown in Fig. 4.5, the MD simulations show different surface profiles around the simulated tip for the three different surface orientations of nickel substrates. The MD simulated contour plots of the

out-of-plane displacement profiles display the pile-up patterns on the surface of the (100)-, (110)- and (111)-oriented surfaces. The MD simulated contour maps for the hillocks of pile-up patterns in Fig. 4.5 (a), (b) and (c) display a crisscross of two-fold symmetry for the (100)-oriented crystal, an edge formed by two meeting points of the two-fold symmetry for the (110)-oriented crystal, and a hexagon of three-fold symmetry for the (111)-oriented crystals, respectively. The pile-up contour maps for the three crystallographic nickel substrates in Fig. 4.5 show that the pile-up dislocations are significantly affected by different surface orientations. For nickel materials, Huang et al [147] utilized micro-indentation to investigate the surface deformation mode of a NiTi shape-memory alloy after the indentation and a subsequent thermal cycle. In addition, Barshilia et al [148] employed low-angle x-ray diffraction and atomic force microscopy (AFM) to study structural characterization and nano-hardness measurements on Cu/Ni multilayer coatings. The results in references [147] and [148] reveal that the pile-up patterns of the nickel-based material are visible around the indentation surface under nanoindentation, with the resultant indents “piling-up” above room temperature, and “sinking-in” at low temperatures. Corresponding to the pile-up investigations of references [147] and [148], our results show that the pile-up of nickel materials are produced by the tip around the indentation surface after indentation, which further confirms our present simulations, which are modeled at room temperature.

In order to further verify the simulated pattern accuracy, the pile-up patterns of the present simulations for the three crystallographic nickel substrates are compared with the research literature for both finite element method (FEM) simulations and experimental tests [40]. Fig. 2 of reference [40] shows FEM simulation contour plots of the

out-of-plane displacement profiles on (100)-, (110)- and (111)-oriented surfaces for single crystal copper samples. Similarly, Fig. 3 of reference [40] shows the atomic force microscopy (AFM) images for experimental nanoindentation tests on the same orientation crystallographic surfaces and the same single crystal copper material. A comparison of pile-up patterns in the present simulations to reference [40] shows that the contour shape of the MD simulation is similar to both the FEM simulation and experimental results. The differences for the detailed contour are attributable to the fact that the maximum indentation depth used in the present simulations is very shallow as compared with both Fig.2 and Fig. 3 of reference [40]. In addition, the small scale of pile-up patterns in MD simulations provides detail that is not present in FEM simulations and experimental tests. However, the pile-up patterns of the three nickel substrates in the present MD simulations are in good agreement with the FEM simulations and experimental tests in reference [40], which prove that the crystalline nickel materials demonstrate the pile-up phenomenon by nanoindentation on the nanoscale similar to the pile-up patterns of the bulk FCC materials on the micron-scale.

Finally, because the hillocks and extensions of the pile-up pattern on the indentation surface represent a dislocation spreading of the materials, both the hillock heights and extension lengths of the pile-up pattern in Fig. 4.5 can provide more information about plastic deformation ability. First, the heights of the largest hillock around the edge of the indentation hole in Fig. 4.5 (a), (b) and (c) are about 1.6 Å, 2.7 Å and 3.2 Å, respectively, and are clearly visible from the pile-up patterns in Fig. 4.5. Secondly, the lengths of the longest extension perpendicular to the edge of indentation hole in Fig. 4.5 (a), (b) and (c) are about 2.7 Å, 4.6 Å and 5.7 Å, respectively, and are also clearly visible from the

pile-up patterns of Fig. 4.5. In the three crystallographic nickel substrates, the (111) surface orientation exhibits the most pile-up dislocation spreading, the (100) surface orientation exhibits the least, with the extent of pile-up dislocation spreading in the (110) surface orientation in between. These results are consistent with the results found in reference [41] by Komanduri et al, who found that the amount of plastic deformation and the pile-up dislocation of the aluminum substrate around the indenter during nanoindentation were observed to be at the maximum on the (111) surface orientation. While Komanduri et al's study [41] provides pile-up details for the (111) orientation, our study presents not only the pile-up patterns for (100), (110), and (111) orientations, but also the corresponding indentation curves which display the effects of dislocation spreading. The fact that the (111) surface orientation exhibits more pile-up dislocation spreading can be seen in the numerous small variations on its indentation curve, as opposed to the steep variations found on the (100) and (110) indentation curves in Fig. 4.1.

4.1.3 Extracted Material Properties from Nanoindentation

In order to further understand the influence of three crystallographic orientation surfaces on the mechanical properties, the formulations developed by Oliver [149] are used to calculate the hardness and Young's modulus of the three crystallographic substrates. The Young's modulus is first calculated by the reduced elastic modulus E_r, which takes into account the combined elastic effects of indentation tip and substrates, as follows:

$$E_r = \frac{\sqrt{\pi} S}{2\sqrt{A}} \tag{4.3}$$

where E and ν are the Young's modulus and Poisson's ratio with the subscripts *s* and *i* representing the sample and tip, respectively. The material properties of the tip used in this study are E_i=1141 GPa and ν_i=0.07 [149-150]. The hardness is thus calculated from the equation below as follows:

$$\frac{1}{E_r} = \frac{(1-\nu_s^2)}{E_s} + \frac{(1-\nu_i^2)}{E_i} \tag{4.4}$$

where E and ν are the Young's modulus and Poisson's ratio with the subscripts *s* and *i* representing the sample and tip, respectively. The hardness is thus calculated from the equation below as follows:

$$H = \frac{P_{\max}}{A_p} = \frac{P_{\max}}{A(h_c)} \tag{4.5}$$

where $P_{\max}$ is the maximum load of the tip at the maximum depth, A_p is the contact area, h_c is the contact depth, and may be expressed as

$$h_c = h_{\max} - \varepsilon \cdot \frac{P_{\max}}{S} \tag{4.6}$$

where ε is the geometric constant of the tip. For the conical tip, it is given a value of 0.72; for the flat punch, it is given a value of 1; and for the paraboloid of revolution, a value of 0.75. After the calculations to the hardness and Young's modulus, the calculated results are compared with the values reported in literature, as shown in Table 5-1.

The hardness values found in Table 5-1 for the (100), (110), and (111) nickel substrates obtained from our simulations at the maximum indentation depth 1.5 nm are 16.7 GPa, 15.8 GPa and 15.1 GPa, respectively. Similarly, in other simulation research, the hardness value obtained from Saraev et al [142] using MD simulation of nanoindentation at the same indentation depth 1.5 nm is 14.8 GPa, whereas the hardness

values of nickel material obtained from nanoindentation experiments as reported in reference documents are in the range of 3.5 to 8.4 GPa [151-152,154-157]. Secondly, regarding the Young's modulus values in Table 5-1, the values of the (100), (110), and (111) nickel substrates obtained from our simulations are 288.07 GPa, 264.51 GPa, and 224.26 GPa, respectively. The Young's modulus values of nickel material obtained from nanoindentation experiments as reported in reference literature are in the range of 164 to 218 GPa [152-153,155,158]. As is evident, the hardness values of the three nickel substrates in our simulations are close to the hardness values produced in MD simulations under similar simulation conditions, yet higher than the experimental values as reported in the reference literature. Similarly, the Young's modulus values of the present simulations for the three nickel substrates are also higher than the experimental values reported in the reference literature. The differences of both the hardness and Young's modulus values between the experimental and the simulated results were attributed to a number of factors: the indentation size effect [41,142,159-162], the difference in specimen scale between experiment and simulation that results in a restriction of dislocation activity in MD simulations [163-165], the higher strain rate due to the higher indenter velocity in MD simulations as compared with experiments [129,166], the experimental scatter and surface roughness in experimental specimens [167], the true contact area value underestimation due to the pile-up phenomenon in MD simulations [161], and the different crystal texture between the perfect mono-crystalline used in MD simulations and experimental specimens which contain a variety of defects [162-165,168]. Although the material properties of both the hardness and Young's modulus values in our simulations are higher than the experimental values of the reference documents, the

simulated values for the hardness and Young's modulus obtained from our simulations are still within a reasonable range.

Furthermore, the hardness values of the three crystallographic nickel substrates calculated from the present simulations show that the hardness value of the (100) substrate is greatest, while the hardness value of the (110) substrate is smaller than the (100) substrate, and the hardness value of the (111) substrate is smallest. This is due to the fact that the (100) substrate has only one slip angle of the {111} sliding planes that occur during nanoindentation, which leads to a lower ability for plastic deformation, and results in a higher hardness value. In contrast, because the (111) substrate has three slip angles of the {111} sliding planes that occur during nanoindentation, the (111) substrate exhibits a better ability for plastic deformation, which leads to a lower hardness value. The (110) substrate has two slip angles of the {111} sliding planes that occur during nanoindentation, so the ability for plastic deformation is between the (100) and (111) substrate values, which leads to a hardness value in between the (100) and (110) substrates. The (100) surface orientation of FCC materials exhibits the maximum hardness value for the three crystallographic surface orientations, also shown in the research previously mentioned [41]. The results in reference [41] for the influence of orientation effect on the hardness values reveal that the hardness of the (100) crystallographic aluminum substrate exhibits the maximum value under nanoindentation, and represents the least anisotropy on the [001] direction. The results in our simulations for the hardness value of the (100) nickel substrate in the three surface orientations are in accord with the results of reference [41]. Because the hardness values of the three nickel substrates correspond to the numbers of slip angle at the {111} sliding planes, the

different slip angles lead to different dislocation activity during nanoindentation. This indicates that the hardness of FCC nickel material on the nanoscale is significantly affected by crystallographic surfaces with different orientations.

Finally, the Young's modulus values of the three crystallographic nickel substrates calculated from the present simulations show that the Young's modulus value of the (100) substrate is greatest, while the Young's modulus value of the (110) substrate is smaller than the (100) substrate, and the Young's modulus value of the (111) substrate is smallest. Because the Young's modulus is only related to the capability for elastic deformation, the material's resistance to elastic deformation at the moment of initial unloading is completely provided by the constitutional strength of atomic bonding. Therefore, a comparison of Young's modulus for the three nickel substrates can be drawn from the average cohesive energy between nickel atoms, as shown in Fig. 4.6, with the horizontal axis representing the indentation depth, and the vertical axis representing the average value of cohesive energy for all atoms of the nickel substrate, defined as the atomic bonding strength between nickel atoms. In Fig. 4.6, it can be clearly seen that throughout the entire indentation process, the (100) substrate has the maximum value of cohesive energy, while the cohesive energy of the (110) substrate is smaller than the (100) substrate from the indentation, and the cohesive energy of the (111) substrate always maintaining the minimum value. The Young's modulus values of the three nickel substrates have a proportional relationship to cohesive energy, which reveals that the elastic modulus of FCC nickel material on the nanoscale is significantly affected by the different crystallographic orientation surfaces.

4.2 The Nanoindentation Accuracy of Multiscale Crystal Ni Metal

In this section, we illustrate the computational efficiency and accuracy of the combined MD and FE approach. We take nanoindentation as an investigation problem for assessing the performance of the coupled method, and confirm the accuracy of our hybrid model as compared with the results of full MD simulations. The present coupling method adopted from references [69,84] was first applied to the nanoindentation problem and compared against full atomistics on a problem sized to be accessible using atomistics. The comparison between indentation curves of the full MD and the hybrid FE/MD simulations is summarized in Fig. 4.7. The vertical axis represents the value of the tip force, defined as the resultant force at the indenting direction exerted upon the tip by nickel atoms, and the horizontal axis represents the indentation depth. The height of the tip is set to zero indentation depth when the atoms of the tip start interacting with the nickel atoms of the substrate. The positive and negative values of the tip force represent the repulsive and attractive force between the tip and the nickel substrate, respectively.

From the results of Fig. 4.7, it can be seen that the indentation curves of both full MD and multiscale models are matched each other before the indentation depth 4.2 Å. After the indentation depth 4.2 Å, the indentation curve of the multiscale model displays quantitative differences in the evolution of trend variation as compared with the indentation curve of full MD model. The average gap value calculated from the indentation curves between the MD and multiscale models is smaller than 5%, even though the maximum gap value does not exceed 8%. The difference of indentation curves between the MD and multiscale models can be indicated as the below factors: the differently intrinsic theory between MD and FE to cause the inevitable discrepancy [69],

the FE precision unable to reach the precise level of MD for the descriptions of material behavior due to the coarse mesh grids of FE [69], the different boundary condition employed between MD and FE to make the divergence [64], and the innate diversity of fluctuation characteristic between MD and FE affected by the temperature effect to produce the inconsistent connection in the multiscale model [83]. After given the elucidations of above-mentioned factors, it is not surprising why the result of indentation curve for the multiscale simulations is unable to exactly match the full MD result of nanoindentation. Although there are quantitative differences in the indentation curve of multiscale model as compared with full MD solution; however, these differences do not significantly affect the indentation results of multiscale model because the entire trend variations of indentation curve for the multiscale simulations are similar to the indentation curve of full MD simulations. Therefore, the result of multiscale simulations from the indentation curve exhibits a good agreement with atomistic solution, which proves that the present multiscale model demonstrates the accuracy from nanoindentation on the nanoscale.

Finally, in order to further examine whether the coupling state between MD and FE in the present mutiscale model is seamlessly, we take the deformation morphology of nickel substrate exerted by the tip at the maximum indentation depth, as shown in Fig. 4.8. Under the highly plastic deformation exerted by the tip, the material deformation from the atomistic descriptions of MD region near the indentation zone to the grids descriptions of FE region away from the indenter has a smooth and continuous variation, which shows a consistent gradation in the entire region of multiscale model. Besides, a more powerful signature of seamless coupling represents a validation of the multiscale

model in Fig. 4.8, which is that the deformation profiles pass from the MD region to the FE regions with no visible discontinuity at the FE/MD interface; i.e., the coupling of the MD region to the FE region appears seamless; this observation remains true even at higher spatial magnifications. These features effectively test the adaptability of our multiscale model, which reveals that the fine scale waves pass out of the MD region properly at the same time as the coarse scale pulse propagates into the coarse scale region when the boundary condition is correctly applied.

4.3 The Nanoindentation Characteristics of Crystal GaN Metal Semiconductor

As described above, Fig. 3.4 is a typical cyclic load–displacement plot for GaN thin film with a maximum load up to 200 mN. It is evident that for load below 50 mN, the load–displacement curve appears to be rather smooth during the whole loading–unloading cycle. However, it starts to exhibit irregularities, characterized by small sudden displacement excursions (‘pop-ins’) indicated by the arrows, during loading. The first apparent pop-in occurred at a load about 60 mN. Subsequently, the pop-ins phenomena are randomly distributed on the loading curve. We note here that the critical applied load for direct identification of pop-in events in the load–displacement curve not only is dependent on the type of indenters used, but also even very much dependent on the test system and the maximum applied load used. For instance, Kucheyev et al [169] reported that the critical load for pop-in to occur varied in the range of ~24–40 mN for GaN films at an indentation load of 100 mN by using ANU UMIS-2000 Nanoindenter Systems with a spherical indenter tip. While, in our previous study [132], we found that the critical load for pop-in actually occurred in the range of ~1.2–1.5 mN for GaN films at an indentation load of 3 mN by using Hysitron Triboscope Nanoindenter Systems with

a Berkovich indenter tip. On the other hand, Ma et al [170] reported that, although pop-ins were evidently observed with 100 mN load in their system, there were no apparent features of pop-ins in the load–displacement curve when an indentation load of 500 mN was applied. They attributed it to the lack of enough resolution when larger load was applied. Another important feature to be noted is that there is no apparent 'irregularity' on any of the unloading segments, which has been regarded as a signature of absence of phase transformation [88,137]. The present results are largely in agreement with previous studies on GaN thin films [88,137,171], except that the values of the mechanical parameters are different (Table 4-1). We suspect that these discrepancies are mainly due to the various indentation methods used. For instance, the tip– surface contact configuration and stress distribution for the Berkovich indenter tip can be drastically different from that for the spherical tip or Vickers-type indenters.

The physical mechanism of the pop-ins appearing in the load–displacement curve has been extensively discussed in the literature. Among all, crack formation, sudden occurrence of pressure-induced phase transformation, and generation of slip bands due to dislocation propagation during the indentation process were identified to have occurred in different systems. Bradby et al [88], using the spherical indenter with a tip radius of 4.2 μm, first observed that in Wurtzite structure GaN films there existed multiple discontinuities upon loading. Since there was no crack and no pressure-induced phase transformation observed in their TEM investigation, they attributed the main deformation mechanism to nucleation of slip bands on the basal planes. In their more recent studies [171], cracks were found at the intersections of converging {111} slip bands in cubic structure GaAs. On the other hand, for hexagonal GaN and ZnO with two slip systems

(both the basal and pyramidal planes), although dislocations slipping on one system are impeded by the other during plastic deformation, there were no cracks formed for loads up to as high as 900 mN and 200 mN for GaN and ZnO, respectively [171]. Instead, there was a profound pile-up of the material far from the indenter contact diameter observed, suggesting that dislocations were being punched out into the surrounding material when loading continued. It is interesting to note that the similar multiple pop-ins characteristics were also observed in hexagonal structure InSe and GaSe single crystals [172]. In their high-temperature (370 $^{\circ}$C) Vickers diamond indentation experiments performed on (0001) N-polar GaN single crystals, Weyher et al [173] reported evidence of pressure-induced transition from the wurtzite to the energetically most favourable rocksalt structure a very high load of 2 N. Unfortunately, since there was no load–displacement measurement, it is not clear how the pop-in events correlate with phase transitions. Nevertheless, the above discussions do suggest that multiple pop-ins indeed are specific features of materials with hexagonal lattice structure and geometry of the indenter tip may play an important role in determining the nanoindentation-induced mechanical responses. Thus, in order to identify the deformation mechanisms specific to the Berkovich nanoindentation direct microstructure characterization in the vicinity of the indented area is needed.

The scanning electron microscopy (SEM) observation shown in the inset of Fig. 3.4 does not reveal any evidence of material pile-ups and signs of crack formation on the film surface around the indented area. There are no ‘pop-outs’ on the unloading curves either (Fig. 3.4), suggesting that phase transitions like that observed in indented Si [174] are probably not occurring beneath the indenter tip for GaN films. The absence of pop-out serration in the unloading segments load– displacement curves, surface pile-ups, and

cracks indicates that nanoindentation-induced deformation in GaN films is predominated by dislocation nucleation and propagations. Fig. 4.9(*a*) shows the bright-field TEM image, obtained by following the sample preparation procedures illustrated in Fig. 3.5, for a GaN film indented with a maximum load of 200 mN by a Berkovich indenter. It is evident from Fig. 4.9(*a*) that, for an estimated film thickness of 2 μm, the GaN film studied here shows almost perfect interface epitaxial relations with the sapphire substrate. Moreover, the image clearly displays that, within the film, the deformation features underneath the indented spot are primarily manifested by dislocation activities. Namely the slip bands are well aligned in parallel with the {0001} basal planes all the way down to the film–substrate interface. It is also interesting to note that the heavily strained features in the vicinity of the interface may not be just accidental artifacts resulting from sample preparation. They might be direct evidence for displaying that, due to the excellent interface epitaxy between film and substrate, the effects of indentation have, in fact, extended into the sapphire substrate. This argument may also partially explain that, due to the ease of relaxing the local stress right under the indenter's tip via the massive substrate, indentation-induced phase transitions were rarely observed.

In order to have a closer look at the dislocation activities immediately beneath the tip, Fig. 4.9(*b*) shows an enlarged TEM picture in the vicinity of the tip contact region. The picture clearly displays a typical microstructure of a heavily deformed material, characterized by features of very high density of dislocations. Nevertheless, the slip bands (dark thick lines in the photograph) clearly indicate that during the indentation the rapidly increasing dislocations can glide collectively along the easy directions. In the present case, in addition to those aligning parallel to the GaN–sapphire interface along

the (0001) basal planes, slip bands oriented at ~60° to the sample surface can also be found. The 60° slip bands, which are believed to originate from dislocations gliding along the $\{10\bar{1}1\}$ pyramidal planes, however, are distributed in much shallower regions near the contacting surface. It is indicative that a much higher stress level is needed to activate this slip system as compared with the one along the basal planes. Fig. 4.10 shows a more detailed microstructure near the intersections of the two sets of slip bands. The distorted slip bands and the extremely high dislocation densities at the intersections indicate the highly strained state of the material. However, even at the submicron scale, no evidence of subsurface cracking and film fragmentation was observed. In addition, the selected area diffraction (not shown here) of the heavily damaged regions did not show evidence of newly formed phases either.

From the above observations and discussion, it is apparent that, in the Berkovich indentation scheme, the primary deformation mechanism for GaN films is dislocation nucleation and propagation along easy slip systems, similar to that concluded with a spherical indenter [88]. Since the pop-in events are usually observed after permanent plastic deformation has occurred (50 mN in the present case) and two of the possible mechanisms, the deformation-induced phase transition and fracture of film [175] were basically ruled out, the most likely mechanism responsible for the pop-ins appears to be associated with the activation of dislocation sources [176]. In this scenario, plastic deformation prior to the pop-in event is associated with the individual movement of a small number of newly nucleated and pre-existing dislocations. As the number of dislocations is increased and entangled with each other, large shear stress is quickly accumulated underneath the indenter tip. When the local stress underneath the tip reaches

some threshold level, a burst of collective dislocation movement on the easy slip systems is activated, leading to a large release of local stress and a pop-in event on the load–displacement curve. Each of these collective dislocation movements is reflected as a slip band in the indented microstructure displayed in Fig. 4.9. Notice that, although the slip bands appeared to stop near the film–substrate interface (Fig. 4.9(*a*)), the released stress due to this effect could extend deep into the substrate as mentioned above. Moreover, the narrow spacing of the dense bands of defects and/or dislocations along the basal planes near the surface suggests that, in the later stage of indentation, a large indentation load, such as the 200 mN used in the present experiments, starts to activate extensive slip bands along the 60° pyramidal planes. The extensive interactions between the dislocations slipping along the two slip systems, thus, confined the slip bands in a shallow regime, which, in turn, resulted in a heavily deformed and strain-hardened lattice structure. Finally, we note that the so-called 'slip-stick' behaviour [88], characterized by material pile-ups caused by interactions between the as-grown defects and the indentation-induced dislocations, is not significant in this study. Whether it is due to the insignificant grown-in defect density of our GaN films or to the specific geometric shape of the indenter tip used is not clear at present and further studies may be required to clarify this issue.

Table 4-1 A comparison of the material properties of three nickel crystallographic substrates with (100), (110), and (111) orientation

	H (GPa)			*E* (GPa)		
Surface orientation	**(100)**	**(110)**	**(111)**	**(100)**	**(110)**	**(111)**
MD simulation results	**16.7**	**15.8**	**15.1**	**288.07**	**264.51**	**224.26**
MD simulation values in Reference literature	**14.8 [142]**	—	—	—	—	—
Experimental values in the reference literature (Surface orientation unknown)	**3.5-8.4 [151-152,154-157]**			**164-218 [152-153,155,158]**		

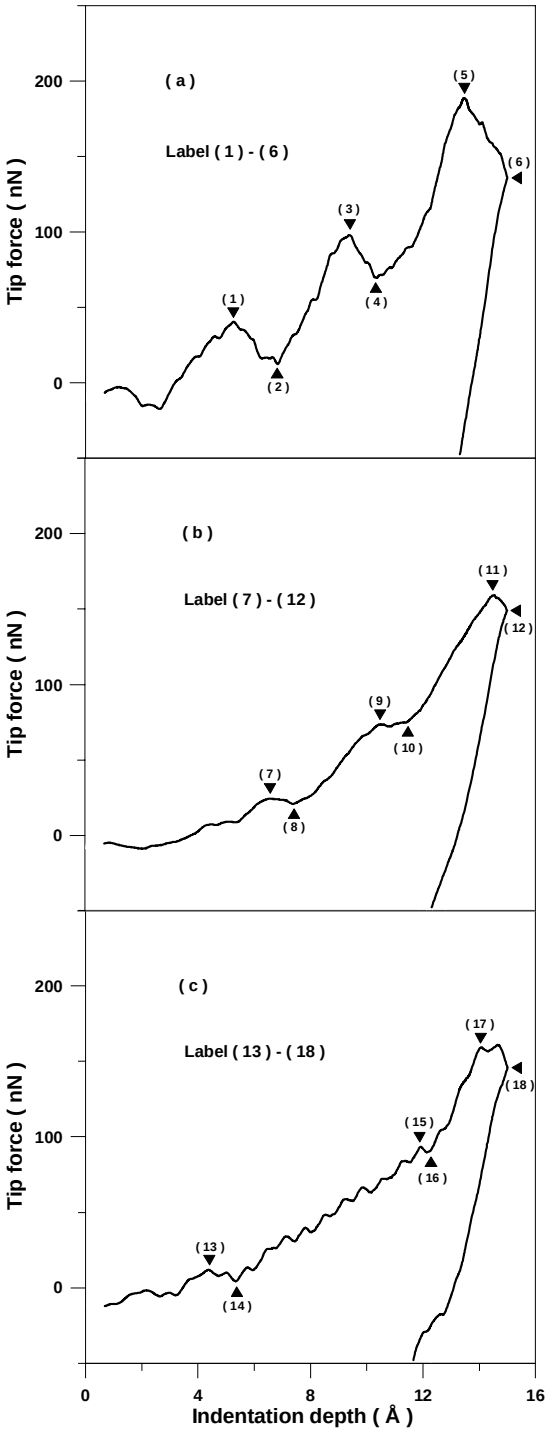

Fig. 4.1 Indentation curves of the three nickel substrates.

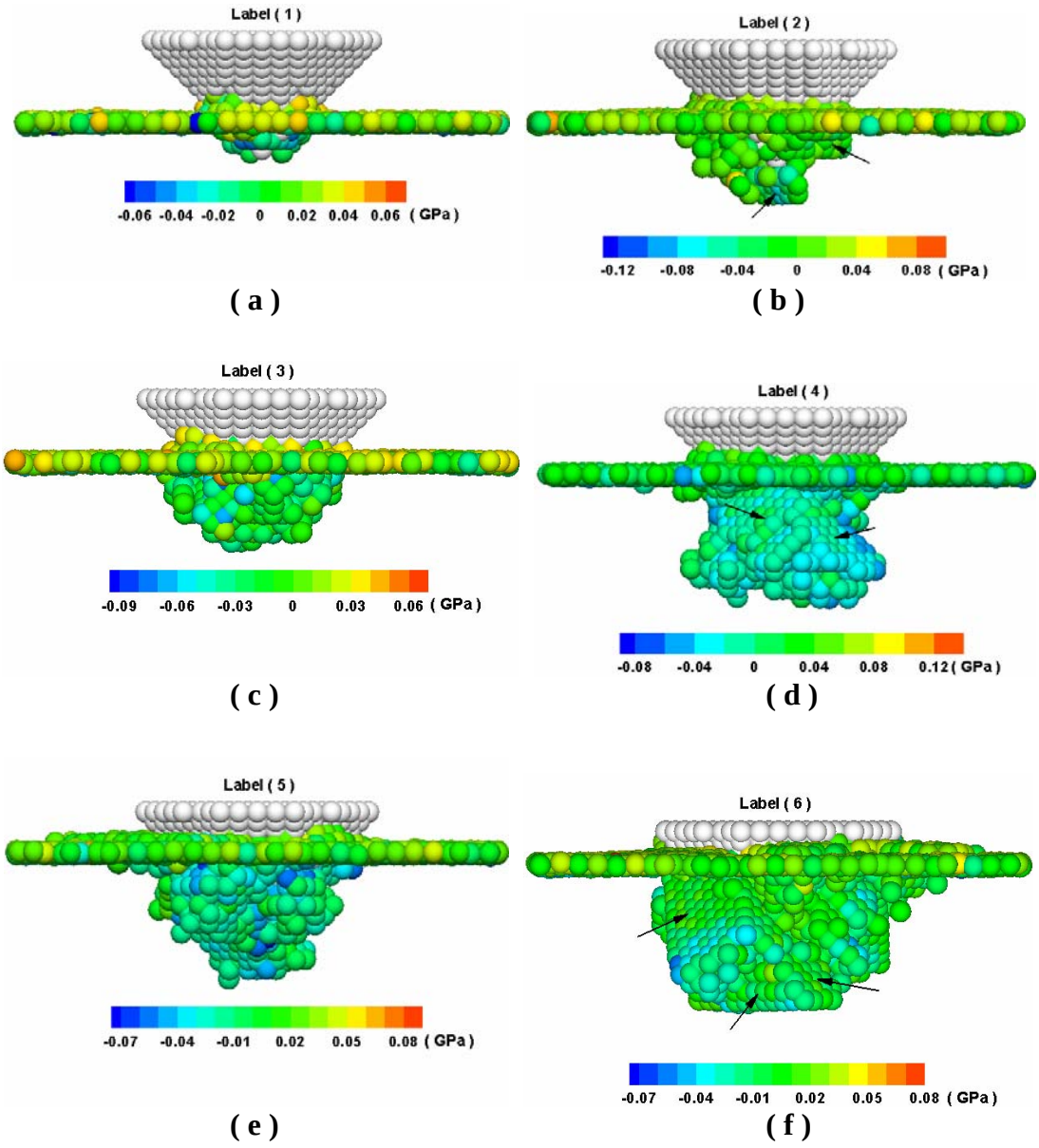

Fig. 4.2 Three dimension snapshots of nickel (100) crystallographic substrate in different indentation depths.

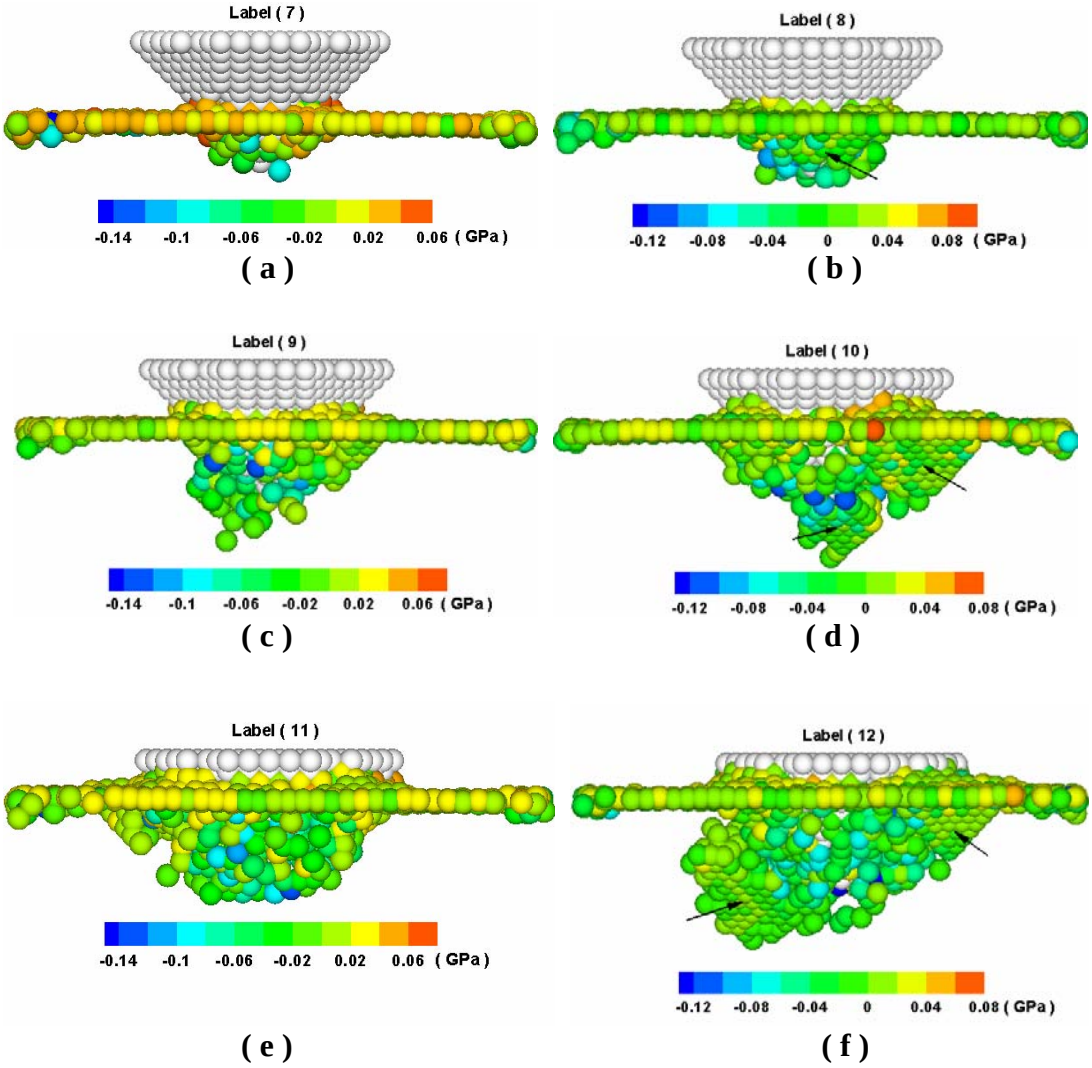

Fig. 4.3 Three dimension snapshots of nickel (110) crystallographic substrate in different indentation depths.

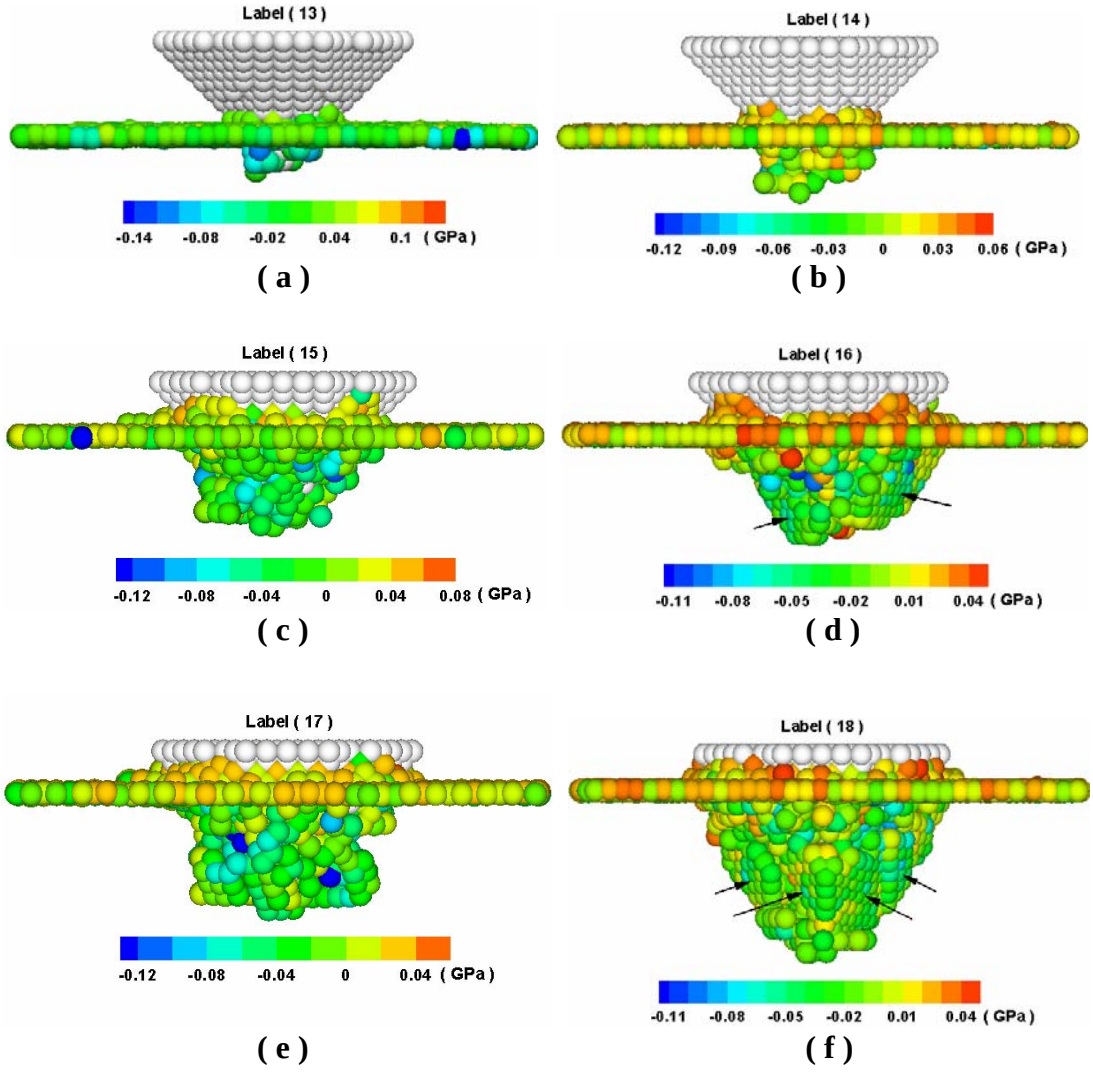

Fig. 4.4 Three dimension snapshots of nickel (111) crystallographic substrate in different indentation depths.

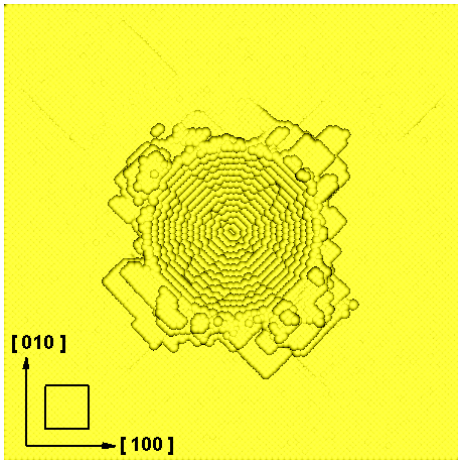

(a)

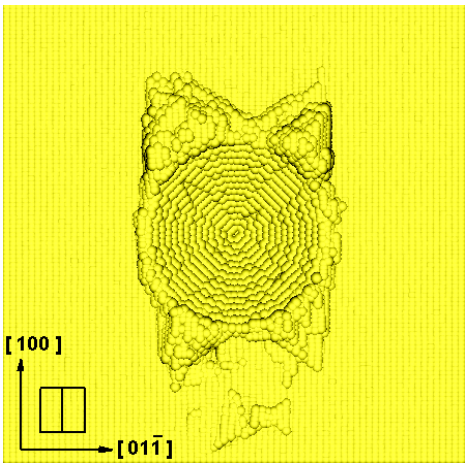

(b)

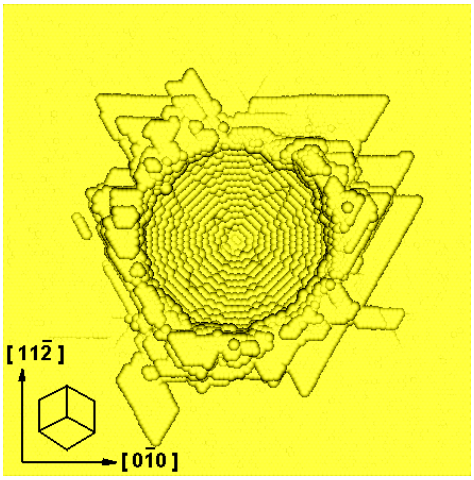

(c)

Fig. 4.5 Pile-up patterns of the top view for the (a) (100), (b) (110) and (c) (111) oriented nickel single crystal surfaces obtained from the present MD simulation.

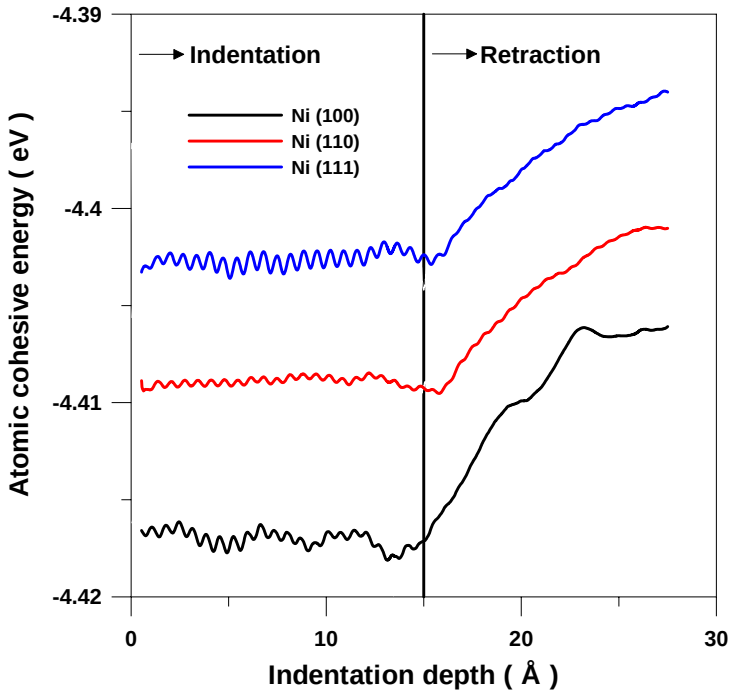

Fig. 4.6 The cohesive energy curves between nickel atoms of the crystallographic nickel substrates with (100), (110) and (111) orientation surfaces.

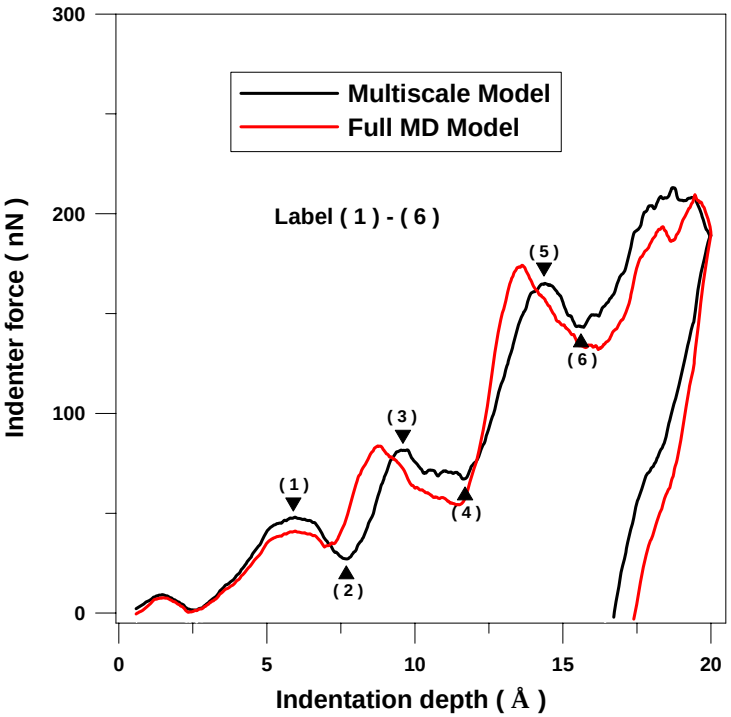

Fig. 4.7 Indentation curves of the nickel substrate of both multiscale and full MD models.

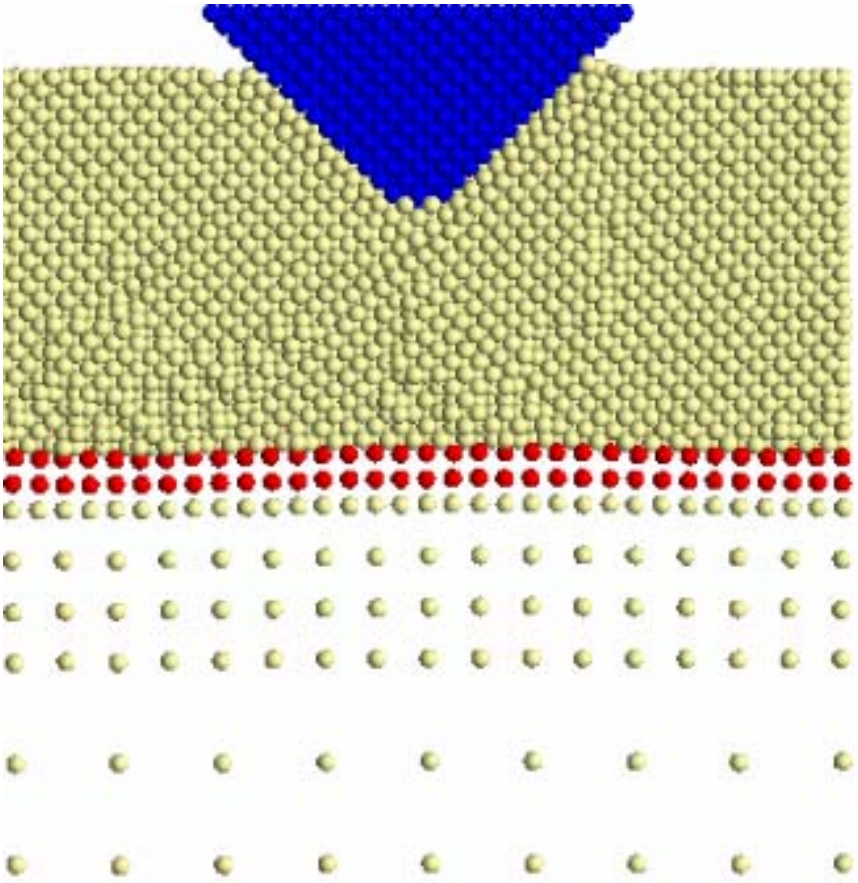

Fig. 4.8 Close-up snapshot for the deformation morphology of multiscale model from the lateral view of nickel substrate exerted by the tip at the maximum indentation depth.

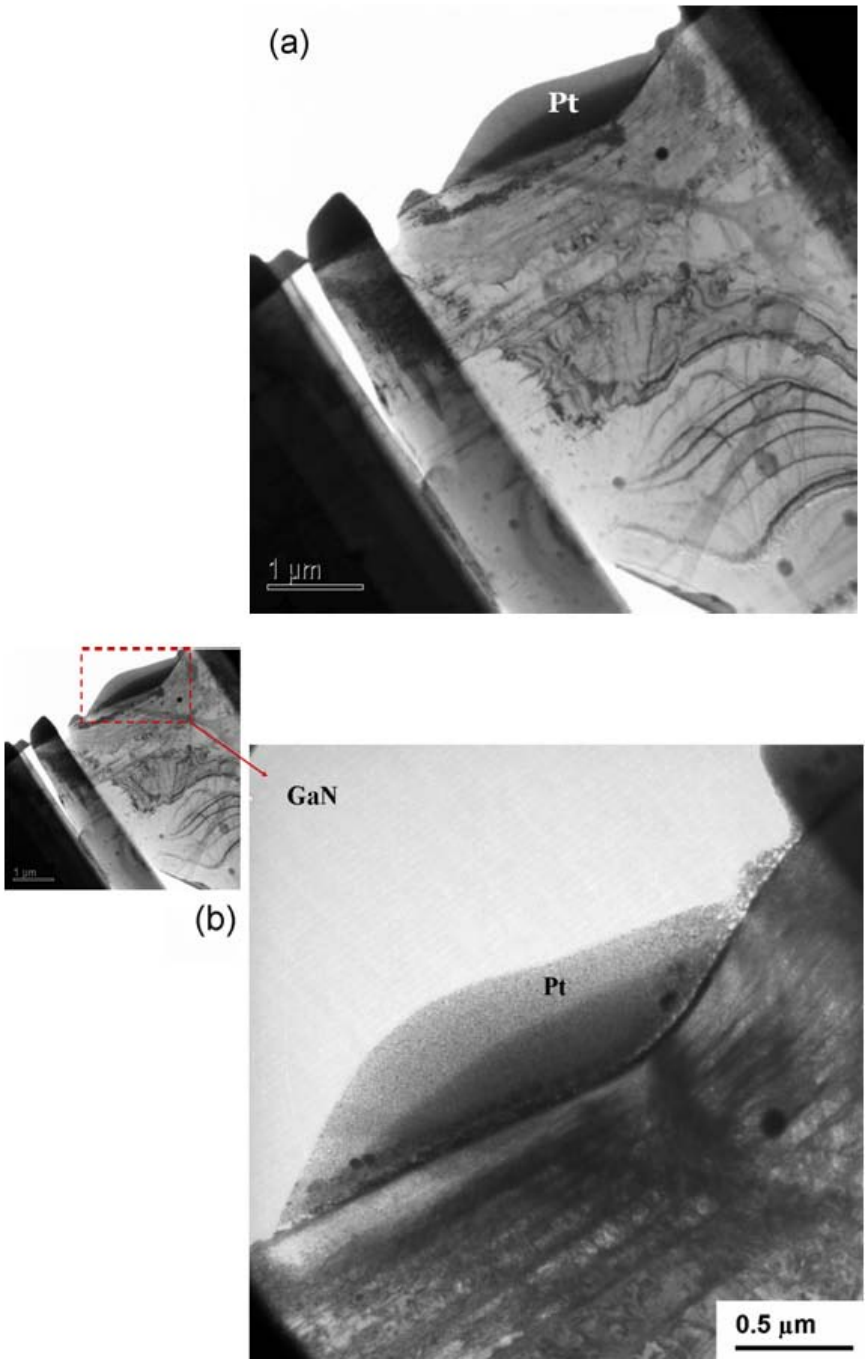

Fig. 4.9 TEM Bright-field images of specimen after an indentation load to 200 mN.

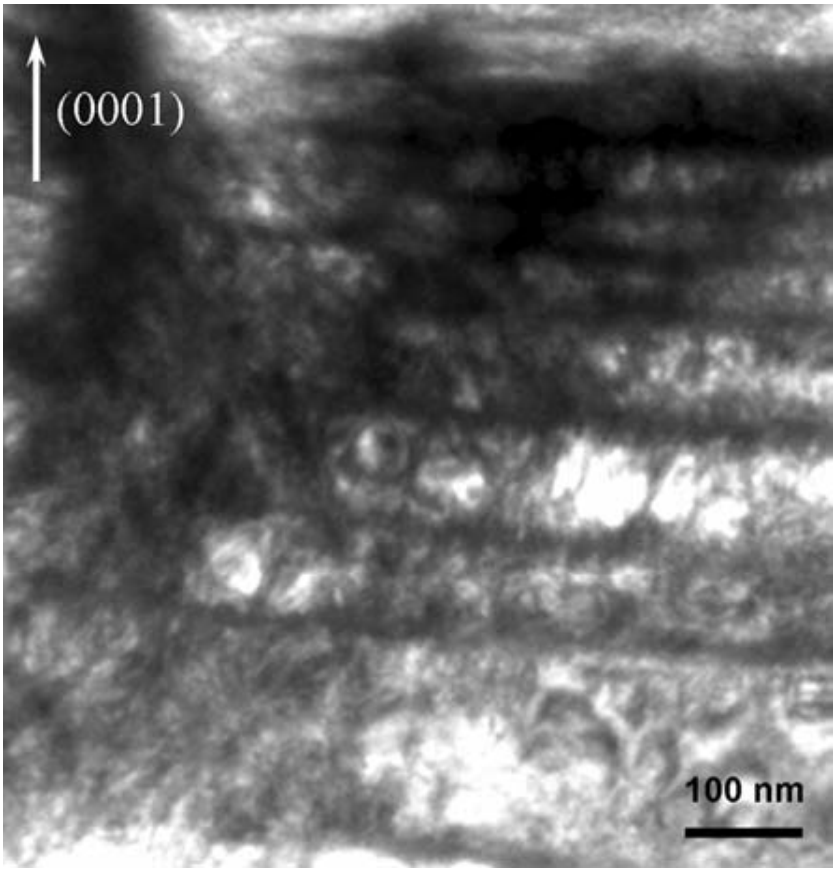

Fig. 4.10 A close-up view of TEM bright-field image of the heavily deformed region of the GaN thin film.

Chapter 5 Conclusion

5.1 Summary

The numerical analysis and the experimental test are performed on the study for the material characteristics of metal thin films by using nanoindentation technique. From the present results of nanoindentation, the conclusions of the present studies can be summarized as follows:

Firstly, the strain energy of the substrate exerted by the tip is stored by the formation of homogeneous nucleation, and is dissipated by the dislocation sliding of the {111} plane. The steep variations of the indentation curve are affected by the numbers of slip angles of the {111} sliding plane. The pile-up patterns of the three nickel substrates prove that the crystalline nickel materials also produce the pile-up phenomenon by nanoindentation under the nanoscale. The effects of FCC surface orientation in material properties on the nanoscale are observable through the slip angle numbers which influence hardness values, as well as the cohesive energy of different crystallographic surfaces that indicate Young's modulus.

Secondly, the indentation curve of multiscale simulations exhibits a good agreement with atomistic solution, which proves that the accuracy of the present multiscale model. The deformation profiles display a consistent gradation in the entire region and reflect no visible discontinuity at the FE/MD interface, which demonstrates that the coupling for MD and FE in the multiscale model is seamlessly.

Finally, the primary nanoindentation-induced deformation mechanism in GaN thin films is nucleation and propagation of dislocations. The basal and pyramidal planes of GaN lattice are acting as the primary slip systems for collective dislocation motions, with

the latter being activated at a higher stress state and hence later stage of indentation.

5.2 Future Prospects

For the future prospects, the following is the research directions that may be identified as necessary and potentially profitable, included as follows: MD simulations on the material characteristics of ZrNi amorphous alloy by using nanoindentation; MD simulations on the material characteristics of high polymer and biomolecular substrates by using nanoindentation; the multiscale simulations for the coupling of molecular dynamics, molecular statics and finite element method; the multiscale simulations for the coupling of ab initio, molecular dynamics and finite element method; the fullscale simulations for the coupling of ab initio, molecular dynamics, molecular statics and finite element method.

References

[1] A. Gouldstone, H. J. Koh, K. Y. Zeng, A. E. Giannakopoulos, S. Suresh. Discrete and continuous deformation during nanoindentation of thin films. Acta Mater., **48**, 2277 (2000).

[2] A. A. Voevodin, M. A. Capano, S. J. P. Laube, M. S. Donley, J. S. Zabinski. Design of a Ti/TiC/DLC functionally gradient coating based on studies of structural transitions in Ti-C thin films. Thin Solid Films, **298**, 107 (1997).

[3] B. Alder, T. Wainwright. Studies in molecular dynamics: I. General method. J. Chem. Phys., **31**, 459 (1959).

[4] B. Alder, T. Wainwright. Studies in molecular dynamics: II. Behavior of a small number of elastic spheres. J. Chem. Phys., **33**, 1439 (1960).

[5] W. G. Hoover, A. J. De Groot, C. G. Hoover, I. F. Stowers, T. Kawai, B. L. Holian, T. Boku, S. Ihara, J. Belak. Large scale elastic-plastic indentation simulations via non-equilibrium molecular dynamics. Phys. Rev. A, **42**, 5844 (1990).

[6] J. Belak, D. B. Boercker, I. F. Stowers. Simulation of nanometer scale deformation of metallic and ceramic surfaces. MRS Bull., **18**, 55 (1993).

[7] U. Landman, W. D. Luedtke, N. A. Burnham, R. J. Colton. Atomistic mechanisms and dynamics of adhesion, nanoindentation, and fracture. Science, **248**, 454 (1990).

[8] U. Landman, W. D. Luedtke. Nanomechanics and dynamics of tip-substrate interactions. J. Vac. Sci. Technol., **9**, 414 (1991).

[9] U. Landman, W. D. Luedtke, E. M. Ringer. Atomistic mechanisms of adhesive contact formation and interfacial processes. Wear, **153**, 3 (1992).

[10] U. Landman, W. D. Luedtke. Atomistic dynamics of interfacial processes: films, junctions, and nanostructure. Appl. Surf. Sci., **92**, 237 (1996).

[11] R. Komanduri, N. Chandrasekaran, L. M. Raff. MD simulation of nanometric cutting of single crystal aluminum-effect of crystal orientation and direction of cutting. Wear, **242**, 60 (2000).

[12] R. Komanduri, N. Chandrasekaran, L. M. Raff. Effect of tool geometry in nanometric cutting: a molecular dynamics simulation approach. Wear, **219**, 84 (1998).

[13] S. Shimada. Molecular dynamics analysis of nanometric cutting process. Int. J. Jpn. Soc. Precis. Eng., **29**, 283 (1995).

[14] T. Inamura, H. Suzuki, N. Takezawa. Cutting experiments in a computer using atomic models of copper crystal and diamond tool. Int. J. Jpn. Soc. Precis. Eng., **25**, 259 (1991).

[15] K. Maekawa, A. Itoh. Friction and tool wear in nanoscale machining-molecular dynamics approach. Wear, **188**, 115 (1995).

[16] N. Chandrasekaran, A. Noori-Khajavi, L. M. Raff, R. Komanduri. A new method for molecular dynamics simulation of nanometric cutting. Philos. Mag., **77**, 7 (1998).

[17] R. Komanduri, N. Chandrasekaran, L. M. Raff. Some aspects of machining with negative rake tools simulating grinding: an MD simulation approach. Philos. Mag., **79**, 955 (1999).

[18] O. Tomagnini, F. Ercolessi, E. Tosatti. Microscopic interaction between a gold tip and lead surface. Surf. Sci., **287**, 1041 (1993).

[19] D. W. Brenner, S. B. Sinnott, J. A. Harrison, O. A. Shenderova. Simulated engineering of nanostructures. Nanotechnology, **7**, 161 (1996).

[20] R. Rentsch, I. Inasaki. Indentation simulation on brittle materials by molecular dynamics. SPIE, **2596**, 214 (1995).

[21] J. A. Harrison, D. W. Brenner, C. T. White, R. J. Colton. Atomistic mechanisms of adhesion and compression of diamond surfaces. Thin Solid Films, **206**, 213 (1991).

[22] W. Yan, K. Komvopoulos. Three-dimensional molecular dynamics analysis of atomic-scale indentation. J. Tribol.-Trans. ASME, **120**, 385 (1998).

[23] J. A. Harrison, C. T. White, R. J. Colton, D. W. Brenner. Molecular dynamics simulations of atomic scale friction of diamond surfaces. Phys. Rev. B, **46**, 9700 (1992).

[24] A. Buldum, S. Ciraci. Contact, nanoindentation, and sliding friction. Phys. Rev. B, **57**, 2468 (1998).

[25] D. E. Kim, N. P. Suh. Molecular dynamics investigation of two dimensional atomic scale friction. J. Tribol.-Trans. ASME, **116**, 225 (1994).

[26] M. Hirano, K. Shinjo. Atomistic locking and friction. Phys. Rev. B, **41**, 11837 (1990).

[27] R. Komanduri, N. Chandrasekaran, L. M. Raff. Molecular dynamics simulation of atomic-scale friction. Phys. Rev. B, **61**, 14007 (2000).

[28] P. Walsh, R. K. Kalia, A. Nakano, P. Vashishta. Amorphization and anisotropic fracture dynamics during nanoindentation of silicon nitride: A multimillion atom molecular dynamics study. Appl. Phys. Lett., **77**, 4332 (2000).

[29] P. Walsh, A. Omeltchenko, R. K. Kalia, A. Nakano, P. Vashishta. Nanoindentation of silicon nitride: A multimillion-atom molecular dynamics study. Appl. Phys. Lett., **82**, 118 (2003).

[30] J. F. Lin, C. C. Wei, Y. K. Yung, C. F. Ai. The effects of hydrogenated carbon films with different film thickness and nitrogen content on specimen mechanical properties, scratch critical load, adhesion work and tribological behavior. Diam. Relat. Mat., **13**, 1895 (2004).

[31] K. -D. Bouzakis, S. Hadjiyiannis, G. Skordaris, I. Mirisidis, N. Michailidis, K. Efstathiou, E. Pavlidou, G. Erkens, R. Cremer, S. Rambadt, I. Wirth. The effect of coating thickness, mechanical strength and hardness properties on the milling performance of PVD coated cemented carbides inserts. Surf. Coat. Technol., **177**,

657 (2004).

[32] B. C. Zhang, G. Barth, H. K. Liu, S. Chang. Characterization of nickel phosphorus surface by ToF-SIMS. Appl. Surf. Sci., **231**, 868 (2004).

[33] R. Ji, T. Liew, C. H. Seek, T. C. Chong. Corrosive effect of acrylic acid on magnetic head and media of an operating hard disk drive. Tribol. Int., **38**, 692 (2005).

[34] D. Son, J. J. Kim, J. Y. Kim, D. Kwon. Tensile properties and fatigue crack growth in LIGA nickel MEMS structures. Mater. Sci. Eng. A-Struct. Mater. Prop. Microstruct. Process., **406**, 274 (2005).

[35] E. Slavcheva, W. Mokwa, U. Schnakenberg. Electrodeposition and properties of NiW films for MEMS application. Electrochim. Acta, **50**, 5573 (2005).

[36] B. Li, Q. Chen, D. G. Lee, J. Woolman, G. P. Carman. Development of large flow rate, robust, passive micro check valves for compact piezoelectrically actuated pumps. Sens. Actuator A-Phys., **117**, 325 (2005).

[37] E. Gomez, E. Pellicer, M. Duch, J. Esteve, E. Valles. Molybdenum alloy electrodeposits for magnetic actuation. Electrochim. Acta, **51**, 3214 (2006).

[38] M. Zhao, C. Jiang, S. Li, S. X. Mao. Probing nano-scale mechanical characteristics of individual semi-conducting nanobelts. Mater. Sci. Eng. A-Struct. Mater. Prop. Microstruct. Process., **409**, 223 (2005).

[39] F. K. Mante, G. R. Baran, B. Lucas. Nanoindentation studies of titanium single crystals. Biomaterials, **20**, 1051 (1999).

[40] Y. Wang, D. Raabe, C. Kluber, F. Roters. Orientation dependence of nanoindentation pile-up patterns and of nanoindentation microtextures in copper single crystals. Acta Mater., **52,** 2229 (2004).

[41] R. Komanduri, N. Chandrasekaran, L. M. Raff. MD simulation of indentation and scratching of single crystal aluminum. Wear, **240**, 113 (2000).

[42] O. Kum. Orientation effects of elastic-plastic deformation at surfaces: nanoindentation of nickel single crystals. Mol. Simul., **31**, 115 (2005).

[43] Z. L. Wang, R. P. Gao, P. Poncharal, W. A. de Heer, Z. R. Dai, Z. W. Pan. Mechanical and electrostatic properties of carbon nanotubes and nanowires. Mater. Sci. Eng. C, **16**, 3 (2001).

[44] J. W. Kang, H. J. Hwang. Mechanical deformation study of copper nanowire using atomistic simulation. Nanotechnology, **12**, 295 (2001).

[45] H. Rafii-Tabar. Modelling the nano-scale phenomena in condensed matter physics via computer-based numerical simulations. Phys. Reports—Rev. Sec. Phys. Lett., **325**, 240 (2000).

[46] J. K. Diao, K. Gall, M. L. Dunn. Atomistic simulation of the structure and elastic properties of gold nanowires. J. Mech. Phys. Solids, **52**, 1935 (2004).

[47] X. Z. Sun, S. J. Chen, K. Cheng, D. H. Huo, W. J. Chu. Multiscale simulation on nanometric cutting of single crystal copper. Proc. Inst. Mech. Eng. Part B-J. Eng. Manuf., **220**, 1217 (2006).

[48] J. H. Argyris, H. P. Mlejnek. Dynamics of structure. Elsevier, Amsterdam (1991).

[49] T. Belytschko, T. J. R. Hughes. Computational Methods for Transient Analysis. Elsevier, Amsterdam (1983).

[50] H. S. Park, W. K. Liu. An introduction and tutorial on multiple-scale analysis in solids. Comput. Methods Appl. Mech. Engrg., **193**, 1733 (2004).

[51] F. F. Abraham. Dynamically spanning the length scales from the quantum to the continuum. Int. J. Mod. Phys. C, **11**, 1135 (2000).

[52] W. K. Liu, H. S. Park, D. Qian, E. G. Karpov, H. Kadowaki, G. J. Wagner. Bridging scale methods for nanomechanics and materials. Comput. Meth. Appl. Mech. Eng., **195**, 1407 (2006).

[53] S. P. Xiao , W. X. Yang. A temperature-related homogenization technique and its implementation in the meshfree particle method for nanoscale simulations. Int. J. Numer. Methods Eng., **69**, 2099 (2007).

[54] D. Qian, G. J. Wagner, W. K. Liu. A multiscale projection method for the analysis of carbon nanotubes. Comput. Meth. Appl. Mech. Eng., **193**, 1603 (2004).

[55] R. E. Rudd, J. Q. Broughton. Concurrent coupling of length scales in solid state systems. Phys. Status Solidi B-Basic Solid State Phys., **217**, 251 (2000).

[56] H. S. Park, E.G. Karpov, P. A. Klein, W. K. Liu. Three-dimensional bridging scale analysis of dynamic fracture. J. Comput. Phys., **207**, 588 (2005).

[57] H. S. Park, E. G. Karpov, W. K. Liu, P. A. Klein. The bridging scale for two-dimensional atomistic/continumn coupling. Philos. Mag., **85**, 79 (2005).

[58] R. Miller, E. B. Tadmor, R. Phillips, M. Ortiz. Quasicontinuum simulation of fracture at the atomic scale. Model. Simul. Mater. Sci. Eng., **6**, 607 (1998).

[59] J. Q. Broughton, F. F. Abraham, N. Bernstein, E. Kaxiras. Concurrent coupling of length scales: Methodology and application. Phys. Rev. B, **60**, 2391 (1999).

[60] F. F. Abraham, J. Q. Broughton, N. Bernstein, E. Kaxiras. Spanning the length scales in dynamic simulation. Comput. Phys., **12**, 538 (1998).

[61] S. Kohlhoff, P. Gumbsch, H. F. Fischmeister. Crack propagation in b.c.c. crystals studied with a combined finite-element and atomistic model. Philos. Mag., **64**, 851 (1991).

[62] Y. Wang, D. Raabe, C. Kluber, F. Roters. Orientation dependence of nanoindentation pile-up patterns and of nanoindentation microtextures in copper single crystals. Acta Mater., **52,** 2229 (2004).

[63] J. Knap, M. Ortiz. An analysis of the quasicontinuum method. J. Mech. Phys. Solids, **49**, 1899 (2001).

[64] R. C. Picu. Atomistic-continuum simulation of nano-indentation in molybdenum. J. Comput-Aided Mater. Des., **7**, 77 (2000).

[65] V. B. Shenoy, R. Phillips, E. B. Tadmor. Nucleation of dislocations beneath a plane strain indenter. J. Mech. Phys. Solids, **48**, 649 (2000).

[66] G. S. Smith, E. B. Tadmor, E. Kaxiras. Multiscale simulation of loading and electrical resistance in silicon nanoindentation. Phys. Rev. Lett., **84**, 1260 (2000).

[67] G. S. Smith, E. B. Tadmor, N. Bernstein, E. Kaxiras. Multiscale simulations of silicon nanoindentation. Acta Mater., **49**, 4089 (2001).

[68] P. Liu, Y. W. Zhang, C. Lu. A three-dimensional concurrent atomistic/continuum analysis of an epitaxially strained island. J. Appl. Phys., **94**, 6350 (2003).

[69] E. Lidorikis, M. E. Bachlechner, R. K. Kalia, A. Nakano, P. Vashishta, G. Z. Voyiadjis. Coupling length scales for multiscale atomistics-continuum simulations: Atomistically induced stress distributions in Si/Si3N4 nanopixels. Phys. Rev. Lett., **87**, 086104 (2001).

[70] H. S. Park, E. G. Karpov, W. K. Liu. A temperature equation for coupled atomistic/continuum simulations. Comput. Meth. Appl. Mech. Eng., **193**, 1713 (2004).

[71] G. J. Wagner, W. K. Liu. Coupling of atomistic and continuum simulations using a bridging scale decomposition. J. Comput. Phys., **190**, 249 (2003).

[72] C. Wen, J. Fish. A generalized space-time mathematical homogenization theory for bridging atomistic and continuum scales. Int. J. Numer. Methods Eng., **67**, 253 (2006).

[73] S. Q. Tang, T. Y. Hou, W. K. Liu. A mathematical framework of the bridging scale method. Int. J. Numer. Methods Eng., **65**, 1688 (2006).

[74] S. Q. Tang , T. Y. Hou, W. K. Liu. A pseudo-spectral multiscale method: Interfacial conditions and coarse grid equations. J. Comput. Phys., **213**, 57 (2006).

[75] V. B. Shenoy, R. Miller, E. B. Tadmor, R. Phillips, M. Ortiz. Quasicontinuum models of interfacial structure and deformation. Phys. Rev. Lett., **80**, 742 (1998).

[76] E. B. Tadmor, M. Ortiz, R. Phillips. Quasicontinuum analysis of defects in solids. Philos. Mag., **73**, 1529 (1996).

[77] R. E. Rudd, J. Q. Broughton. Coarse-grained molecular dynamics and the atomic limit of finite elements. Phys. Rev. B, **58**, R5893 (1998).

[78] M. Dewald, W. A. Curtin. Analysis and minimization of dislocation interactions with atomistic/continuum interfaces. Model. Simul. Mater. Sci. Eng., **14**, 497 (2006).

[79] B. Q. Luan, S. Hyun, J. F. Molinari. Multiscale modeling of two-dimensional contacts. Phys. Rev. E, **74**, 046710 (2006).

[80] W. A. Curtin, R. E. Miller. Atomistic/continuum coupling in computational materials science. Model. Simul. Mater. Sci. Eng., **11**, R33 (2003).

[81] S. Izumi, T. Kawakami, S. Sakai. A FEM-MD combination method for silicon. Simulation of Semiconductor Processes and Devices, International Conference on 6-8 Sept., 143, (1999).

[82] S. Izumi, T. Kawakami, S. Sakai. Study of a combined FEM-MD method for silicon. JSME Int. J. Ser. A-Solid Mech. Mat. Eng., **44**, 152 (2001).

[83] W. K. Liu, E. G. Karpov, S. Zhang, H. S. Park. An introduction to computational nanomechanics and materials. Comput. Meth. Appl. Mech. Eng., **193**, 1529 (2004).

[84] S. Ogata, E. Lidorikis, F. Shimojo, A. Nakano, P. Vashishta, R. K. Kalia. Hybrid finite-element/molecular-dynamics/electronic-density-functional approach to materials simulations on parallel computers. Comput. Phys. Commun., **138**, 143 (2001).

[85] H. Morkoc, S. N. Mohammad. High-luminosity blue and blue-green gallium nitride light-emitting-diodes. Science, **267**, 51 (1995).

[86] G. Fasol. Room-temperature blue gallium nitride laser diode. Science, **272**, 1751 (1996).

[87] G. S. Cheng, A. Kolmakov, Y. X. Zhang, M. Moskovits, R. Munden, M. A. Reed, G. M. Wang, D. Moses, J. P. Zhang. Current rectification in a single GaN nanowire with a well-defined p-n junction. Appl. Phys. Lett., **83**, 1578 (2003).

[88] J. E. Bradby, S. O. Kucheyev, J. S. Williams, J. Wong-Leung, M. V. Swain, P. Munroe, G. Li , M. R. Phillips. Indentation-induced damage in GaN epilayers. Appl. Phys. Lett., **80**, 383 (2002).

[89] P. Puech, F. Demangeot, J. Frandon, C. Pinquier, M. Kuball, V. Domnich, Y. Gogotsi. GaN nanoindentation: A micro-Raman spectroscopy study of local strain fields. J. Appl. Phys., **96**, 2853 (2004).

[90] E. Le Bourhis, G. Patriarche. Solid-solution strengthening in ordered InxGa1-xP alloys. Philos. Mag. Lett., **84**, 373 (2004).

[91] J. Li, K. J. Van Vliet, T. Zhu, S. Yip, S. Suresh. Atomistic mechanisms governing elastic limit and incipient plasticity in crystals. Nature, **418**, 307 (2002).

[92] D. E. Kim, S. I. Oh. Atomistic simulation of structural phase transformations in monocrystalline silicon induced by nanoindentation. Nanotechnology, **17**, 2259 (2006).

[93] S. R. Jian, T. H. Fang, D. S. Chuu, L. W. Ji. Atomistic modeling of dislocation activity in nanoindented GaAs. Appl. Surf. Sci., **253**, 833 (2006).

[94] X. D. Li, L. M. Zhang, H. S. Gao. Micro/nanomechanical characterization of a single decagonal AlCoNi quasicrystal. J. Phys. D-Appl. Phys., **37**, 753 (2004).

[95] M. Campo, A. Urena, J. Rams. Effect of silica coatings on interfacial mechanical properties in aluminium - SiC composites characterized by nanoindentation. Scr. Mater., **52**, 977 (2005).

[96] S. R. Jian, T. H. Fang, D. S. Chuu. Nanomechanical characterizations of InGaN thin films. Appl. Surf. Sci., **252**, 3033 (2006).

[97] J. E. Lennard-Jones. The determination of molecular fields. I. from the variation of the viscosity of gas with temperature. Proc. Roy. Soc., **106**, 441 (1924).

[98] F. Cleri, V. Rosato. Tight-binding potentials for transition metals and alloys. Phys. Rev. B, **48**, 22 (1993).

[99] S. Plimpton. Computational limits of classical molecular dynamics simulations. J.

Comput. Phys., **117**, 1 (1995).

[100] B. M. Boghosian. Computational physics on the connection machine. Comp. in Phys., Jan/Feb (1990).

[101] G. C. Fox, M. A. Johnson, G. A. Lyzenga, S. W. Otto, K. J. Salmon, D. W. Walker. Solving Problems on Concurrent Processors: Volume 1, NJ (1988).

[102] G. S. Karypi, K. Schloegel, V. Kumar. University of Minnesota, Department of Computer Science (1998).

[103] G. Sines. Elasticity and Strength. Allyn and Bacon, Boston (1969).

[104] S. Timoshenko, J. N. Goodier. Theory of Elasticity, 2nd (1951).

[105] D. T. Greenwood. Principles of Dynamics, 1st (1965).

[106] C. I. Bajer. Triangular and tetrahedral space-time finite elements in vibration analysis. Int. J. Numer. Methods Eng. **23**, 2031 (1986).

[107] C. I. Bajer. Notes on the stability of non-rectangular space-time finite elements. Int. J. Numer. Methods Eng. **24**, 1721 (1986).

[108] R. W. Clough. Comparison of Three dimensional Finite Elements in Proceedings of the Symposium on Application of Finite Element Methods in Civil Engineering. Vanderbilt University, 1 (1969).

[109] R. W. Hamming. Numerical Methods for Scientists and Engineers. McGraw-Hill Book Co. Inc., 1st (1962).

[110] A. K. Noor. Parallel Processing in Finite Element Structural Analysis. Eng. Comput., **3**, 225 (1988).

[111] C. Farhat, E. Wilson. Concurrent iterative solution of large finite element systems. Commun. Appl. Numer. Meth., **3**, 319 (1987).

[112] S. W. Bostic, R. E. Fulton. Implementation of the lanczos method for structural vibration analysis on a parallel computer. Comput. Struct., **25**, 395 (1987).

[113] L. Adams. Reordering computations for parallel execution. Commun. Appl. Numer. Meth., **2**, 263 (1986).

[114] M. Ortiz, B. Nour-Omid. Unconditionally stable concurrent procedures for transient finite element analysis. Comput. Meth. Appl. Mech. Eng., **58**, 151 (1986).

[115] J. S. Przemieniecki. Matrix structural analysis of substructures. AAIA Journal, **1**, 138 (1963).

[116] C. Farhat, F. X. Roux. A method of finite element tearing and interconnecting and its parallel solution algorithm. Int. J. Numer. Methods Eng., **32**, 1205 (1991).

[117] B. Smith, P. Bjorstad, W. Gropp. Domain Decomposition: Parallel Multilevel Methods for Elliptic Partial Differential Equations. Cambridge University, USA (1996).

[118] H. M. Chen, G. C. Archer. New domain decomposition algorithm for nonlinear substructures. J. Comput. Civil. Eng., **19**, 148 (2005).

[119] P. Geng, J. T. Oden, R. A. ven de Geijn. Parallel multifrontal algorithm and its implementation. Comput. Meth. Appl. Mech. Eng., **149**, 289 (1997).

[120] Y. Saad. Iterative Methods for Sparse Linear Systems. PWS Publishing Company, UWA (1996).

[121] M. Papadrakakis, Y. Tsompanakis. Domain decomposition methods for parallel solution of shape sensitivity analysis problems. Int. J. Numer. Methods Eng., **44**, 281 (1999).

[122] Y. R. Jeng, P. C. Tsai, T. H. Fang. Molecular dynamics studies of atomic-scale friction for roller-on-slab systems with different rolling-sliding conditions. Nanotechnology, **16**, 1941 (2005).

[123] D. Frenkel, B. Smit. Understanding Molecular Simulation. 2nd ed. (2002).

[124] F. Cleri, V. Rosato. Tight-binding potentials for transition metals and alloys. Phys. Rev. B, **48**, 22 (1993).

[125] Y. Lee, J. Y. Park, S. Y. Kim, S. Jun, S. Im. Atomistic simulations of incipient plasticity under Al (111) nanoindentation. Mech. Mater., **37**, 1035 (2005).

[126] C. Zhu, W. Guo, T. X. Yu, C. H. Woo. Radial compression of carbon nanotubes: deformation and damage, super-elasticity and super-hardness. Nanotechnology, **16**, 1035 (2005).

[127] H. Y. Liang, C. H. Woo, H. Huang, A. H. W. Ngan, T. X. Yu. Dislocation nucleation in the initial stage during nanoindentation. Philos. Mag., **83**, 3609 (2003).

[128] V. Yamakov, D. Wolf, S. R. Phillpot, A. K. Mukherjee, H. Gleiter. Dislocation processes in the deformation of nanocrystalline aluminium by molecular-dynamics simulation. Nature, **1**, 1 (2002).

[129] T. H. Fang, S. R. Jian, D. S. Chuu. Molecular dynamics analysis of effects of velocity and loading on the nanoindentation. Jpn. J. Appl. Phys., **41**, L1328 (2002).

[130] J. L. Humar. Dynamics of Structures. 2nd ed. (2002).

[131] W. C. Oliver, G. M. Pharr. Measurement of hardness and elastic modulus by instrumented indentation: Advances in understanding and refinements to methodology. J. Mater. Res., **19**, 3 (2004).

[132] S. R. Jian, T. H. Fang, D. S. Chuu. Analysis of physical properties of III-nitride thin films by nanoindentation. J. Electron. Mater., **32**, 496 (2003).

[133] X. D. Li, B. Bhushan. A review of nanoindentation continuous stiffness measurement technique and its applications. Mater. Charact., **48**, 11 (2002).

[134] W. C. Oliver, G. M. Pharr. An improved technique for determining hardness and elastic-modulus using load and displacement sensing indentation experiments. J. Mater. Res., **7**, 1564 (1992).

[135] M. D. Drory, J. W. Ager, T. Suski, I. Grzegory, S. Porowski. Hardness and fracture toughness of bulk single crystal gallium nitride. Appl. Phys. Lett., **69**, 4044 (1996).

[136] R. Nowak, M. Pessa, M. Suganuma, M. Leszczynski, I. Grzegory, S. Porowski, F. Yoshida. Elastic and plastic properties of GaN determined by nano-indentation of bulk crystal. Appl. Phys. Lett., **75**, 2070 (1999).

[137] S. O. Kucheyev, J. E. Bradby, J. S. Williams, C. Jagadish, M. V. Swain, G. Li. Deformation behavior of ion-beam-modified GaN. Appl. Phys. Lett., **78**, 156 (2001).

[138] P. Kavouras, P. Konminou, T. Karakostas. Effects of ion implantation on the mechanical behavior of GaN films. Thin Solid Films, **515**, 3011 (2007).

[139] D. William, JR Callister. Materials Science and Engineering. 6th ed. (2003).

[140] N. Miyazaki, Y. Shiozaki. Calculation of mechanical properties of solids using molecular dynamics. JSME Int. J. Ser. A-Solid Mech. Mat. Eng., **39**, 606 (1996).

[141] D. Srolovitz, K. Maeda, V. Vitek, T. Egami. Structural Defects in Amorphous Solids: Statistical Analysis of a Computer Model. Philos. Mag., **44**, 847 (1981).

[142] D. Saraev, R. E. Miller. Atomic-scale simulations of nanoindentation-induced plasticity in copper crystals with nanometer-sized nickel coatings. Acta Mater., **54**, 33 (2006).

[143] T. Zhu, J. Li, K. J. Van Vliet, S. Ogata, S. Yip, S. Suresh. Predictive modeling of nanoindentation-induced homogeneous dislocation nucleation in copper. J. Mech. Phys. Solids, **52**, 691 (2004).

[144] K. J. Van Vliet, J. Li, T. Zhu, S. Yip, S. Suresh. Quantifying the early stages of plasticity through nanoscale experiments and simulations. Phys. Rev. B, **67**, 104105 (2003).

[145] C. L. Kelchner, S. J. Plimpton, J. C. Hamilton. Dislocation nucleation and defect structure during surface indentation. Phys. Rev. B, **58**, 11085 (1998).

[146] D. Hull, D. J. Bacon. Introduction to Dislocations. 4th ed. (2001).

[147] W. M. Huang, J. F. Su, M. H. Hong, B. Yang. Pile-up and sink-in in micro-indentation of a NiTi shape-memory alloy. Scr. Mater., **53**, 1055 (2005).

[148] H. C. Barshilia, K. S. Rajam. Characterization of Cu/Ni multilayer coatings by nanoindentation and atomic force microscopy. Surf. Coat. Technol., **155**, 195 (2002).

[149] W. C. Oliver, G. M. Pharr. An improved technique for determining hardness and elastic modulus using load and displacement sensing indentation experiments. J. Mater. Res., **7**, 1564 (1992).

[150] H. Ni, X. Li, H. Gao, T. P. Nguyen. Nanoscale structural and mechanical characterization of bamboo-like polymer/silicon nanocomposite films. Nanotechnology, **16**, 1746 (2005).

[151] R. A. Mirshams, R. M. Pothapragada. Correlation of nanoindentation measurements of nickel made using geometrically different indenter tips. Acta Mater., **54**, 1123 (2006).

[152] L. Riester, P. J. Blau, E. Lara-Curzio, K. Breder. Nanoindentation with a Knoop

indenter. Thin Solid Films, **377,** 635 (2000).

[153] J. L. Bucaille, S. Stauss, P. Schwaller, J. Michler. A new technique to determine the elastoplastic properties of thin metallic films using sharp indenters. Thin Solid Films, **447**, 239 (2004).

[154] R. Schwaiger, B. Moser, M. Dao, N. Chollacoop, S. Suresh. Some critical experiments on the strain-rate sensitivity of nanocrystalline nickel. Acta Mater., **51**, 5159 (2003).

[155] J. A. D. Jensen, P. O. A. Persson, K. Pantleon, M. Oden, L. Hultman. Electrochemically deposited nickel membranes; process—microstructure—property relationships. Surf. Coat. Technol., **172**, 79 (2003).

[156] R. Mitra, R. A. Hoffman, A. Madan, J. R. Weertman. Effect of process variables on the structure, residual stress and hardness of sputtered nanocrystalline nickel films. J. Mater. Res., **16**, 1010 (2001).

[157] R. A. Mirshams, P. Padama. Nanoindentation of nanocrystalline Ni with geometrically different indenters. Mater. Sci. Eng. A-Struct. Mater. Prop. Microstruct. Process., **372**, 252 (2004).

[158] M. Kopycinska-Muller, R. H. Geiss, J. Muller, D. C. Hurley. Elastic-property measurements of ultrathin films using atomic force acoustic microscopy. Nanotechnology, **16**, 703 (2005).

[159] D. Mulliah, S. D. Kenny, E. McGee, R. Smith, A. Richter, B. Wolf. Atomistic modelling of ploughing friction in silver, iron and silicon. Nanotechnology, **17**, 1807 (2006).

[160] R. Smith, D. Christopher, S. D. Kenny. Defect generation and pileup of atoms during nanoindentation of Fe single crystals. Phys. Rev. B, **67**, 245405 (2003).

[161] P. Walsh, A. Omeltchenko, R. K. Kalia, A. Nakano, P. Vashishta. Nanoindentation of silicon nitride: A multimillion-atom molecular dynamics study. Appl. Phys. Lett., **82**, 118 (2003).

[162] R. Astala, M. Kaukonen, R. M. Nieminen. Nanoindentation of silicon surfaces: Molecular-dynamics simulations of atomic force microscopy. Phys. Rev. B, **61**, 2973 (2000).

[163] T. H. Fang, W. J. Chang, C. I. Weng. Nanoindentation and nanomachining characteristics of gold and platinum thin films. Mater. Sci. Eng. A-Struct. Mater. Prop. Microstruct. Process., **430**, 332 (2006).

[164] A. Noreyan, J. G. Amar, I. Marinescu. Molecular dynamics simulations of nanoindentation of beta-SiC with diamond indenter. Mater. Sci. Eng. B-Solid State Mater. Adv. Technol., **117**, 235 (2005).

[165] T. H. Fang, C. I. Weng, J. G. Chang. Mater. Sci. Eng. A-Struct. Mater. Prop. Microstruct. Process., **357**, 7 (2003).

[166] J. Y. Hsieh, S. P. Ju, S. H. Li, C. C. Hwang. Temperature dependence in

nanoindentation of a metal substrate by a diamondlike tip. Phys. Rev. B, **70**, 195424 (2004).

[167] S. R. Jian, T. H. Fang, D. S. Chuu, L. W. Ji. Atomistic modeling of dislocation activity in nanoindented GaAs. Appl. Surf. Sci., **253**, 833 (2006).

[168] A. Richter, R. Ries, R. Smith, M. Henkel, B. Wolf. Nanoindentation of diamond, graphite and fullerene films. Diam. Relat. Mat., **9**, 170 (2000).

[169] S. O. Kucheyev, J. E. Bradby, J. S. Williams, C. Jagadish, M. Toth, M. R. Phillips, M. V. Swain. Nanoindentation of epitaxial GaN films. Appl. Phys. Lett., **77**, 3373 (2000).

[170] L. W. Ma, J. M. Cairney, M. J. Hoffman, P. R. Munroe. Characterization of TiN thin films subjected to nanoindentation using focused ion beam milling. Appl. Surf. Sci., **237**, 631 (2004).

[171] J. E. Bradby, J. S. Williams, M. V. Swain. Pop-in events induced by spherical indentation in compound semiconductors. J. Mater. Res., **19**, 380 (2004).

[172] D. H. Mosca, N. Mattoso, C. M. Lepienski, W. Veiga, I. Mazzaro, V. H. Etgens, M. Eddrief. Mechanical properties of layered InSe and GaSe single crystals. J. Appl. Phys., **91**, 140 (2002).

[173] J. L. Weyher, M. Albrecht, T. Wosinski, G. Nowak, H. P. Strunk, S. Porowski. Study of individual grown-in and indentation-induced dislocations in GaN by defect-selective etching and transmission electron microscopy. Mater. Sci. Eng. B-Solid State Mater. Adv. Technol., **80**, 318 (2001).

[174] J. E. Bradby, J. S. Williams, J. Wong-Leung, M. V. Swain, P. Munroe. Transmission electron microscopy observation of deformation microstructure under spherical indentation in silicon. Appl. Phys. Lett., **77**, 3749 (2000).

[175] S. J. Bull. Nano-indentation of coatings. J. Phys. D-Appl. Phys., **38**, R393 (2005).

[176] Y. Gaillard, C. Tromas, J. Woirgard. Pop-in phenomenon in MgO and LiF: observation of dislocation structures. Philos. Mag. Lett., **83**, 553 (2003).

VITA

王中鼎 (Chung-Ting Wang)

Education and Training:

1986-1990 B.S.
Department of Civil Engineering, Chung Chang Institute Technology, Taiwan.

1994-1996 M.S.
Department of Civil Engineering, Chung Chang Institute Technology, Taiwan.

2001-2007 Ph.D.
Department of Mechanical and Electro-Mechanical Engineering, National Sun Yat-Sen University, Taiwan.

Publication:

A. Journal paper

1. C. H. Chien, Y. D. Wu, Y. T. Chiou, C. C. Hsieh, Y. C. Chen, T. P. Chen, M. L. Tsai, C. T. Wang, "Nanoscale Deformation Measurement using the Gray-level Method by Holographic Interferometry", Optics and Lasers in Engineering, Vol. 44, pp.80, 2006 (**SCI**).

2. C. H. Chien, S. R. Jian, C. T. Wang, J. Y. Juang, J. C. Huang, Y. S. Lai, "Cross-sectional transmission electron microscopy observations on the Berkovich indentation-induced deformation microstructures in GaN thin films", Journal of Physics D: Applied Physics, Vol. 40, pp.3958, 2007 (**SCI**).

3. S. P. Ju, C. T. Wang, C. H. Chien, J. C. Huang, S. R.. Jian, "The material responses of nanoindentation-induced on different nickel orientation surfaces", Molecular Simulation, Vol. 33, pp.905, 2007(**SCI**).

4. S. P. Ju, C. T. Wang, C. H. Chien, "Multiscale simulation of nanoindentation in monocrystal nickel", Nanotechnoloby, 2007 (**SCI**) (Submit).

5. C. H. Chien, C. T. Wang, S. P. Ju, "The influence of indentation rate effect on the material responses of amorphous ZrNi alloy induced by nanoindentation", Applied Physics Letters, 2007 (**SCI**) (Prepare).

B. Conference paper

1. H. Chien, T. P. Chen, C. C. Hsieh, Y. D. Wu, C. T. Wang, 16-19 May 2004, "Hygro-Thermal Buckling Of A Thin PBGA Package",24th International

Conference on Microelectronics, Nis, Serbia and Montenegro, pp. 637-640.

2. C. H. Chien, Y. D. Wu, C. C. Hsieh, Y. C. Chen, T. P. Chen, C. T. Wang, August 2004, "Nanoscale Measurement with Microscale Surface Resolution by Holographic Interferometry", International Conference on Experimental Mechanics, ICEM12, Politecnico di Bari, Italy.

3. 朱訓鵬，廖明亮，王中鼎，"以分子動力學模擬研究甲基丙烯酸甲酯於金基板上在不同溫度下之現象"，第四屆精密機械與製造技術研討會。

C. Patent

錢志回，吳以德，陳太平，陳永昌，謝其昌，邱以泰，王中鼎，蔡明郎，"量測物體位移至次奈米級解析度之方法與設備"，中華民國專利發明第 204822 號，專利權期間 2004.05.21-2023.07.30.

D. Report

朱訓鵬，王中鼎，"鎳薄膜之多尺度奈米壓痕模擬與分析"，國科會 96 年度計劃結案報告書, NSC 95-2221-E-110-070.